Constructing a 3-D radially anisotropic crustal velocity model for Oklahoma using full waveform inversion

Shuo Zhang[1] and Hejun Zhu[1]

[1]University of Texas at Dallas

May 8, 2023

Abstract

Over the past decade, the seismicity rate in the state of Oklahoma has increased significantly, which has been linked to industrial operations, such as saltwater injection. Taking advantage of induced earthquakes and recently deployed seismometers, we construct a 3-D radially anisotropic seismic velocity model for the crust of Oklahoma by using full waveform inversion. To mitigate the well-known cycle-skipping problem, we use misfit functions based on phase and waveform differences in several frequency bands. Relative velocity perturbations in the inverted model allow us to delineate major geological provinces in Oklahoma, such as the Anadarko and Arkoma Basins, as well as the Cherokee Platform and Shelf. In addition, radial anisotropy in the inverted model reflects deformation within the crust of Oklahoma, which might correlate with sedimentary layers, micro-cracks/fractures, as well as the dominant orientation of anisotropic minerals. The crystalline basement beneath Oklahoma can be inferred from the new velocity model, which enables us to classify induced seismicity in current earthquake catalogs better. Furthermore, synthetic experiments suggest that the new velocity model enables us to better constrain earthquake location in Oklahoma,

especially for determining their depths, which are important for investigating induced seismicity.

Constructing a 3-D radially anisotropic crustal velocity model for Oklahoma using full waveform inversion

Shuo Zhang[1] **and Hejun Zhu**[1,2]

[1]Department of Geosciences, The University of Texas at Dallas
[2]Department of Physics, The University of Texas at Dallas

Key Points:

- We use induced earthquakes and full waveform inversion to construct a 3-D radially anisotropic seismic velocity for the crust of Oklahoma.
- Spatial distributions of inverted velocity and radial anisotropy agree with geological provinces and tectonic deformation in Oklahoma.
- Lateral velocity heterogeneities have strong impacts on earthquake location, especially for epicentral depths.

Abstract

Over the past decade, the seismicity rate in the state of Oklahoma has increased significantly, which has been linked to industrial operations, such as saltwater injection. Taking advantage of induced earthquakes and recently deployed seismometers, we construct a 3-D radially anisotropic seismic velocity model for the crust of Oklahoma by using full waveform inversion. To mitigate the well-known cycle-skipping problem, we use misfit functions based on phase and waveform differences in several frequency bands. Relative velocity perturbations in the inverted model allow us to delineate major geological provinces in Oklahoma, such as the Anadarko and Arkoma Basins, as well as the Cherokee Platform and Shelf. In addition, radial anisotropy in the inverted model reflects deformation within the crust of Oklahoma, which might correlate with sedimentary layers, micro-cracks/fractures, as well as the dominant orientation of anisotropic minerals. The crystalline basement beneath Oklahoma can be inferred from the new velocity model, which enables us to better classify induced seismicity in current earthquake catalogs. Furthermore, synthetic experiments suggest that the new velocity model enables us to better constrain earthquake location in Oklahoma, especially for determining their depths, which are important for investigating induced seismicity.

Plain Language Summary

Taking advantage of induced earthquakes and seismometers deployed in Oklahoma in the last decade, we construct a radially anisotropic seismic model for the crust beneath Oklahoma by using full waveform inversion. The data misfit is iteratively reduced by about 40%, and predicted seismograms associated from the new velocity model can fit observations very well. We can identify geological structures from the velocity model, such as low velocity anomalies associated with the Anadarko Basin, and fast anomalies relative to the Cherokee Platform. Positive radial anisotropy in the shallow crust might reflect layered structure of sedimentary, while the negative radial anisotropy with the middle crust may relate to preferred orientation of anisotropic minerals, such as plagioclase, mica and amphibole. Furthermore, synthetic tests are used to illustrate the impact of lateral variations of seismic velocity on earthquake locations, especially for epicentral depths. Therefore, this new 3-D model provides us an opportunity to improve current catalogs of earthquakes in Oklahoma, and improve our understanding about the triggering mechanism of induced earthquakes.

1 Introduction

Located in the middle of the North American Plate, the state of Oklahoma is dominated by east-west oriented tectonic stress for a long time and results in its widespread crustal deformation (Whitaker & Engelder, 2006; Almqvist & Mainprice, 2017; Lund Snee & Zoback, 2020). Due to its comparatively stable tectonic condition, seismicity in this area remains relatively low for decades. However, since 2008, seismologists observed a significant increase in seismicity in the state of Oklahoma, which reached a peak level around 2016 and then gradually decreased to a normal level. To date, many studies have attributed these unexpected earthquakes as induced seismicity related to industry activities, such as saltwater injection (Ellsworth, 2013; Walsh & Zoback, 2015; X. Chen et al., 2018) and hydraulic fracturing (Holland, 2013a; Rubinstein & Mahani, 2015; Skoumal et al., 2018). During this time, the 2011 Mw 5.7 Prague earthquake (Keranen et al., 2013; Sumy et al., 2014) and the 2016 Mw 5.8 Pawnee earthquake (Barbour et al., 2017; Pennington & Chen, 2017) are the two largest earthquakes ever occurred in Oklahoma, resulting in severe damage to the local community and infrastructure. In order to monitor these unusual seismic activities, many seismometers have been deployed in Oklahoma (Walter et al., 2020), giving us an opportunity to use seismic tomography to study the crustal structure of Oklahoma.

An accurate 3-D crustal velocity model is important for earthquake source estimations. With 1-D seismic velocity profiles and dense arrays in Oklahoma, several earthquake catalogs have been developed (Schoenball & Ellsworth, 2017; Cramer et al., 2017; Mueller, 2019), which enable us to delineate some previously unmapped 3-D fault systems in Oklahoma (Holland, 2013b; McNamara et al., 2015; Schoenball & Ellsworth, 2017). However, there are still a lot of randomly distributed earthquakes in these catalogs that cannot be directly linked to any fault systems. A number of studies have illustrated the impacts of lateral crustal velocity heterogeneities on earthquake location (Thurber, 1983; Michelini & Lomax, 2004; Font et al., 2013; Zhu, 2018), as well as moment tensor solutions (Q. Liu et al., 2004; X. Wang & Zhan, 2020; Takemura et al., 2021). Both of them are critical for studying earthquake triggering processes and delineating fault geometry in the subsurface. To date, there are few community-shared 3-D crustal velocity models in Oklahoma that can be used to potentially improve the accuracy of current earthquake catalogs and better delineate fault geometry (Tan et al., 2021).

Seismic tomography is a classical method to construct velocity models from seismic data recorded at the Earth's surface. The idea of iteratively constraining seismic model parameters by minimizing mismatches between observations and predictions has been proposed for a long time (Lailly & Bednar, 1983; Tarantola, 1984). Tromp et al. (2005) recognized the generality of using the adjoint-state method in seismic tomography, which combines high-quality seismic recordings with numerical modeling to map the spatial distribution of seismic parameters. So far, full waveform inversion (FWI) has been widely utilized to constrain crustal and upper mantle structures in California (Tape et al., 2010; K. Wang et al., 2020), Alaska (G. Chen et al., 2023), Austrilia (Fichtner et al., 2009), New Zealand (Chow et al., 2020), Europe (Fichtner et al., 2013; Zhu et al., 2015), Eastern Asia (M. Chen et al., 2017; Tao et al., 2018; Zhang et al., 2018), North America (Zhu et al., 2017), Antarctic (A. Lloyd et al., 2020), North Atlantic (Rickers et al., 2013), and the entire Earth (French & Romanowicz, 2014; Lei et al., 2020), etc.

In order to better investigate induced seismicity in Oklahoma, we construct a 3-D seismic velocity model for the crust of Oklahoma by fully exploiting three-component seismograms collected over the past several years. The lateral variations of seismic velocity and radial anisotropy in the inverted model can be used to investigate geological structures and deformation in Oklahoma (Fouch & Rondenay, 2006; J. Wang & Zhao, 2009; Long, 2013). In this paper, we first briefly review the tectonic evolution of the crust beneath Oklahoma in section 2. The datasets and the initial model used in the inversion are introduced in section 3. Section 4 presents determinations of misfit functions, model parameterizations, and kernel processing. We illustrate the improvements in both data and model domains in section 5. Section 6 discusses the reliability of the inverted model, potential origins of radial anisotropy, depths of the crystalline basement, and impact of velocity heterogeneities on earthquake locations.

2 Brief Introduction of Tectonic Evolution in Oklahoma

Oklahoma has experienced a long tectonic evolution history over the past 1.4 billion years, which forms its present-day crustal and lithospheric structure (Johnson & Luza, 2008). Since the Precambrian period, geological structures beneath Oklahoma experienced numerous cycles of continental collision and rifting (Johnson & Luza, 2008). The oldest rocks found in Oklahoma are Precambrian igneous and metamorphic rocks that formed about 1.4 billion years ago (Sloss, 1988). Before being covered by shallow sea-water in the early Paleozoic, the surface of Oklahoma was exposed and partly eroded (Hamilton, 1956). Due to the circulations of deposition and erosion during Silurian and Devonian (Chenoweth, 1968), multiple thin layers of black shale overlay on limestone and dolomite. Thick sedimentary layers were formed after rapid subsidence in the Carboniferous period (Johnson & Luza, 2008), with most petroleum reservoirs found in Pennsylvanian shale in Oklahoma (Ball et al., 1991). Most of Oklahoma was above sea level by the Triassic and Jurassic periods, which was then overlapped by the Cretaceous Sea. The weathered and loose surface of Oklahoma, which was contributed by shale, sandstone, and limestone, were characterized as the Quaternary sedimentary.

To date, the principal mountain belts, including the Ouachita, the Arbuckle, and the Wichita mountains are located around the Southern Oklahoma Aulacogen, while the Anadarko, the Arkoma, the Ardmore, and the Ouachita basins received sediments with 2 to 12 km thickness (Johnson, 1996) (Figure 1A). The Anadarko basin is one of the major tectonic provinces in Oklahoma (Evans, 1979), with sedimentary rocks ranging from the Cambrian to the Permian periods. The thickest sedimentary column, in excess of 12 km, is detected at the southern edge of the Anadarko basin, with the average thickness of the basin around 4.6 km (Kolawole et al., 2020). In contrast, the sedimentary thickness goes down to 0.6 km on the northern and western flanks of the basin, as well as the Cherokee shelf and platform (Mitchell & Landisman, 1970). To date, the Anadarko Basin is one of the largest oil production zones in America (Higley et al., 2014).

3 Databases and The Initial Model

3.1 Distributions of Earthquakes and Seismometers

We collect centroid moment tensor (CMT) solutions for earthquakes that occurred between 2010 and 2018 (Figure 1D) from the Earthquake Center of St. Louis University (SLU; `https://www.eas.slu.edu/eqc/eqc.html`). These CMT solutions are jointly inverted by using surface-wave spectrum amplitudes, radiation patterns, waveforms, and first motions (Herrmann, 2013). In total, 153 earthquakes from the SLU catalog are used in this study (Figure 1B), most of which are distributed around the Nemaha and Wilzetta strike-slip fault zones with depths around 5 km (Figure 1E). They are small- to moderate-sized earthquakes with magnitudes ranging from 3.4 to 4.8 (Figure 1F).

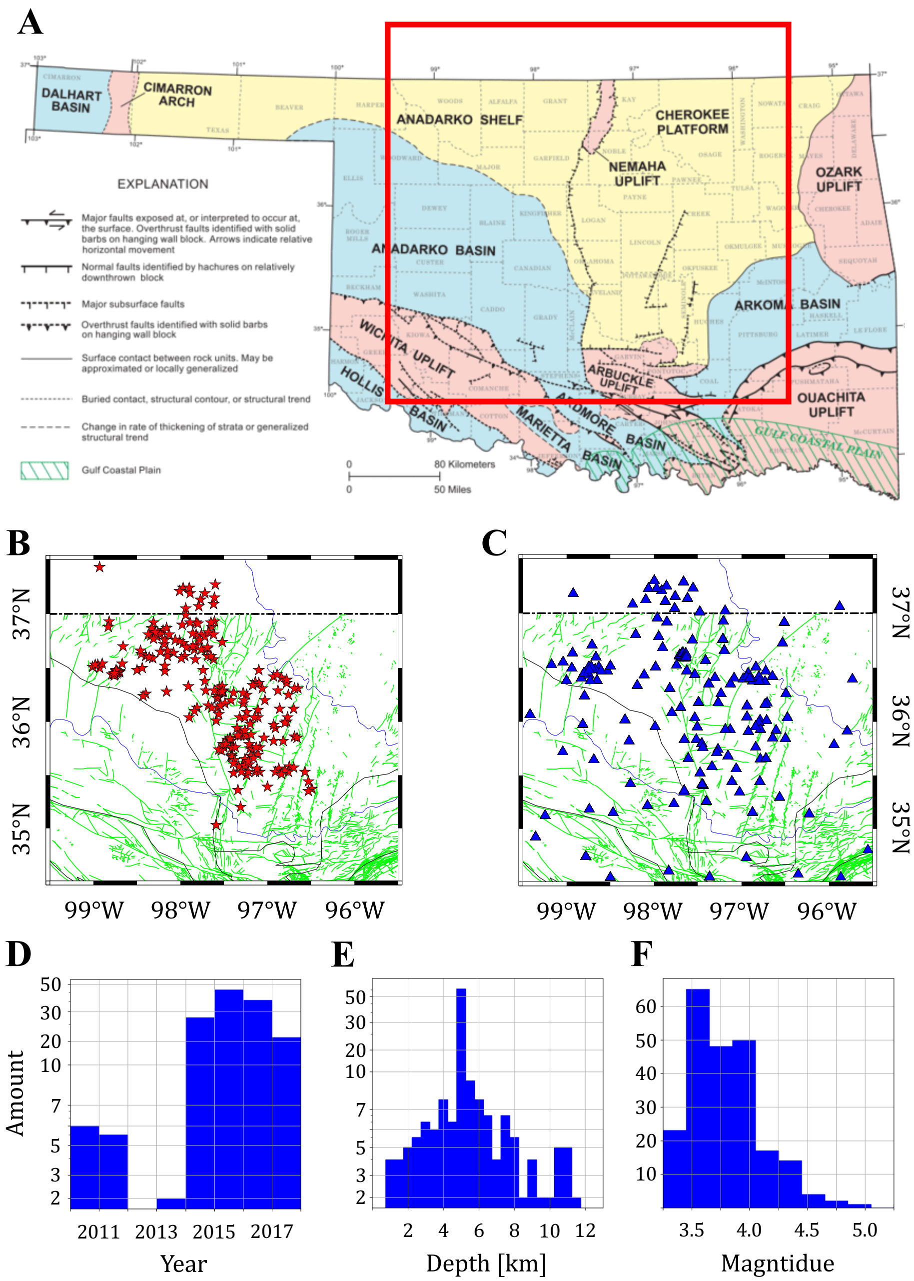

Figure 1. Tectonic map and distributions of earthquakes and stations used in this study. Panel A shows the simplified geological map modified from Northcutt and Campbell (1996). The red box represents the inversion region in this study. Panels B and C demonstrate the locations of 153 earthquakes (red stars) and 176 available stations (blue triangles). Green lines in panels B and C represent fault traces mapped at the Earth's surface (Marsh & Holland, 2016), while thin black lines delineate geological provinces shown in panel A. Panels D to F show the histograms of occurring times, depths and magnitudes of collected earthquakes from the SLU catalog.

Three-component waveform recordings for these events are downloaded from the Data Management Center of the Incorporated Research Institutions of Seismology (IRIS-DMC). The USArray Transportable Array (TA) covered the study region from 2010 to 2012, after which a number of temporary arrays have been deployed to monitor the increasing seismicity in Oklahoma. In total, 176 seismographic stations are used in this study (Figure 1C), allowing us to achieve a dense ray sampling for the state of Oklahoma.

3.2 The Initial Model and Spectral Element Mesh

We use a 3-D isotropic velocity model as the initial model, which was constructed by using adjoint tomography to fit vertical-vertical component ambient noise cross-correlation functions with a 5-40 s frequency band (Zhu, 2018). It gives us good fits for long-period surface waves with relatively low spatial resolutions, but does not include shallow sedimentary layers due to the limited frequency bands. Here, we incorporate a shallow layer (<1.5 km) from Shen and Ritzwoller (2016) into the starting model in order to represent sediments with slow seismic velocities in Oklahoma. The interface of these two models (at 1.5 km depth) is smoothed by a Gaussian filter with standard deviation $\sigma = 200\ m$, in order to avoid any artificial reflections. The simulation domain includes central and northern Oklahoma, as well as southern parts of Kansas, ranging from $34.5°\ N$ to $37.5°\ N$ in latitude and $99.5°\ W$ to $95.5°\ W$ in longitude. The Moho depths of the study region vary from 38 to 44 km (Keller, 2013), thus, our model is truncated at 50 km depth. The Earth's surface is comparatively flat in Oklahoma, ranging from 200 to 600 m (Amante & Eakins, 2009).

SPECFEM3D_Cartesian is used to calculate forward and adjoint wavefields with the spectral element method (Komatitsch & Tromp, 1999; Peter et al., 2011). Topography from ETOPO1 (Amante & Eakins, 2009) is incorporated into the discretized spectral-element mesh. The entire mesh includes 428,544 spectral elements and 28,340,784 Gauss-Lobatto-Legendre grid points. The minimum resolvable period is around 1.61 s and the minimum element size is approximately 1.25 km at the Earth's surface. With 128 cores on the Lonestar 6 cluster at the Texas Advanced Computing Center (TACC), it takes 48 minutes to perform one forward simulation and approximately 2 hours for calculating misfit gradients for each individual event.

4 Method

4.1 Choices of Misfit Functions

The specific misfit function in FWI determines the purposes and eventual performance of the inversion (Tromp et al., 2005). In the last decades, a variety of misfit functions have been designed based on travel-times differences (Luo & Schuster, 1991), surface wave dispersion curves (Beaty et al., 2002; Dal Moro et al., 2007), envelopes differences (Bozdağ et al., 2011; Wu et al., 2014), dynamic wrapping functions (Ma & Hale, 2013), adaptive matching filters (Warner & Guasch, 2016; Zhu & Fomel, 2016), cross-correlation functions (Y. Liu et al., 2017; Tao et al., 2017), Wasserstein distances (Métivier et al., 2016; Yang & Engquist, 2018), etc. Among them, the L2 norm of waveform differences is the classical misfit to constrain seismic velocity models. However, it suffers from nonlinearity and cycle-skipping problems (Virieux & Operto, 2009). In order to mitigate these difficulties, two misfit functions based on phase and waveform differences are used in this study. Here, FLEXWIN is applied to automatically select useful windows, which allows us to compare phase shifts, STA/LTA, as well as envelopes of observed and predicted waveforms (Maggi et al., 2009).

We first update the velocity models by reducing phase differences. Here, frequency-dependent phase differences are measured by using a multi-taper technique (Tape et al., 2010),

$$\chi_1 = \frac{1}{2}\sum_s \sum_r \sum_m N_m \int \left[\frac{\Delta\tau_m(\omega)}{\sigma_m(\omega)}\right]^2 \mathrm{d}\omega \quad , \tag{1}$$

where $\Delta\tau_m$ denotes the phase difference between observations and predictions for m component, and σ_m is the associated uncertainty of the phase measurement. ω is the angular frequency, N_m denotes the weighting factor to balance the contributions of different components. The total misfit (Equation 1) is the summation over all earthquakes s, stations r, and wave components m. To further mitigate the nonlinearity of FWI, a multi-scale strategy (Bunks et al., 1995) is applied via inverting the velocity model using three different frequency bands, 10-30 s, 5-30 s, and 2-30 s, sequentially.

Once the travel-time differences between observed and predicted waveforms are less than half period of the dominate frequency, we switch to the L2 waveform misfit as,

$$\chi_2 = \frac{1}{2}\int \left[\hat{d}(t) - \hat{s}(t)\right]^2 \mathrm{d}t \quad , \tag{2}$$

where $\hat{d}(t)$ and $\hat{s}(t)$ denote the normalized observations and predictions, in order to mitigate potential errors for moment magnitude from CMT solutions. This second waveform-based misfit enables us to further improve the spatial resolution of the inversion.

4.2 Model Parameterization

Radial anisotropy, with five indenpendent elastic constants (C_{11}, C_{13}, C_{33}, C_{44}, C_{66}), is introduced in the model update to solve the Rayleigh-Love discrepancy (Anderson, 1961; Harkrider, 1964; Debayle & Kennett, 2000). Since the phase measurements are more sensitive to wavespeeds, we use the following five model parameters,

$$\begin{aligned}
\alpha_\mathrm{h} &= \sqrt{\frac{C_{11}}{\rho}} \quad , \\
\alpha_\mathrm{v} &= \sqrt{\frac{C_{33}}{\rho}} \quad , \\
\beta_\mathrm{h} &= \sqrt{\frac{C_{66}}{\rho}} \quad , \\
\beta_\mathrm{v} &= \sqrt{\frac{C_{44}}{\rho}} \quad , \\
\eta &= \frac{C_{13}}{C_{11} - 2C_{44}} \quad .
\end{aligned} \tag{3}$$

where ρ stands for the density. α_h and α_v are the velocities of horizontally and vertically polarized P-wave. β_h and β_v are the velocities of horizontally and vertically polarized S-wave. η is the radial anisotropy parameter.

The mass density ρ is approximated by the following empirical relationship,

$$\delta \mathrm{ln}\rho = 0.33 \mathrm{ln}\beta \quad , \tag{4}$$

where the Voigt average of isotropic compressional- and shear-wave velocities, α and β, can be computed as

$$\alpha = \sqrt{\frac{2\alpha_\mathrm{h}^2 + \alpha_\mathrm{v}^2}{3}} \quad ,$$

$$\beta = \sqrt{\frac{2\beta_{\mathrm{h}}^2 + \beta_{\mathrm{v}}^2}{3}} \quad . \tag{5}$$

We define the radial anisotropy (RA) as,

$$RA = \frac{\beta_{\mathrm{h}} - \beta_{\mathrm{v}}}{\beta} \quad , \tag{6}$$

For each iteration, four model parameters, α_{h}, α_{v}, β_{h}, and β_{v}, are updated simultaneously. Thus, the misfit perturbation can be expressed as a volumetric integral over relative perturbations of these four model parameters as

$$\delta\chi = \int_V K_{\alpha_{\mathrm{h}}}\delta\ln\alpha_{\mathrm{h}} + K_{\alpha_{\mathrm{v}}}\delta\ln\alpha_{\mathrm{v}} + K_{\beta_{\mathrm{h}}}\delta\ln\beta_{\mathrm{h}} + K_{\beta_{\mathrm{v}}}\delta\ln\beta_{\mathrm{v}}\mathrm{d}V \quad , \tag{7}$$

where $K_{\alpha_{\mathrm{h}}}$, $K_{\alpha_{\mathrm{v}}}$, $K_{\beta_{\mathrm{h}}}$ and $K_{\beta_{\mathrm{v}}}$ are the misfit gradients with respect to four radially anisotropic elastic model parameters.

We use the approximated inverse of the diagonal Hessian as the pre-conditioner to balance amplitudes at shallow and deeper depths, and mitigate singular values at source and receiver locations (Luo, 2012; Luo et al., 2015),

$$P(\mathbf{x}) = \frac{1}{\int \partial^2\mathbf{s}(\mathbf{x},t) \cdot \partial^2\mathbf{s}^\dagger(\mathbf{x}, T-t)\mathrm{d}t} \quad , \tag{8}$$

where $\mathbf{s}$ and $\mathbf{s}^\dagger$ denote the forward and adjoint displacement wavefields, respectively.

We also employ a 3-D Gaussian function to smooth the preconditioned kernels. Its standard deviation varies with the dominant wavelength of the inversion. A conjugate-gradient method is utilized to update the model parameters (Fletcher & Reeves, 1964; Matthies & Strang, 1979), with the step length determined by a quadratic interpolation (Tape et al., 2007).

5 Results

5.1 Waveform Fitting

Taking one earthquake occurred in November 8th 2015 as an example (Figure 2A), we compare observed and predicted seismograms to demonstrate the performance of the inversion. The locations and azimuthal distributions of recorded seismometers are shown in Figures 2A and C. Compared with results from the initial model (Figures 3A and S1 in Supporting Information), simulations from the new model fit observed waveforms much better. For instance, for short epicentral distances, predictions can perfectly match observations, while there are still some residuals for longer epicentral distances. Other than fundamental mode surface waves, the inverted model can also reproduce higher-mode oscillations, which can be clearly observed in 5-30 s and 2-30 s frequency bands (Figures 2B and S2 in Supporting Information). For further comparisons, we also simulate wave propagation with the same earthquake and corresponding stations by using a 1-D velocity profile (OGS-1D) provided by the Oklahoma Geological Survey (Darold et al., 2015). For short epicentral distances, the OGS-1D model provides comparably good fittings with observed data, however, it fails to fit observations with long epicentral distances (Figures 3C and S3 in Supporting Information). More details on waveform comparisons with different velocity models can be found in Section S1 of Supporting Information.

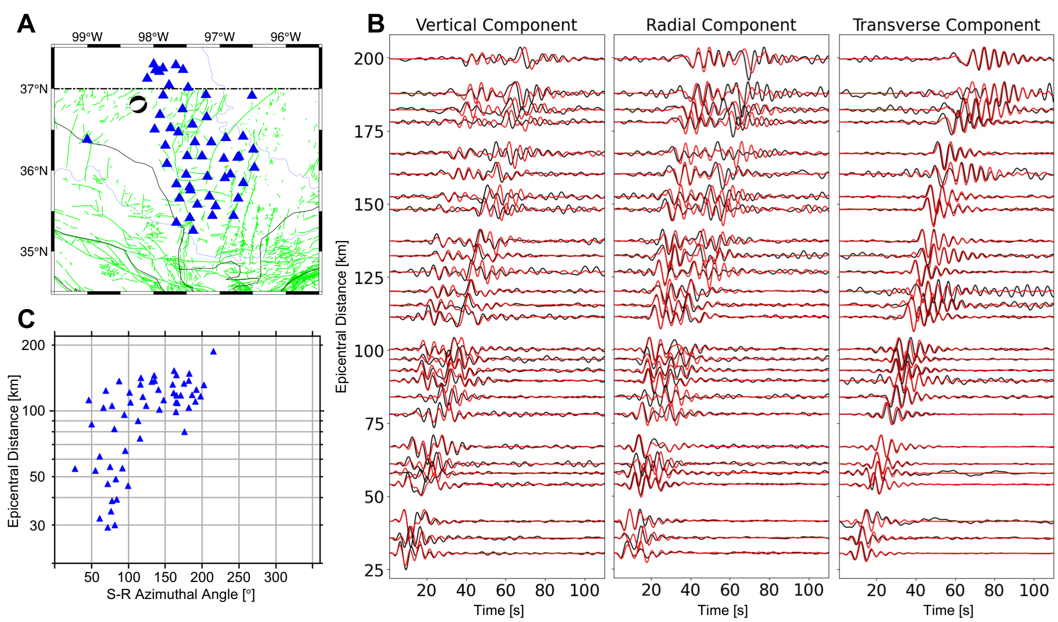

Figure 2. Comparison between observed (black) and predicted (red) waveforms based on the inverted model. The particular earthquake (beachball) and corresponding seismometers (triangle) are shown in panel A. Comparisons of vertical, radial, and transverse component seismograms (with 5-30 s passband) are shown from left to right in panel B. Panel C illustrates the distributions of azimuthal angles and epicentral distances for selected seismograms.

Beyond this particular event, we also present the evolution of data residuals in Figure 4A. In order to mitigate the cycling-skipping problem, three frequency bands, 10-30 s, 5-30 s, 2-30 s, are applied sequentially, with the same phase-based misfit (Equation 1). It is then followed by another five iterations with the L2 norm waveform-based misfit (Equation 2) in 5-30 s frequency band. Because of different frequency bands and misfits, these four stages are not directly comparable. Therefore, we normalize the data misfit within each individual stage for a better comparison. When using the phase-based misfit in 10-30 s (Figure 4A), the data misfit is reduced by about 30% for each individual component. While for higher frequency bands (5-30 s and 2-30 s), the phase difference of the transverse component decreases much faster than the other two components. The data misfit is reduced by around 25% after using the phase-based misfit. In contrast, after switching to the L2 norm waveform misfit in the last five iterations, we observe a larger misfit reduction for vertical and radial components (22%) than the transverse component (13%).

The robustness of the inversion in the data domain can be further illustrated by comparing the histograms of time shifts between the initial and inverted models (Figures 4B-D). The isotropic initial velocity model (Zhu, 2018) still produces 0.5-1.0 s mean travel time errors for three components in the frequency band of 2-30 s. The inverted model enables us to reduce the averaged travel-time error to less than 0.2 s. For instance, the mean traveltime error for the vertical component is reduced from 1.09 s to 0.19 s. In addition, FLEXWIN can detect more windows for the inverted model than the initial model, because of the improvement of overall waveform match. For instance, the total number of detected time windows for the radial component is increased from 1,140 to 2,099 after the inversion.

5.2 3-D Isotropic Shear Wave Velocity Model

We first compute the 1-D velocity profile (FWI-1D) by averaging lateral heterogeneities of the inverted 3-D model, and compare it with OGS-1D in Figure 5A. Starting from slow sedimentary layers with $V_p = 3.0\ km/s$ and $V_s = 1.7\ km/s$, both FWI-1D and OGS-1D consistently increase with depths. Large discrepancies exist between 2 to 7 km, with FWI-1D being slower than OGS-1D by about 9% in P-wave velocity and 3% in S-wave velocity. Considering better waveform comparisons as shown in Figures 3B and C, this comparatively slow velocity at depths of 4-7 km in FWI-1D (Figure 5A) is

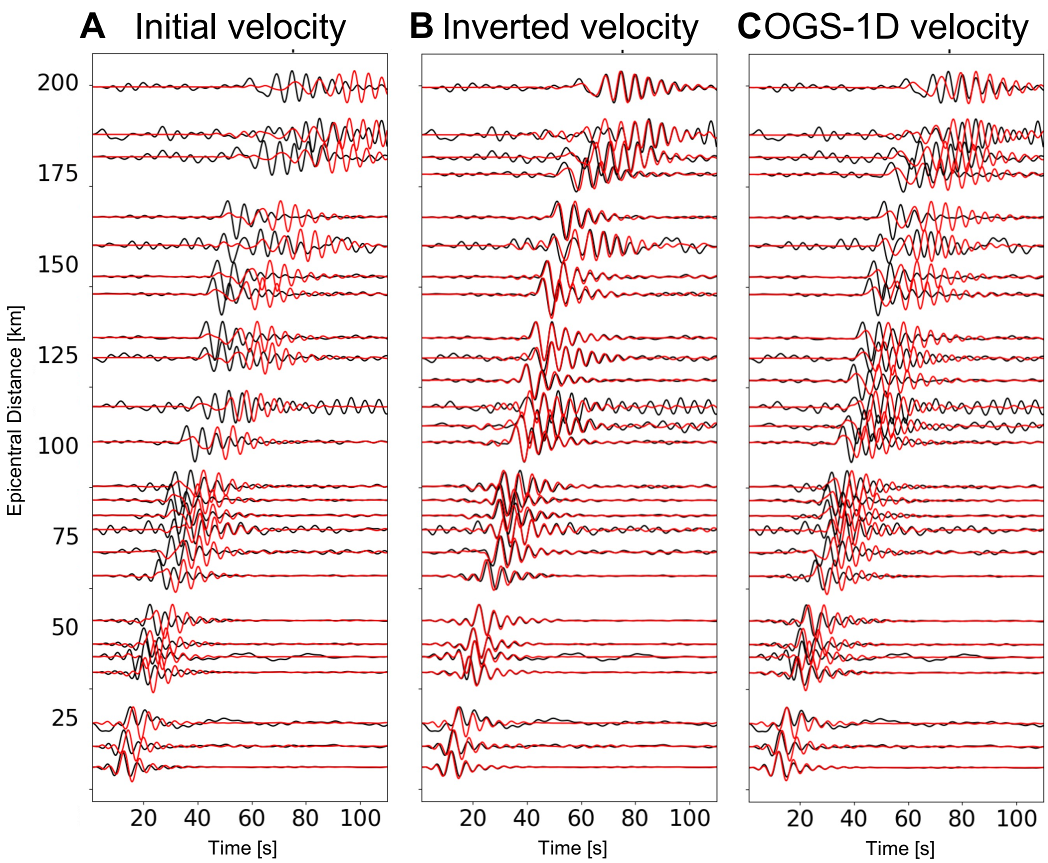

Figure 3. Comparison between transverse component observed (black) and predicted (red) seismograms from different velocity models. Locations of the earthquake and corresponding seismometers are shown in Figure 2A. Panels A to C are resulted from the initial model, inverted model, and OGS-1D profile (Darold et al., 2015), respectively. All seismograms are filtered with 5-30 s passband.

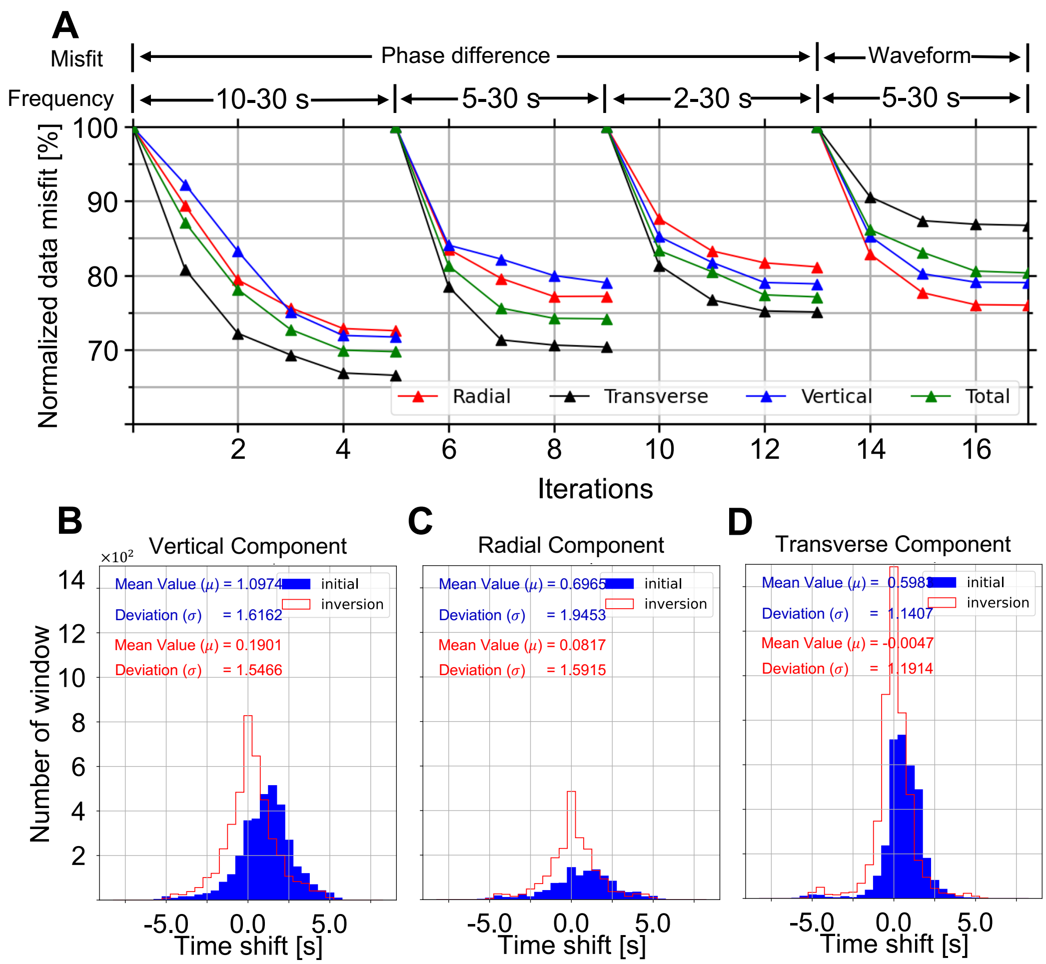

Figure 4. Comparisons of data residuals and travel time histograms. Panel A shows the evolution of data residuals with four stages of total 17 iterations, with different frequency bands and misfit functions. The data misfits are normalized within each individual stage for better comparison. Panels B-D compare the histograms of travel-time differences between three components, observed and predicted seismograms from the initial (blue) and inverted (red) velocity models.

required for waveform fitting. These two 1D velocity profiles are basically consistent with each other in the middle crust. Because of limited frequencies and ray-path coverage, our inversion is not sensitive to velocity perturbations at depths greater than 30 km.

We also compute relative velocity perturbations (Figures 5B-E), with respect to FWI-1D by using $V_{rel} = \ln\frac{V_{3D}}{V_{1D}}$. Two major features can be observed within the uppermost crust (Figure 5B), with slow anomalies for basin areas and fast anomalies for the Cherokee Shelf and Platform. In vertical profiles, the depths of the fast anomaly change from 10 km in the Cherokee Shelf (Figures 6G and I) to less than 5 km in the Cherokee Platform (Figure 6G), which basically agree with geological survey results (Northcutt & Campbell, 1996; Johnson & Luza, 2008; Xu et al., 2009).

In contrast to the fast Cherokee Shelf and Platform, the Anadarko and Arkoma Basins are fulfilled with sandstone and shale after frequent erosion and deposit (Johnson & Luza, 2008), where seismic velocity perturbations are imaged as slow as -10%. In addition, porous and layered structures in these sedimentary basins might further slow down the apparent velocity due to attenuation and scattering effects (Houtz & Ludwig, 1979; Sams et al., 1997; Yu et al., 2015). The NE-SW distribution of the slow velocity anomaly is consistent with the geological boundaries of the Anadarko Basin (Perry, 1989). Similar observations can also be obtained for the Arkoma Basin. The wedge shape of the slow velocity anomaly in the Anadarko Basin, with the lower bound at about 15 km (Figure 6H and I), is consistent with geological investigations (Perry, 1989; Ball et al., 1991; Northcutt & Campbell, 1996). Another fast velocity anomaly can be observed in the middle crust beneath slow basins in Figure 6H, which might be related to the Arbuckle Uplift (Johnson & Luza, 2008) in south Oklahoma.

5.3 Radial Anisotropy

The magnitude of RA, defined by Equation 6, ranges from -5% to +5% in our inverted model. Two large RA anomalies are imaged, a large negative anomaly within the middle crust is overlain by a positive anomaly in the uppermost crust (Figures 5J-L). The positive perturbation is located around the Nemaha-Wilzetta Fault System, which connects the Cherokee Shelf in the west and the Cherokee Platform in the east (Figure 5F). In spite of its large amplitude (+5%), this positive RA is comparatively thin. Underneath

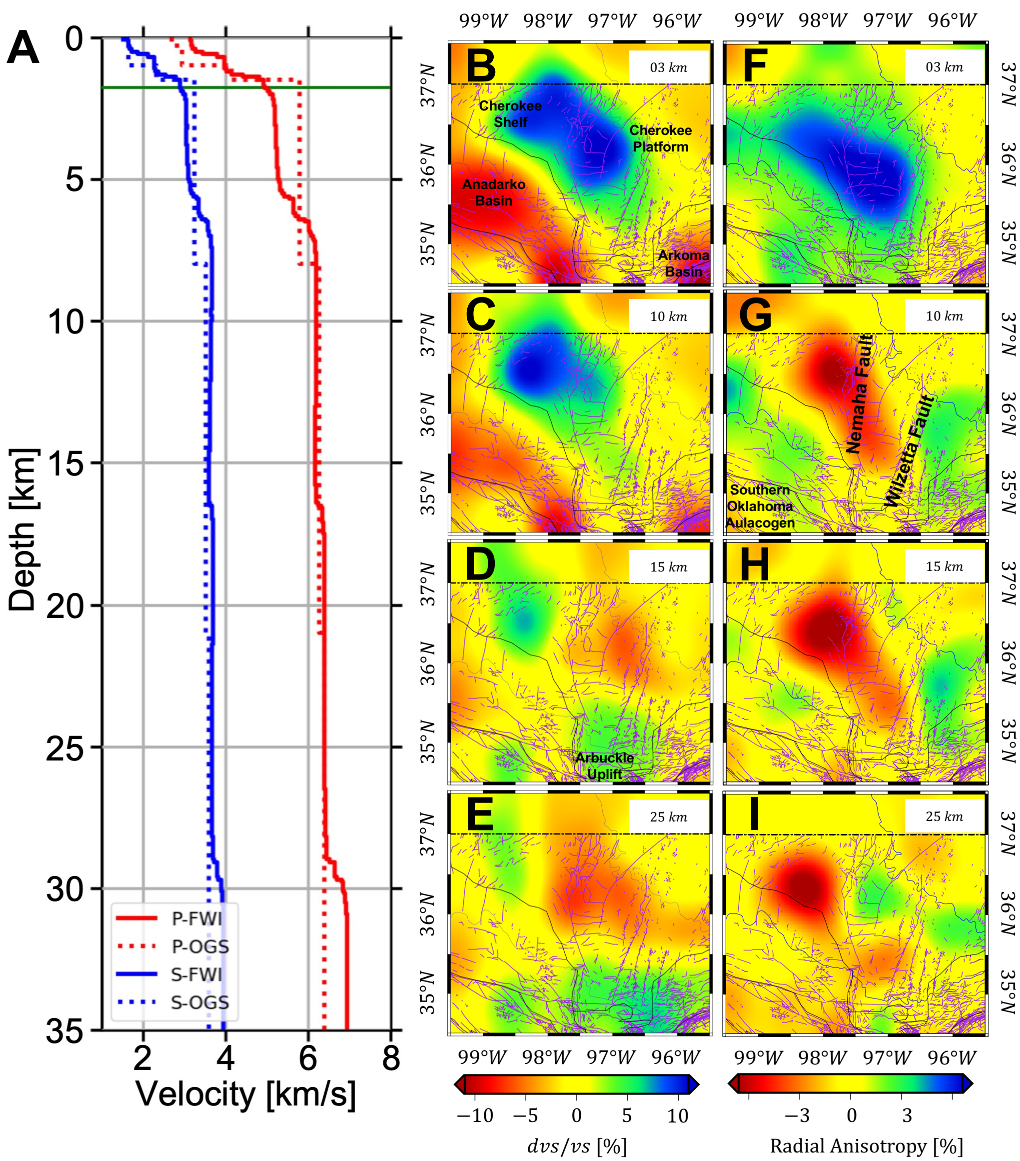

Figure 5. Vertical and horizontal variations of seismic velocities within the inverted model. Panel A compares absolute P (red) and S (blue) wave velocities from OGS-1D (dashed) and FWI-1D (solid) profiles. Panels B to E show relative S velocity variations at depths of 3, 10, 15 and 25 km. Corresponding radial anisotropy at these depths are shown in panels F to I.

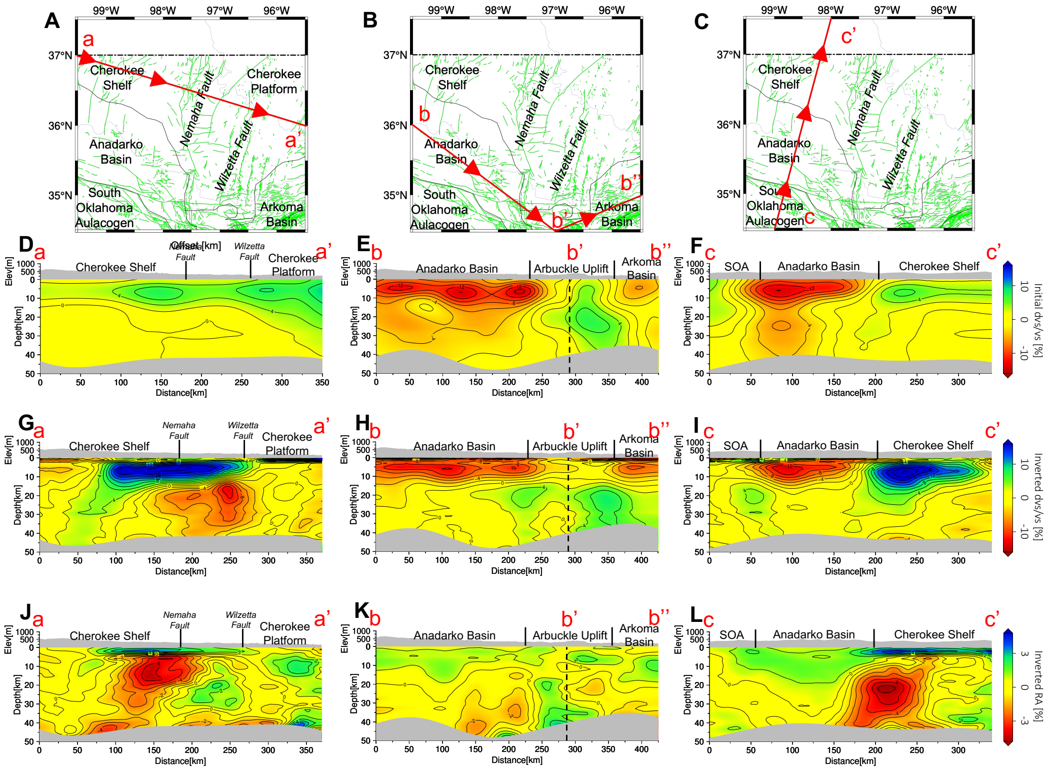

Figure 6. Vertical cross sections of the initial and inverted models and their radial anisotropy. Panels D, G and J are extracted from line a-a' in panel A. Panels E, H and K are extracted from line b-b'-b" in panel B, where the dashed lines indicate the turning point b'. Panels F, I and L are extracted from line c-c' in panel C. Panels D, E and F illustrate shear wave velocity perturbations from the initial velocity model. Panels G, H and I show relative shear wave velocity perturbations from the inverted velocity model. Panels J, K and L are radial anisotropy in the inverted model.

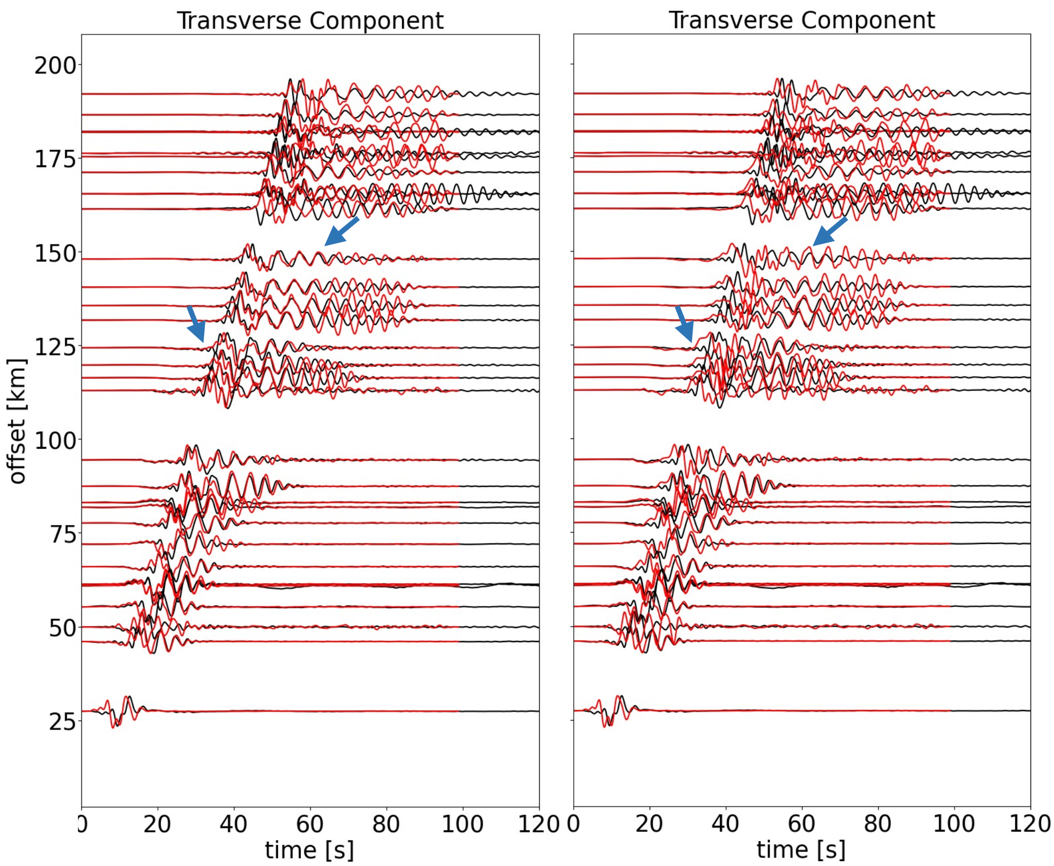

Figure 7. Necessity of incorporating radial anisotropy in the inverted model. Red traces are predicted seismograms based on the inverted model (left) and the modified velocity model after removing positive RA in the uppermost crust (right), while black traces are observations. Only transverse component seismograms are shown here. The locations of earthquake and corresponding stations are the same as Figure 2A. All seismograms are filtered with a 2-30 s passband.

the Anadarko Basin, the weak positive RA (less than +3%) goes down to depths around 20 km (Figures 6K and L).

In contrast to the uppermost crust, a negative RA perturbation (-5%) is imaged within the middle/lower crust beneath the Nemaha-Wilzetta Fault Zone, which is surrounded by relatively weak positive anomalies (+3%) beneath the Anadarko Basin and Cherokee Platform (Figures 5G and H). As the depth increases, the center of this negative anomaly moves northward to the Cherokee Shelf (Figure 5I). The origin of these RA anomalies will be discussed in section 6.2.

To further evaluate the necessity of including radial anisotropy in our inversion, we build another 3-D velocity model by removing the positive RA within the uppermost crust. A Gaussian filter with $\sigma = 0.2\ km$ is applied to remove artificial contrasts due to this modification. All waveforms are filtered with a 2-30 s passband. Compared with the original inverted model (Figure 7A), seismograms from the modified velocity model (Figure 7B) produce much larger mismatches in both travel-times and amplitudes. This comparison demonstrates the necessity of incorporating radial anisotropy in the inversion.

6 Discussion

6.1 Assessments of the Inverted Model

A checkerboard model with a standard deviation $\sigma_{\mathrm{h}} = 30\ km$ in the horizontal direction and $\sigma_{\mathrm{v}} = 10\ km$ in the vertical direction is used to analyze the resolution of our inversion. The amplitude of this checkerboard model is limited within $\pm 15\%$ with respect to the maximum of the inverted model. The action of the Hessian on each model parameter can be approximated by the subtraction of gradients based on perturbed and original 3-D velocity models. In order to evaluate cross-talks among four model parameters, we perturb one model parameter at each time and leave the other three model parameters unchanged.

For instance, Figure 8 illustrates the approximated Hessian action when perturbing β_{v} alone. Regardless of the imperfect shapes resulting from the uneven distribution of seismometers and earthquakes, we are able to successfully recover the positive and negative Gaussian anomalies in the checkerboard model (Figures 8E and e). In addition, the amplitude of the recovered perturbations in β_{v} is ten times larger than the other three model parameters. These results suggest that the inversion is less contaminated by the tradeoff among different model parameters. The other three experiments by perturbing α_{h}, α_{v}, and β_{h} are shown in Section S2 of Supporting Information, which basically give us similar conclusions.

6.2 Origin of Radial Anisotropy

Radial anisotropy can be used as an indicator for investigating tectonic deformation and dynamic processes of the crust (Fouch & Rondenay, 2006; J. Wang & Zhao, 2009; Long, 2013). Major origins of seismic anisotropy include lattice-preferred orientation (LPO)

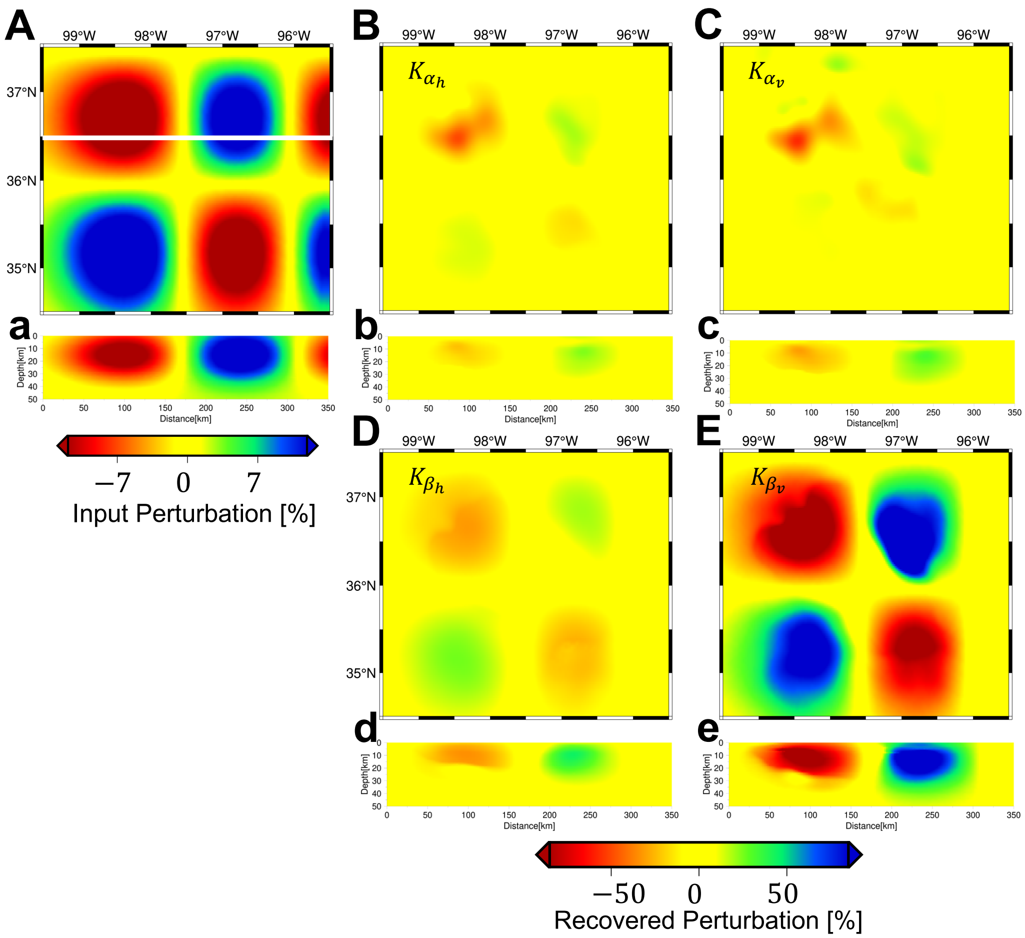

Figure 8. A checkerboard model and corresponding action of the Hessian on velocity perturbation. Panel A shows the distribution of Gaussian anomalies in the checkerboard model. Panels B, C, D and E are the action of the Hessian on 15% perturbations in α_h, α_v, β_h and β_v, respectively. Panels a, b, c, d and e are corresponding vertical sections of Panels A, B, C, D and E along latitude=36.5° N (white line in Panel A).

and shape-preferred orientation (SPO). When discussing the uppermost crust, the alignment of layered structures, pores and cracks could be alternative contributors of radial anisotropy (Babuska & Cara, 1991; Shapiro et al., 2004; Lin et al., 2011).

In our inverted model, we observe positive radial anisotropy near the Earth's surface (Figures 5, and 6), which means that horizontally polarized shear waves V_{sh} are faster than the vertically polarized components V_{sv} (Equation 3). The layered strata of sedimentary deposits might be the major cause of such positive radial anisotropy within the uppermost crust (Crampin, 1989; Johnston & Christensen, 1995; Jiang & Denolle, 2022). The comparatively deep positive anomalies around the Anadarko and Arkoma basins (Figure 6L) might correspond to their thick sedimentary strata, whereas the thin sedimentary deposit in the Cherokee Shelf and Platform can be used to explain their shallow positive anomalies (Figures 6J and L) . In addition, measured by laboratory experiments (Yan et al., 2016), porosity and saturation of sandstone and shale might result in contrastive radial anisotropy in basin and shelf areas as well.

In most cases, radial anisotropy within the middle crust is positive, due to the subhorizontal foliation plane of minerals in response to widespread horizontal-orientated tectonic stress (Shapiro et al., 2004; Guo et al., 2012). However, a large negative volume is observed in the middle crust of the inverted model (Figure 5 and 6). The negative radial anisotropy is often attributed to the injection of magma which forms vertical structures, like dikes (Mordret et al., 2015; Lynner et al., 2018). Nonetheless, few volcanic activities are recorded in the geological history of Oklahoma. In the last decade, negative radial anisotropy has also been reported in Tohoku and Kyushu (J. Wang & Zhao, 2013), the Tehran basin (Shirzad & Shomali, 2014), the eastern Tibet (Huang et al., 2010), and the Los Angeles basin (K. Wang et al., 2020), which potentially result from the preferred orientation of mineral within the middle crust. Therefore, we also interpret the negative volume in the inverted model as the response of anisotropic minerals. With respect to the hexagonal symmetry of mica (Rey, 1993; Shapiro et al., 2004; G. E. Lloyd et al., 2009), or orthorhombic symmetry of amphibole (Brownlee et al., 2017), negative radial anisotropy can be caused by the sub-vertical foliation plane in minerals, which may suggest a potentially vertical tectonic orientation at a local scale. Other than the fast axes in mica/amphibole that are parallel to the direction of deformation, another possible candidate is plagioclase (Christensen, 1996; Almqvist & Mainprice, 2017; Bernard & Behr, 2017), which, in laboratory measurements, exhibits strong anisotropy with fast axes aligning perpendicular to the orientation of shear stresses (Shaocheng & David, 1988; Ji & Salisbury, 1993; Satsukawa et al., 2013). Based on the tectonic history in Oklahoma, the preferred orientation of mica or plagioclase, representing different crystal structures, could be the origin of negative radial anisotropy in the middle crust, but more investigations are needed to distinguish detailed mechanisms.

6.3 Depths of the Crystalline Basement

Figure 9B shows the basement depth in Oklahoma obtained from borehole measurements in the OGS database (`https://www.ou.edu/ogs`). A linear interpolation is applied to smooth these point sampled results. The basement is shallow in the Cherokee Platform and the Southern Oklahoma Aulacogen (less than 0.5 km), and increases in basin areas, such as around 5.0 km in the Arkoma Basin. These borehole measurements are point samples and unevenly distributed, for instance, there are few measurements in the Anadarko and Arkoma Basins, leading to poor constraints on the basement depths in these areas.

Alternatively, we choose the V_s=3.0 km/s contour as a proxy to delineate the lateral variations of the crystalline basement in Oklahoma (Durrheim & Mooney, 1991; Porritt et al., 2020). The resulting map from our inverted 3-D velocity model has similar spatial distribution as well-log measurements, for instance, shallow basement in the Cherokee Platform, the Cherokee Shelf, and the Southern Oklahoma Aulacogen, reflecting thin unconsolidated sedimentary layers. Furthermore, in Figures 9C and D, we show crystalline basement maps extracted from other two 3-D velocity models: US2015 (Schmandt et al., 2015) and US2016 (Shen & Ritzwoller, 2016). Model US2015 is estimated based on multi-mode receiver functions and Rayleigh wave phase velocities (Schmandt et al., 2015), while model US2016 is constrained by the joint inversion of ambient noise Rayleigh wave dispersion curves and P-wave receiver functions (Shen & Ritzwoller, 2016). Their spatial resolution is relatively low when focusing on Oklahoma, since both of them are models for the entire United States. Similar to Figures 9A and B, we can find shallow basements in the Cherokee Platform and the Southern Oklahoma Aulacogen in Figures 9C and D. However, the Anadarko and the Arkoma Basins are not clear in Figures 9C and D, and their depths are overall underestimated, such as around 3 to 4 km in contrast to 12 km from geological surveys and our new model.

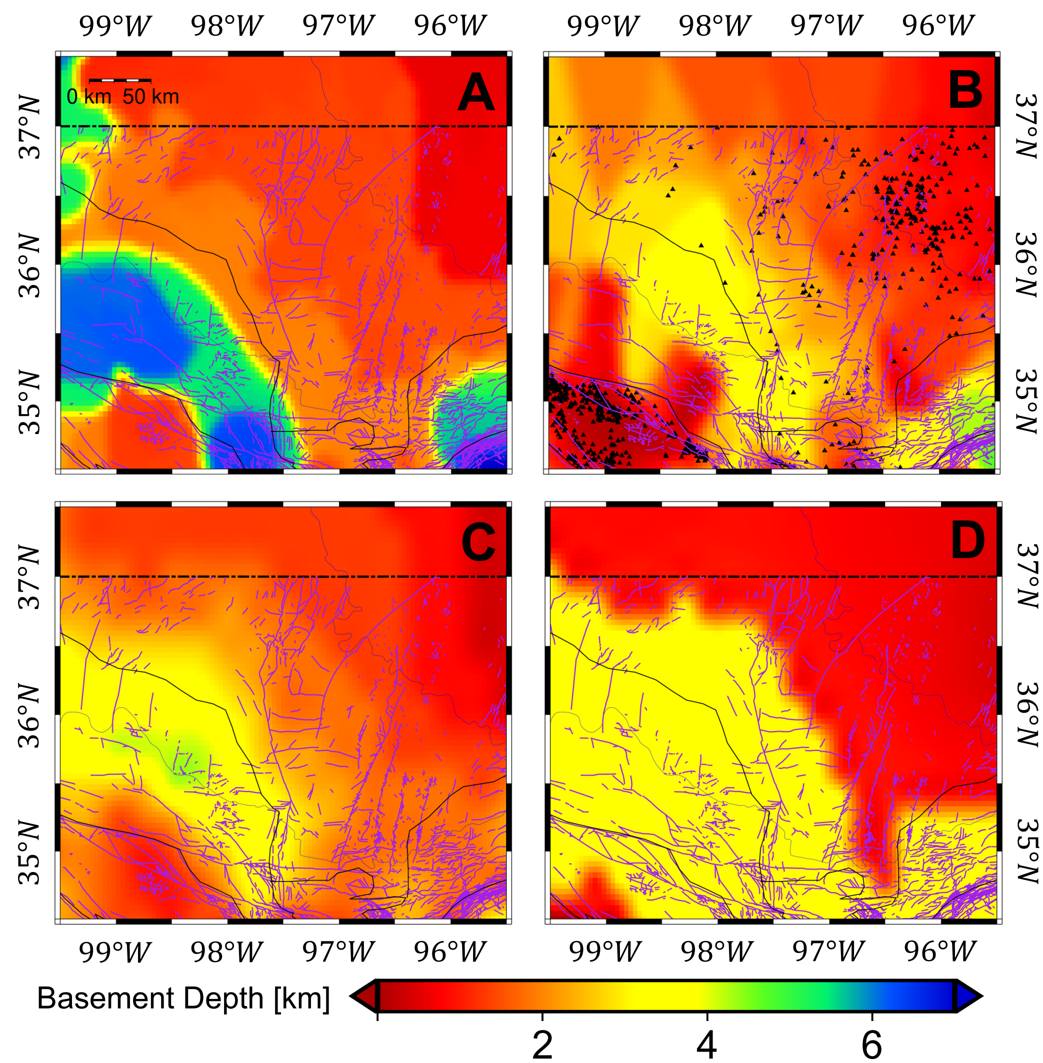

Figure 9. Comparison of crystalline basement depths extracted from our inverted 3D model (Panel A), well log measurements (Panel B), model US2016 from Shen and Ritzwoller (2016) (Panel C) and model US2015 from Schmandt et al. (2015) (Panel D). Black triangles in Panel B represent the locations of well logs (`https://www.ou.edu/ogs`).

6.4 Impact of 3-D velocity models on earthquake locations

To date, many studies have linked the increasing seismicity rate in Oklahoma to industry activities, such as saltwater injection (Keranen et al., 2013, 2014; Langenbruch & Zoback, 2016; X. Chen et al., 2018). Most existing earthquake catalogs are based on 1-D velocity profiles. They have played important roles to study the relation between industry activities and induced seismicity. Previous studies have demonstrated that lateral seismic velocity variations could bias the determination of centroid moment tensor solutions, as well as source locations (Q. Liu et al., 2004; X. Wang & Zhan, 2020). In this section, we illustrate the influence of lateral crustal velocity heterogeneities on earthquake locations in Oklahoma.

In Figure 10, 140 "synthetic earthquakes" are created and they are evenly distributed in the study region, with depths at 5, 10, 15 and 20 km. These "synthetic earthquakes" are relocated by using 58 stations in Oklahoma. Based on the inverted 3-D velocity model, the "observed travel-times" are calculated by using a fast marching method (Sethian, 1996; Sethian & Popovici, 1999), which are then inverted by using NonLinLoc (Lomax et al., 2000) to determine their locations. In the relocation, we use both inverted 3-D velocity model and the associated FWI-1D profile. As shown in Figures 10A and 11B, horizontal biases are overall negligible (less than 2 km) by taking lateral velocity variations or not. Whereas the depth errors are significant (Figures 10B, 10C and 11A). For instance, when using the 1-D velocity profile for earthquake relocation, the vertical errors can go as high as 10 km, which are reduced to around 2.5 km when we use the correct 3-D velocity model. Considering large uncertainties on the depths of relocated earthquakes, it is important to re-investigate the current catalogs by using the inverted 3-D velocity model, which allows us to better determine their depths and further investigate the triggering mechanisms of induced seismicity in Oklahoma.

7 Conclusion

With induced earthquakes and dense seismic stations deployed in Oklahoma, we construct a 3-D radially anisotropic crustal velocity model by using full waveform inversion. Our model can reduce the data misfit by around 40% for all three-component records. This 3-D model enables us to better delineate geological provinces in Oklahoma, such as the Anadarko Basin, the Cherokee Platform, and the Southern Oklahoma Aulacogen.

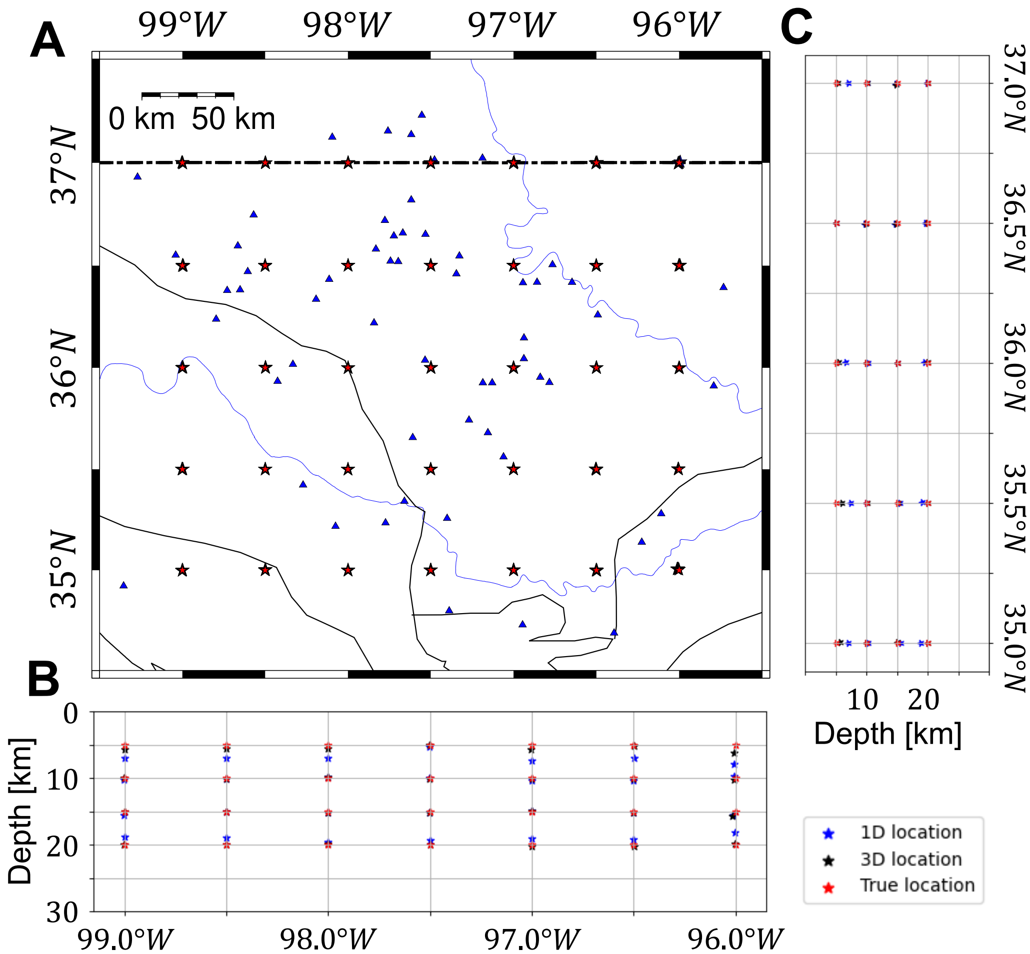

Figure 10. Comparison between earthquake locations based on 1-D (blue stars) and 3-D (black stars) velocity models by using synthetic earthquakes shown as red stars. Blue triangles in panel A denote 58 stations for the relocations. Panels B and C compare results along the vertical sections with latitude=$35.5^{\circ}N$ and longitude=$-98.5^{\circ}N$, respectively.

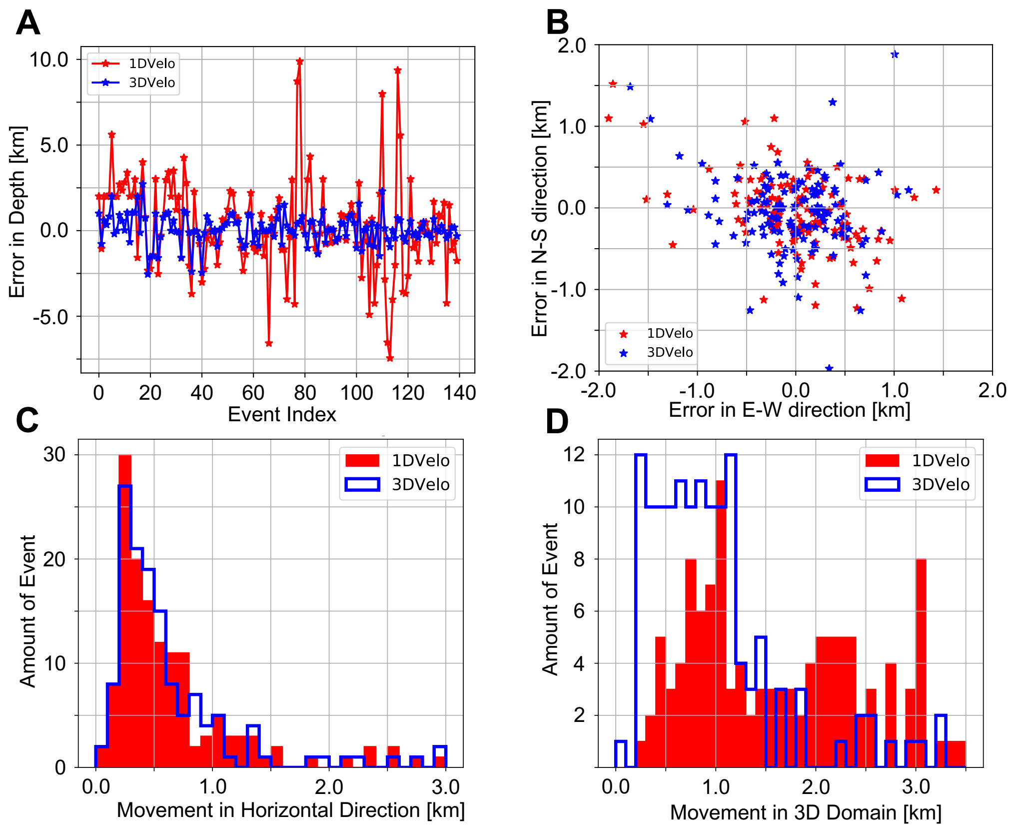

Figure 11. Impact of lateral seismic velocity variations on earthquake locations. Panels A and B illustrate vertical and horizontal errors from relocation based on 1-D (red) and 3-D (blue) velocity models. Panels C and D show the distribution of distances from the true location in the horizontal plane and 3-D volume.

Furthermore, we observe the upper crust is dominated by a thin layer with positive radial anisotropy (+6%), while the middle to lower crust is characterized as relatively large negative radial anisotropy (-6%). These features might be related to deformation from background tectonic stress and preferential alignment of anisotropic minerals. We also extract the depths of the crystalline basement based on the inverted 3-D velocity model, which is overall consistent with borehole measurements. We further demonstrate that the 3-D velocity model allows us to improve the accuracy of earthquake locations, especially for determining their depths. Therefore, the inverted 3-D velocity model provides us an opportunity to better investigate induced earthquakes in Oklahoma.

Acknowledgments

This study is supported by NSF Grant EAR-*** and 3D+4D seismic inversion consortium at the University of Texas at Dallas. We thank the Texas Advanced Computing Center for providing computational facilities for this study. Earthquake source parameters, including time, location, and CMT solutions, are collected from the Earthquake Center of St. Louis University (`https://www.eas.slu.edu/eqc/eqc.html`). Raw seismic waveform records are downloaded from the Data Management Center of Incorporated Research Institutions for Seismology (`https://ds.iris.edu/ds/nodes/dmc/`). Forward and adjoint wavefields are solved by using SPECFEM3D from Computational Infrastructure for Geodynamics (`https://github.com/SPECFEM/specfem3d`). Time window selection is performed by using FLEXWIN (`https://github.com/geodynamics/flexwin`). Well-log information are collected from the Open Data Oklahoma Corporation Commission (`https://www.ou.edu/ogs`). All figures are plotted by Generic Mapping Tools (`https://www.generic-mapping-tools.org/`) and Obspy (`https://docs.obspy.org/`). This is UTD Geoscience contribution number ***.

References

Almqvist, B. S., & Mainprice, D. (2017). Seismic properties and anisotropy of the continental crust: Predictions based on mineral texture and rock microstructure. *Reviews of Geophysics*, *55*(2), 367–433. doi: doi.org/10.1002/2016RG000552

Amante, C., & Eakins, B. W. (2009). *ETOPO1 arc-minute global relief model: procedures, data sources and analysis* (Tech. Rep.). NOAA National Geophysical Data Cente. Retrieved from https://www.ngdc.noaa.gov/mgg/global/relief/ETOPO1/docs/ETOPO1.pdf

Anderson, D. L. (1961). Elastic wave propagation in layered anisotropic media. *Journal of Geophysical Research*, *66*(9), 2953–2963. doi: doi.org/10.1029/JZ066i009p02953

Babuska, V., & Cara, M. (1991). *Seismic anisotropy in the Earth* (Vol. 10). Springer Science & Business Media.

Ball, M. M., Henry, M. E., & Frezon, S. E. (1991). *Petroleum geology of the Anadarko Basin region, province (115), Kansas, Oklahoma, and Texas* (Tech. Rep.). doi: doi.org/10.3133/ofr88450W

Barbour, A. J., Norbeck, J. H., & Rubinstein, J. L. (2017). The effects of varying injection rates in Osage County, Oklahoma, on the 2016 m w 5.8 Pawnee earthquake. *Seismological Research Letters*, *88*(4), 1040–1053. doi: doi.org/10.1785/0220170003

Beaty, K. S., Schmitt, D. R., & Sacchi, M. (2002). Simulated annealing inversion of multimode Rayleigh wave dispersion curves for geological structure. *Geophysical Journal International*, *151*(2), 622–631. doi: doi.org/10.1046/j.1365-246X.2002.01809.x

Bernard, R. E., & Behr, W. M. (2017). Fabric heterogeneity in the Mojave lower crust and lithospheric mantle in Southern California. *Journal of Geophysical Research: Solid Earth*, *122*(7), 5000–5025. doi: doi.org/10.1002/2017JB014280

Bozdağ, E., Trampert, J., & Tromp, J. (2011). Misfit functions for full waveform inversion based on instantaneous phase and envelope measurements. *Geophysical Journal International*, *185*(2), 845–870. doi: doi.org/10.1111/j.1365-246X.2011.04970.x

Brownlee, S. J., Schulte-Pelkum, V., Raju, A., Mahan, K., Condit, C., & Orlandini, O. F. (2017). Characteristics of deep crustal seismic anisotropy from a compilation of rock elasticity tensors and their expression in receiver functions. *Tectonics*, *36*(9), 1835–1857. doi: doi.org/10.1002/2017TC004625

Bunks, C., Saleck, F. M., Zaleski, S., & Chavent, G. (1995). Multiscale seismic waveform inversion. *Geophysics*, *60*(5), 1457–1473. doi: https://doi.org/10.1190/1.1443880

Chen, G., Chen, J., Tape, C., Wu, H., & Tong, P. (2023). Double-difference adjoint tomography of the crust and uppermost mantle beneath Alaska. *Journal of Geophysical Research: Solid Earth*, *128*, e2022JB025168. doi: doi.org/10.1029/2022JB025168

Chen, M., Niu, F., Tromp, J., Lenardic, A., Lee, C.-T. A., Cao, W., & Ribeiro, J. (2017). Lithospheric foundering and underthrusting imaged beneath Tibet. *Nature communications*, *8*(1), 1–10. doi: doi.org/10.1038/ncomms15659

Chen, X., Haffener, J., Goebel, T. H., Meng, X., Peng, Z., & Chang, J. C. (2018). Temporal correlation between seismic moment and injection volume for an induced earthquake sequence in central Oklahoma. *Journal of Geophysical Research: Solid Earth*, *123*(4), 3047–3064. doi: doi.org/10.1002/2017JB014694

Chenoweth, P. A. (1968). Early Paleozoic (Arbuckle) overlap, southern mid-continent, United States. *AAPG Bulletin*, *52*(9), 1670–1688. doi: https://doi.org/10.1306/5D25C4C7-16C1-11D7-8645000102C1865D

Chow, B., Kaneko, Y., Tape, C., Modrak, R., & Townend, J. (2020). An automated workflow for adjoint tomography—waveform misfits and synthetic inversions for the North Island, New Zealand. *Geophysical Journal International*, *223*(3), 1461–1480. doi: doi.org/10.1093/gji/ggaa381

Christensen, N. I. (1996). Poisson's ratio and crustal seismology. *Journal of Geophysical Research: Solid Earth*, *101*(B2), 3139–3156. doi: doi.org/10.1029/95JB03446

Cramer, C. H., Bauer, R. A., Chung, J.-w., Rogers, J. D., Pierce, L., Voigt, V., … others (2017). St. louis area earthquake hazards mapping project: Seismic and liquefaction hazard maps. *Seismological Research Letters*, *88*(1), 206–223.

Crampin, S. (1989). Suggestions for a consistent terminology for seismic anisotropy 1. *Geophysical prospecting*, *37*(7), 753–770. doi: doi.org/10.1111/j.1365-2478.1989.tb02232.x

Dal Moro, G., Pipan, M., & Gabrielli, P. (2007). Rayleigh wave dispersion curve inversion via genetic algorithms and marginal posterior probability density estimation. *Journal of Applied Geophysics*, *61*(1), 39–55. doi: doi.org/10.1016/j.jappgeo.2006.04.002

Darold, A. P., Holland, A. A., Morris, J. K., & Gibson, A. R. (2015). *Oklahoma earthquake summary report 2014* (Tech. Rep.). Okla. Geol. Surv. Open-

File Rept. OF1-2015. Retrieved from `http://ogs.ou.edu/docs/openfile/OF1-2015.pdf`

Debayle, E., & Kennett, B. (2000). Anisotropy in the Australasian upper mantle from Love and Rayleigh waveform inversion. *Earth and Planetary Science Letters*, *184*(1), 339–351. doi: doi.org/10.1016/S0012-821X(00)00314-9

Durrheim, R. J., & Mooney, W. D. (1991). Archean and Proterozoic crustal evolution: Evidence from crustal seismology. *Geology*, *19*(6), 606–609. doi: doi.org/10.1130/0091-7613(1991)019⟨0606:AAPCEE⟩2.3.CO;2

Ellsworth, W. L. (2013). Injection-induced earthquakes. *Science*, *341*(6142). doi: doi.org/10.1126/science.1225942

Evans, J. L. (1979). Major structural and stratigraphic features of the Anadarko basin. , *61*, 2116. doi: doi.org/10.1306/2F9188A1-16CE-11D7-8645000102C1865D

Fichtner, A., Kennett, B. L., Igel, H., & Bunge, H.-P. (2009). Full seismic waveform tomography for upper-mantle structure in the Australasian region using adjoint methods. *Geophysical Journal International*, *179*(3), 1703–1725. doi: doi.org/10.1111/j.1365-246X.2009.04368.x

Fichtner, A., Trampert, J., Cupillard, P., Saygin, E., Taymaz, T., Capdeville, Y., & Villasenor, A. (2013). Multiscale full waveform inversion. *Geophysical Journal International*, *194*(1), 534–556. doi: doi.org/10.1093/gji/ggt118

Fletcher, R., & Reeves, C. M. (1964). Function minimization by conjugate gradients. *The computer journal*, *7*(2), 149–154. doi: doi.org/10.1093/comjnl/7.2.149

Font, Y., Segovia, M., Vaca, S., & Theunissen, T. (2013). Seismicity patterns along the Ecuadorian subduction zone: new constraints from earthquake location in a 3-D a priori velocity model. *Geophysical Journal International*, *193*(1), 263–286. doi: doi.org/10.1093/gji/ggs083

Fouch, M. J., & Rondenay, S. (2006). Seismic anisotropy beneath stable continental interiors. *Physics of the Earth and Planetary Interiors*, *158*(2-4), 292–320. doi: doi.org/10.1016/j.pepi.2006.03.024

French, S., & Romanowicz, B. A. (2014). Whole-mantle radially anisotropic shear velocity structure from spectral-element waveform tomography. *Geophysical Journal International*, *199*(3), 1303–1327. doi: doi.org/10.1093/gji/ggu334

Guo, Z., Gao, X., Wang, W., & Yao, Z. (2012). Upper-and mid-crustal radial anisotropy beneath the central Himalaya and southern Tibet from seismic ambient noise tomography. *Geophysical Journal International*, *189*(2), 1169–1182. doi: doi.org/10.1111/j.1365-246X.2012.05425.x

Hamilton, W. B. (1956). Precambrian rocks of Wichita and Arbuckle mountains, Oklahoma. *Geological Society of America Bulletin*, *67*(10), 1319–1330. doi: doi.org/10.1130/0016-7606(1956)67[1319:PROWAA]2.0.CO;2

Harkrider, D. G. (1964). Surface waves in multilayered elastic media i. Rayleigh and Love waves from buried sources in a multilayered elastic half-space. *Bulletin of the Seismological Society of America*, *54*(2), 627–679. doi: doi.org/10.1785/BSSA0540020627

Herrmann, R. B. (2013). Computer programs in seismology: An evolving tool for instruction and research. *Seismological Research Letters*, *84*(6), 1081–1088. doi: doi.org/10.1785/0220110096

Higley, D. K., Cook, T. A., & Pawlewicz, M. J. (2014). Petroleum systems and assessment of undiscovered oil and gas in the Anadarko Basin Province, Colorado, Kansas, Oklahoma, and Texas—Woodford Shale assessment units. , *58*. doi: doi.org/10.3133/ds69EE

Holland, A. A. (2013a). Earthquakes triggered by hydraulic fracturing in south-central Oklahoma. *Bulletin of the Seismological Society of America*, *103*(3), 1784–1792. doi: doi.org/10.1785/0120120109

Holland, A. A. (2013b). Optimal fault orientations within oklahoma. *Seismological Research Letters*, *84*(5), 876–890. doi: doi.org/10.1785/0220120153

Houtz, R. E., & Ludwig, W. J. (1979). Distribution of reverberant subbottom layers in the southwest Pacific basin. *Journal of Geophysical Research: Solid Earth*, *84*(B7), 3497–3504. doi: doi.org/10.1029/JB084iB07p03497

Huang, H., Yao, H., & van der Hilst, R. D. (2010). Radial anisotropy in the crust of SE Tibet and SW China from ambient noise interferometry. *Geophysical Research Letters*, *37*(21). doi: doi.org/10.1029/2010GL044981

Ji, S., & Salisbury, M. H. (1993). Shear-wave velocities, anisotropy and splitting in high-grade mylonites. *Tectonophysics*, *221*(3-4), 453–473. doi: doi.org/10.1016/0040-1951(93)90173-H

Jiang, C., & Denolle, M. A. (2022). Pronounced Seismic Anisotropy in Kanto Sedimentary Basin: A Case Study of Using Dense Arrays, Ambient Noise Seismology, and Multi-Modal Surface-Wave Imaging. *Journal of Geophysical Research: Solid Earth*, *127*(8), e2022JB024613. doi: doi.org/10.1029/2022JB024613

Johnson, K. S. (1996). *Geology of Oklahoma* (Tech. Rep.). Oklahoma Geological Survey. Retrieved from `http://ogs.ou.edu/docs/specialpublications/SP96-5.pdf`

Johnson, K. S., & Luza, K. V. (2008). *Earth sciences and mineral resources of Oklahoma* (Tech. Rep.). Oklahoma Geological Survey. Retrieved from `http://www.ogs.ou.edu/pubsscanned/EP9_All.pdf`

Johnston, J. E., & Christensen, N. I. (1995). Seismic anisotropy of shales. *Journal of Geophysical Research: Solid Earth*, *100*(B4), 5991–6003. doi: doi.org/10.1029/95JB00031

Keller, G. R. (2013). The Moho of North America: A brief review focused on recent studies. *Tectonophysics*, *609*, 45–55. doi: doi.org/10.1016/j.tecto.2013.07.031

Keranen, K. M., Savage, H. M., Abers, G. A., & Cochran, E. S. (2013). Potentially induced earthquakes in Oklahoma, USA: Links between wastewater injection and the 2011 Mw 5.7 earthquake sequence. *Geology*, *41*(6), 699–702. doi: doi.org/10.1130/G34045.1

Keranen, K. M., Weingarten, M., Abers, G. A., Bekins, B. A., & Ge, S. (2014). Sharp increase in central Oklahoma seismicity since 2008 induced by massive wastewater injection. *Science*, *345*(6195), 448–451. doi: doi.org/10.1126/science.1255802

Kolawole, F., Turko, M. S., & Carpenter, B. M. (2020). Basement-controlled deformation of sedimentary sequences, Anadarko Shelf, Oklahoma. *Basin Research*, *32*(6), 1365–1387. doi: https://doi.org/10.1111/bre.12433

Komatitsch, D., & Tromp, J. (1999). Introduction to the spectral element method for three-dimensional seismic wave propagation. *Geophysical journal international*, *139*(3), 806–822. doi: doi.org/10.1046/j.1365-246x.1999.00967.x

Lailly, P., & Bednar, J. (1983). The seismic inverse problem as a sequence of before stack migrations. In *Conference on inverse scattering: theory and application* (pp. 206–220).

Langenbruch, C., & Zoback, M. D. (2016). How will induced seismicity in Oklahoma respond to decreased saltwater injection rates? *Science advances*, *2*(11), e1601542. doi: https://doi.org/10.1126/sciadv.1601542

Lei, W., Ruan, Y., Bozdağ, E., Peter, D., Lefebvre, M., Komatitsch, D., ... Pugmire, D. (2020). Global adjoint tomography—model GLAD-M25. *Geophysical Journal International*, *223*(1), 1–21. doi: https://doi.org/10.1093/gji/ggaa253

Lin, F.-C., Ritzwoller, M. H., Yang, Y., Moschetti, M. P., & Fouch, M. J. (2011). Complex and variable crustal and uppermost mantle seismic anisotropy in the western United States. *Nature Geoscience*, *4*(1), 55–61. doi: https://doi.org/10.1038/ngeo1036

Liu, Q., Polet, J., Komatitsch, D., & Tromp, J. (2004). Spectral-element moment tensor inversions for earthquakes in southern California. *Bulletin of the Seismological Society of America*, *94*(5), 1748–1761. doi: https://doi.org/10.1785/012004038

Liu, Y., Teng, J., Xu, T., Wang, Y., Liu, Q., & Badal, J. (2017). Robust time-domain full waveform inversion with normalized zero-lag cross-correlation objective function. *Geophysical Journal International*, *209*(1), 106–122. doi: https://doi.org/10.1093/gji/ggw485

Lloyd, A., Wiens, D., Zhu, H., Tromp, J., Nyblade, A., Aster, R., ... others (2020). Seismic structure of the Antarctic upper mantle imaged with adjoint tomography. *Journal of Geophysical Research: Solid Earth*, *125*(3). doi: https://doi.org/10.1029/2019JB017823

Lloyd, G. E., Butler, R. W., Casey, M., & Mainprice, D. (2009). Mica, deformation fabrics and the seismic properties of the continental crust. *Earth and Planetary Science Letters*, *288*(1-2), 320–328. doi: https://doi.org/10.1016/j.epsl.2009.09.035

Lomax, A., Virieux, J., Volant, P., & Berge-Thierry, C. (2000). Probabilistic earthquake location in 3D and layered models. In *Advances in seismic event location* (pp. 101–134). Springer. doi: 10.1007/978-94-015-9536-0_5

Long, M. D. (2013). Constraints on subduction geodynamics from seismic anisotropy. *Reviews of Geophysics*, *51*(1), 76–112. doi: https://doi.org/10.1002/rog.20008

Lund Snee, J.-E., & Zoback, M. D. (2020). Multiscale variations of the crustal stress field throughout North America. *Nature Communications*, *11*(1), 1951. doi: https://doi.org/10.1038/s41467-020-15841-5

Luo, Y. (2012). *Seismic imaging and inversion based on spectral-element and adjoint methods* (Doctoral dissertation, Princeton University). Retrieved from `https://dataspace.princeton.edu/handle/88435/dsp018623hx78j`

Luo, Y., Modrak, R., & Tromp, J. (2015). Strategies in adjoint tomography. In *Handbook of Geomathematics: Second Edition* (pp. 1943–2001). Springer Berlin Heidelberg. doi: 10.1007/978-3-642-54551-1_96

Luo, Y., & Schuster, G. T. (1991). Wave-equation traveltime inversion. *Geophysics*, *56*(5), 645–653. doi: https://doi.org/10.1190/1.1443081

Lynner, C., Beck, S. L., Zandt, G., Porritt, R. W., Lin, F.-C., & Eilon, Z. C. (2018). Midcrustal deformation in the Central Andes constrained by radial anisotropy. *Journal of Geophysical Research: Solid Earth*, *123*(6), 4798–4813. doi: https://doi.org/10.1029/2017JB014936

Ma, Y., & Hale, D. (2013). Wave-equation reflection traveltime inversion with dynamic warping and full-waveform inversion. *Geophysics*, *78*(6), R223–R233. doi: https://doi.org/10.1190/geo2013-0004.1

Maggi, A., Tape, C., Chen, M., Chao, D., & Tromp, J. (2009). An automated time-window selection algorithm for seismic tomography. *Geophysical Journal International*, *178*(1), 257–281. doi: https://doi.org/10.1111/j.1365-246X.2009.04099.x

Marsh, S., & Holland, A. (2016). *Comprehensive fault database and interpretive fault map of Oklahoma* (Tech. Rep.). Oklahoma Geological Survey. Retrieved from `http://ogs.ou.edu/docs/openfile/OF2-2016.pdf`

Matthies, H., & Strang, G. (1979). The solution of nonlinear finite element equations. *International journal for numerical methods in engineering*, *14*(11), 1613–1626. doi: https://doi.org/10.1002/nme.1620141104

McNamara, D. E., Benz, H. M., Herrmann, R. B., Bergman, E. A., Earle, P., Holland, A., . . . Gassner, A. (2015). Earthquake hypocenters and focal mechanisms in central Oklahoma reveal a complex system of reactivated subsurface strike-slip faulting. *Geophysical Research Letters*, *42*(8), 2742–2749. doi: https://doi.org/10.1002/2014GL062730

Métivier, L., Brossier, R., Mérigot, Q., Oudet, E., & Virieux, J. (2016). Measuring the misfit between seismograms using an optimal transport distance: Application to full waveform inversion. *Geophysical Supplements to the*

Monthly Notices of the Royal Astronomical Society, *205*(1), 345–377. doi: doi.org/10.1093/gji/ggw014

Michelini, A., & Lomax, A. (2004). The effect of velocity structure errors on double-difference earthquake location. *Geophysical Research Letters*, *31*(9). doi: https://doi.org/10.1093/gji/ggw014

Mitchell, B., & Landisman, M. (1970). Interpretation of a crustal section across Oklahoma. *Geological Society of America Bulletin*, *81*(9), 2647–2656. doi: https://doi.org/10.1130/0016-7606(1970)81[2647:IOACSA]2.0.CO;2

Mordret, A., Rivet, D., Landès, M., & Shapiro, N. M. (2015). Three-dimensional shear velocity anisotropic model of Piton de la Fournaise Volcano (La Réunion Island) from ambient seismic noise. *Journal of Geophysical Research: Solid Earth*, *120*(1), 406–427. doi: https://doi.org/10.1002/2014JB011654

Mueller, C. S. (2019). Earthquake catalogs for the USGS national seismic hazard maps. *Seismological Research Letters*, *90*(1), 251–261. doi: https://doi.org/10.1785/0220170108

Northcutt, R. A., & Campbell, J. A. (1996). Geologic provinces of Oklahoma. *The Shale Shaker*, *46*(5), 99–103. doi: 10.1007/978-94-011-5098-9_2

Pennington, C., & Chen, X. (2017). Coulomb stress interactions during the M w 5.8 Pawnee sequence. *Seismological Research Letters*, *88*(4), 1024–1031. doi: https://doi.org/10.1785/0220170011

Perry, W. J. (1989). *Tectonic evolution of the Anadarko Basin region, Oklahoma* (No. 1866). Department of the Interior, US Geological Survey. doi: https://doi.org/10.3133/b1866A

Peter, D., Komatitsch, D., Luo, Y., Martin, R., Le Goff, N., Casarotti, E., … others (2011). Forward and adjoint simulations of seismic wave propagation on fully unstructured hexahedral meshes. *Geophysical Journal International*, *186*(2), 721–739. doi: doi.org/10.1111/j.1365-246X.2011.05044.x

Porritt, R., Savvaidis, A., Young, B., Shirley, M., & Li, P. (2020). Crustal Structure in Southeastern Texas From Joint Inversion of Ambient Seismic Noise and P to S Receiver Functions. *Geochemistry, Geophysics, Geosystems*, *21*(7), e2019GC008866. doi: https://doi.org/10.1029/2019GC008866

Rey, P. (1993). Seismic and tectono-metamorphic characters of the lower continental crust in Phanerozoic areas: A consequence of post-thickening extension. *Tec-*

tonics, *12*(2), 580–590. doi: https://doi.org/10.1029/92TC01568

Rickers, F., Fichtner, A., & Trampert, J. (2013). The Iceland–Jan Mayen plume system and its impact on mantle dynamics in the North Atlantic region: evidence from full-waveform inversion. *Earth and Planetary Science Letters*, *367*, 39–51. doi: https://doi.org/10.1016/j.epsl.2013.02.022

Rubinstein, J. L., & Mahani, A. B. (2015). Myths and facts on wastewater injection, hydraulic fracturing, enhanced oil recovery, and induced seismicity. *Seismological Research Letters*, *86*(4), 1060–1067. doi: https://doi.org/10.1785/0220150067

Sams, M., Neep, J., Worthington, M., & King, M. (1997). The measurement of velocity dispersion and frequency-dependent intrinsic attenuation in sedimentary rocks. *Geophysics*, *62*(5), 1456–1464. doi: https://doi.org/10.1190/1.1444249

Satsukawa, T., Ildefonse, B., Mainprice, D., Morales, L., Michibayashi, K., & Barou, F. (2013). A database of plagioclase crystal preferred orientations (CPO) and microstructures–implications for CPO origin, strength, symmetry and seismic anisotropy in gabbroic rocks. *Solid Earth*, *4*(2), 511–542. doi: https://doi.org/10.5194/se-4-511-2013

Schmandt, B., Lin, F.-C., & Karlstrom, K. E. (2015). Distinct crustal isostasy trends east and west of the Rocky Mountain Front. *Geophysical Research Letters*, *42*(23), 10–290. doi: https://doi.org/10.1002/2015GL066593

Schoenball, M., & Ellsworth, W. L. (2017). Waveform-relocated earthquake catalog for Oklahoma and southern Kansas illuminates the regional fault network. *Seismological Research Letters*, *88*(5), 1252–1258. doi: https://doi.org/10.1785/0220170083

Sethian, J. A. (1996). A fast marching level set method for monotonically advancing fronts. *Proceedings of the National Academy of Sciences*, *93*(4), 1591–1595. doi: https://doi.org/10.1073/pnas.93.4.1591

Sethian, J. A., & Popovici, A. M. (1999). 3-D traveltime computation using the fast marching method. *Geophysics*, *64*(2), 516–523. doi: https://doi.org/10.1190/1.1444558

Shaocheng, J., & David, M. (1988). Natural deformation fabrics of plagioclase: implications for slip systems and seismic anisotropy. *Tectonophysics*, *147*(1-2), 145–163. doi: https://doi.org/10.1016/0040-1951(88)90153-9

Shapiro, N. M., Ritzwoller, M. H., Molnar, P., & Levin, V. (2004). Thinning and flow of Tibetan crust constrained by seismic anisotropy. *Science*, *305*(5681), 233–236. doi: https://doi.org/10.1126/science.1098276

Shen, W., & Ritzwoller, M. H. (2016). Crustal and uppermost mantle structure beneath the United States. *Journal of Geophysical Research: Solid Earth*, *121*(6), 4306–4342. doi: https://doi.org/10.1002/2016JB012887

Shirzad, T., & Shomali, Z. H. (2014). Shallow crustal radial anisotropy beneath the Tehran basin of Iran from seismic ambient noise tomography. *Physics of the Earth and Planetary Interiors*, *231*, 16–29. doi: https://doi.org/10.1016/j.pepi.2014.04.001

Skoumal, R. J., Ries, R., Brudzinski, M. R., Barbour, A. J., & Currie, B. S. (2018). Earthquakes induced by hydraulic fracturing are pervasive in Oklahoma. *Journal of Geophysical Research: Solid Earth*, *123*(12), 10–918. doi: doi.org/10.1029/2018JB016790

Sloss, L. L. (1988). *Sedimentary Cover—North American Craton: US.* Geological Society of America.

Sumy, D. F., Cochran, E. S., Keranen, K. M., Wei, M., & Abers, G. A. (2014). Observations of static Coulomb stress triggering of the November 2011 M5. 7 Oklahoma earthquake sequence. *Journal of Geophysical Research: Solid Earth*, *119*(3), 1904–1923. doi: https://doi.org/10.1002/2013JB010612

Takemura, S., Yoshimoto, K., & Shiomi, K. (2021). Long-period ground motion simulation using centroid moment tensor inversion solutions based on the regional three-dimensional model in the Kanto region, Japan. *Earth, Planets and Space*, *73*(1), 1–18. doi: https://doi.org/10.1186/s40623-020-01348-2

Tan, J., Langston, C. A., & Ni, S. (2021). Shallow shear-wave velocity structure in Oklahoma based on the joint inversion of ambient noise dispersion and teleseismic P-wave receiver functions. *Bulletin of the Seismological Society of America*, *111*(2), 654–670. doi: https://doi.org/10.1785/0120200246

Tao, K., Grand, S. P., & Niu, F. (2017). Full-waveform inversion of triplicated data using a normalized-correlation-coefficient-based misfit function. *Geophysical Journal International*, *210*(3), 1517–1524. doi: https://doi.org/10.1093/gji/ggx249

Tao, K., Grand, S. P., & Niu, F. (2018). Seismic structure of the upper mantle beneath eastern Asia from full waveform seismic tomography. *Geochemistry, Geophysics, Geosystems*, *19*(8), 2732–2763. doi: https://doi.org/10.1029/2018GC007460

Tape, C., Liu, Q., Maggi, A., & Tromp, J. (2010). Seismic tomography of the southern California crust based on spectral-element and adjoint methods. *Geophysical Journal International*, *180*(1), 433–462. doi: https://doi.org/10.1111/j.1365-246X.2009.04429.x

Tape, C., Liu, Q., & Tromp, J. (2007). Finite-frequency tomography using adjoint methods—Methodology and examples using membrane surface waves. *Geophysical Journal International*, *168*(3), 1105–1129. doi: https://doi.org/10.1111/j.1365-246X.2006.03191.x

Tarantola, A. (1984). Inversion of seismic reflection data in the acoustic approximation. *Geophysics*, *49*(8), 1259–1266. doi: https://doi.org/10.1190/1.1441754

Thurber, C. H. (1983). Earthquake locations and three-dimensional crustal structure in the Coyote Lake area, central California. *Journal of Geophysical Research: Solid Earth*, *88*(B10), 8226–8236. doi: https://doi.org/10.1029/JB088iB10p08226

Tromp, J., Tape, C., & Liu, Q. (2005). Seismic tomography, adjoint methods, time reversal and banana-doughnut kernels. *Geophysical Journal International*, *160*(1), 195–216. doi: https://doi.org/10.1111/j.1365-246X.2004.02453.x

Virieux, J., & Operto, S. (2009). An overview of full-waveform inversion in exploration geophysics. *Geophysics*, *74*(6), WCC1–WCC26. doi: https://doi.org/10.1190/1.3238367

Walsh, F. R., & Zoback, M. D. (2015). Oklahoma's recent earthquakes and saltwater disposal. *Science advances*, *1*(5), e1500195. doi: https://doi.org/10.1126/sciadv.1500195

Walter, J. I., Ogwari, P., Thiel, A., Ferrer, F., Woelfel, I., Chang, J. C., . . . Holland, A. A. (2020). The Oklahoma Geological Survey Statewide Seismic Network. *Seismological Research Letters*, *91*(2A), 611–621. doi: https://doi.org/10.1785/0220190211

Wang, J., & Zhao, D. (2009). P-wave anisotropic tomography of the crust and upper mantle under Hokkaido, Japan. *Tectonophysics*, *469*(1-4), 137–149. doi: https://doi.org/10.1016/j.tecto.2009.02.005

Wang, J., & Zhao, D. (2013). P-wave tomography for 3-D radial and azimuthal anisotropy of Tohoku and Kyushu subduction zones. *Geophysical Journal International*, *193*(3), 1166–1181. doi: https://doi.org/10.1093/gji/ggt086

Wang, K., Jiang, C., Yang, Y., Schulte-Pelkum, V., & Liu, Q. (2020). Crustal deformation in Southern California constrained by radial anisotropy from ambient noise adjoint tomography. *Geophysical Research Letters*, *47*(12), e2020GL088580. doi: https://doi.org/10.1029/2020GL088580

Wang, X., & Zhan, Z. (2020). Moving from 1-D to 3-D velocity model: automated waveform-based earthquake moment tensor inversion in the Los Angeles region. *Geophysical Journal International*, *220*(1), 218–234. doi: https://doi.org/10.1093/gji/ggz435

Warner, M., & Guasch, L. (2016). Adaptive waveform inversion: Theory. *Geophysics*, *81*(6), R429–R445. doi: https://doi.org/10.1190/geo2015-0387.1

Whitaker, A. E., & Engelder, T. (2006). Plate-scale stress fields driving the tectonic evolution of the central Ouachita salient, Oklahoma and Arkansas. *Geological Society of America Bulletin*, *118*(5-6), 710–723. doi: https://doi.org/10.1130/B25780.1

Wu, R.-S., Luo, J., & Wu, B. (2014). Seismic envelope inversion and modulation signal model. *Geophysics*, *79*(3), WA13–WA24. doi: https://doi.org/10.1190/geo2013-0294.1

Xu, C., Cronin, T. P., McGinness, T. E., & Steer, B. (2009). Middle Atokan sediment gravity flows in the Red Oak field, Arkoma Basin, Oklahoma: A sedimentary analysis using electrical borehole images and wireline logs. *AAPG bulletin*, *93*(1), 1–29. doi: https://doi.org/10.1306/09030808054

Yan, F., Han, D.-H., Sil, S., & Chen, X.-L. (2016). Analysis of seismic anisotropy parameters for sedimentary strata. *Geophysics*, *81*(5), D495–D502. doi: https://doi.org/10.1190/geo2016-0062.1

Yang, Y., & Engquist, B. (2018). Analysis of optimal transport and related misfit functions in full-waveform inversion. *Geophysics*, *83*(1), A7–A12. doi: https://doi.org/10.1190/geo2017-0264.1

Yu, Y., Song, J., Liu, K. H., & Gao, S. S. (2015). Determining crustal structure beneath seismic stations overlying a low-velocity sedimentary layer using receiver functions. *Journal of Geophysical Research: Solid Earth*, *120*(5), 3208–3218.

doi: https://doi.org/10.1002/2014JB011610

Zhang, C., Yao, H., Liu, Q., Zhang, P., Yuan, Y. O., Feng, J., & Fang, L. (2018). Linear array ambient noise adjoint tomography reveals intense crust-mantle interactions in North China Craton. *Journal of Geophysical Research: Solid Earth*, *123*(1), 368–383. doi: https://doi.org/10.1002/2017JB015019

Zhu, H. (2018). Crustal wave speed structure of North Texas and Oklahoma based on ambient noise cross-correlation functions and adjoint tomography. *Geophysical Journal International*, *214*(1), 716–730. doi: https://doi.org/10.1093/gji/ggy169

Zhu, H., Bozdağ, E., & Tromp, J. (2015). Seismic structure of the European upper mantle based on adjoint tomography. *Geophysical Journal International*, *201*(1), 18–52. doi: https://doi.org/10.1093/gji/ggu492

Zhu, H., & Fomel, S. (2016). Building good starting models for full-waveform inversion using adaptive matching filtering misfit. *Geophysics*, *81*(5), U61–U72. doi: https://doi.org/10.1190/geo2015-0596.1

Zhu, H., Komatitsch, D., & Tromp, J. (2017). Radial anisotropy of the North American upper mantle based on adjoint tomography with USArray. *Geophysical Journal International*, *211*(1), 349–377. doi: https://doi.org/10.1093/gji/ggx305

Constructing a 3-D radially anisotropic crustal velocity model for Oklahoma using full waveform inversion

Shuo Zhang[1] and Hejun Zhu[1,2]

[1]Department of Geosciences, The University of Texas at Dallas
[2]Department of Physics, The University of Texas at Dallas

Key Points:

- We use induced earthquakes and full waveform inversion to construct a 3-D radially anisotropic seismic velocity for the crust of Oklahoma.
- Spatial distributions of inverted velocity and radial anisotropy agree with geological provinces and tectonic deformation in Oklahoma.
- Lateral velocity heterogeneities have strong impacts on earthquake location, especially for epicentral depths.

Abstract

Over the past decade, the seismicity rate in the state of Oklahoma has increased significantly, which has been linked to industrial operations, such as saltwater injection. Taking advantage of induced earthquakes and recently deployed seismometers, we construct a 3-D radially anisotropic seismic velocity model for the crust of Oklahoma by using full waveform inversion. To mitigate the well-known cycle-skipping problem, we use misfit functions based on phase and waveform differences in several frequency bands. Relative velocity perturbations in the inverted model allow us to delineate major geological provinces in Oklahoma, such as the Anadarko and Arkoma Basins, as well as the Cherokee Platform and Shelf. In addition, radial anisotropy in the inverted model reflects deformation within the crust of Oklahoma, which might correlate with sedimentary layers, micro-cracks/fractures, as well as the dominant orientation of anisotropic minerals. The crystalline basement beneath Oklahoma can be inferred from the new velocity model, which enables us to better classify induced seismicity in current earthquake catalogs. Furthermore, synthetic experiments suggest that the new velocity model enables us to better constrain earthquake location in Oklahoma, especially for determining their depths, which are important for investigating induced seismicity.

Plain Language Summary

Taking advantage of induced earthquakes and seismometers deployed in Oklahoma in the last decade, we construct a radially anisotropic seismic model for the crust beneath Oklahoma by using full waveform inversion. The data misfit is iteratively reduced by about 40%, and predicted seismograms associated from the new velocity model can fit observations very well. We can identify geological structures from the velocity model, such as low velocity anomalies associated with the Anadarko Basin, and fast anomalies relative to the Cherokee Platform. Positive radial anisotropy in the shallow crust might reflect layered structure of sedimentary, while the negative radial anisotropy with the middle crust may relate to preferred orientation of anisotropic minerals, such as plagioclase, mica and amphibole. Furthermore, synthetic tests are used to illustrate the impact of lateral variations of seismic velocity on earthquake locations, especially for epicentral depths. Therefore, this new 3-D model provides us an opportunity to improve current catalogs of earthquakes in Oklahoma, and improve our understanding about the triggering mechanism of induced earthquakes.

1 Introduction

Located in the middle of the North American Plate, the state of Oklahoma is dominated by east-west oriented tectonic stress for a long time and results in its widespread crustal deformation (Whitaker & Engelder, 2006; Almqvist & Mainprice, 2017; Lund Snee & Zoback, 2020). Due to its comparatively stable tectonic condition, seismicity in this area remains relatively low for decades. However, since 2008, seismologists observed a significant increase in seismicity in the state of Oklahoma, which reached a peak level around 2016 and then gradually decreased to a normal level. To date, many studies have attributed these unexpected earthquakes as induced seismicity related to industry activities, such as saltwater injection (Ellsworth, 2013; Walsh & Zoback, 2015; X. Chen et al., 2018) and hydraulic fracturing (Holland, 2013a; Rubinstein & Mahani, 2015; Skoumal et al., 2018). During this time, the 2011 Mw 5.7 Prague earthquake (Keranen et al., 2013; Sumy et al., 2014) and the 2016 Mw 5.8 Pawnee earthquake (Barbour et al., 2017; Pennington & Chen, 2017) are the two largest earthquakes ever occurred in Oklahoma, resulting in severe damage to the local community and infrastructure. In order to monitor these unusual seismic activities, many seismometers have been deployed in Oklahoma (Walter et al., 2020), giving us an opportunity to use seismic tomography to study the crustal structure of Oklahoma.

An accurate 3-D crustal velocity model is important for earthquake source estimations. With 1-D seismic velocity profiles and dense arrays in Oklahoma, several earthquake catalogs have been developed (Schoenball & Ellsworth, 2017; Cramer et al., 2017; Mueller, 2019), which enable us to delineate some previously unmapped 3-D fault systems in Oklahoma (Holland, 2013b; McNamara et al., 2015; Schoenball & Ellsworth, 2017). However, there are still a lot of randomly distributed earthquakes in these catalogs that cannot be directly linked to any fault systems. A number of studies have illustrated the impacts of lateral crustal velocity heterogeneities on earthquake location (Thurber, 1983; Michelini & Lomax, 2004; Font et al., 2013; Zhu, 2018), as well as moment tensor solutions (Q. Liu et al., 2004; X. Wang & Zhan, 2020; Takemura et al., 2021). Both of them are critical for studying earthquake triggering processes and delineating fault geometry in the subsurface. To date, there are few community-shared 3-D crustal velocity models in Oklahoma that can be used to potentially improve the accuracy of current earthquake catalogs and better delineate fault geometry (Tan et al., 2021).

Seismic tomography is a classical method to construct velocity models from seismic data recorded at the Earth's surface. The idea of iteratively constraining seismic model parameters by minimizing mismatches between observations and predictions has been proposed for a long time (Lailly & Bednar, 1983; Tarantola, 1984). Tromp et al. (2005) recognized the generality of using the adjoint-state method in seismic tomography, which combines high-quality seismic recordings with numerical modeling to map the spatial distribution of seismic parameters. So far, full waveform inversion (FWI) has been widely utilized to constrain crustal and upper mantle structures in California (Tape et al., 2010; K. Wang et al., 2020), Alaska (G. Chen et al., 2023), Austrilia (Fichtner et al., 2009), New Zealand (Chow et al., 2020), Europe (Fichtner et al., 2013; Zhu et al., 2015), Eastern Asia (M. Chen et al., 2017; Tao et al., 2018; Zhang et al., 2018), North America (Zhu et al., 2017), Antarctic (A. Lloyd et al., 2020), North Atlantic (Rickers et al., 2013), and the entire Earth (French & Romanowicz, 2014; Lei et al., 2020), etc.

In order to better investigate induced seismicity in Oklahoma, we construct a 3-D seismic velocity model for the crust of Oklahoma by fully exploiting three-component seismograms collected over the past several years. The lateral variations of seismic velocity and radial anisotropy in the inverted model can be used to investigate geological structures and deformation in Oklahoma (Fouch & Rondenay, 2006; J. Wang & Zhao, 2009; Long, 2013). In this paper, we first briefly review the tectonic evolution of the crust beneath Oklahoma in section 2. The datasets and the initial model used in the inversion are introduced in section 3. Section 4 presents determinations of misfit functions, model parameterizations, and kernel processing. We illustrate the improvements in both data and model domains in section 5. Section 6 discusses the reliability of the inverted model, potential origins of radial anisotropy, depths of the crystalline basement, and impact of velocity heterogeneities on earthquake locations.

2 Brief Introduction of Tectonic Evolution in Oklahoma

Oklahoma has experienced a long tectonic evolution history over the past 1.4 billion years, which forms its present-day crustal and lithospheric structure (Johnson & Luza, 2008). Since the Precambrian period, geological structures beneath Oklahoma experienced numerous cycles of continental collision and rifting (Johnson & Luza, 2008). The oldest rocks found in Oklahoma are Precambrian igneous and metamorphic rocks that formed about 1.4 billion years ago (Sloss, 1988). Before being covered by shallow sea-water in the early Paleozoic, the surface of Oklahoma was exposed and partly eroded (Hamilton, 1956). Due to the circulations of deposition and erosion during Silurian and Devonian (Chenoweth, 1968), multiple thin layers of black shale overlay on limestone and dolomite. Thick sedimentary layers were formed after rapid subsidence in the Carboniferous period (Johnson & Luza, 2008), with most petroleum reservoirs found in Pennsylvanian shale in Oklahoma (Ball et al., 1991). Most of Oklahoma was above sea level by the Triassic and Jurassic periods, which was then overlapped by the Cretaceous Sea. The weathered and loose surface of Oklahoma, which was contributed by shale, sandstone, and limestone, were characterized as the Quaternary sedimentary.

To date, the principal mountain belts, including the Ouachita, the Arbuckle, and the Wichita mountains are located around the Southern Oklahoma Aulacogen, while the Anadarko, the Arkoma, the Ardmore, and the Ouachita basins received sediments with 2 to 12 km thickness (Johnson, 1996) (Figure 1A). The Anadarko basin is one of the major tectonic provinces in Oklahoma (Evans, 1979), with sedimentary rocks ranging from the Cambrian to the Permian periods. The thickest sedimentary column, in excess of 12 km, is detected at the southern edge of the Anadarko basin, with the average thickness of the basin around 4.6 km (Kolawole et al., 2020). In contrast, the sedimentary thickness goes down to 0.6 km on the northern and western flanks of the basin, as well as the Cherokee shelf and platform (Mitchell & Landisman, 1970). To date, the Anadarko Basin is one of the largest oil production zones in America (Higley et al., 2014).

3 Databases and The Initial Model

3.1 Distributions of Earthquakes and Seismometers

We collect centroid moment tensor (CMT) solutions for earthquakes that occurred between 2010 and 2018 (Figure 1D) from the Earthquake Center of St. Louis University (SLU; `https://www.eas.slu.edu/eqc/eqc.html`). These CMT solutions are jointly inverted by using surface-wave spectrum amplitudes, radiation patterns, waveforms, and first motions (Herrmann, 2013). In total, 153 earthquakes from the SLU catalog are used in this study (Figure 1B), most of which are distributed around the Nemaha and Wilzetta strike-slip fault zones with depths around 5 km (Figure 1E). They are small- to moderate-sized earthquakes with magnitudes ranging from 3.4 to 4.8 (Figure 1F).

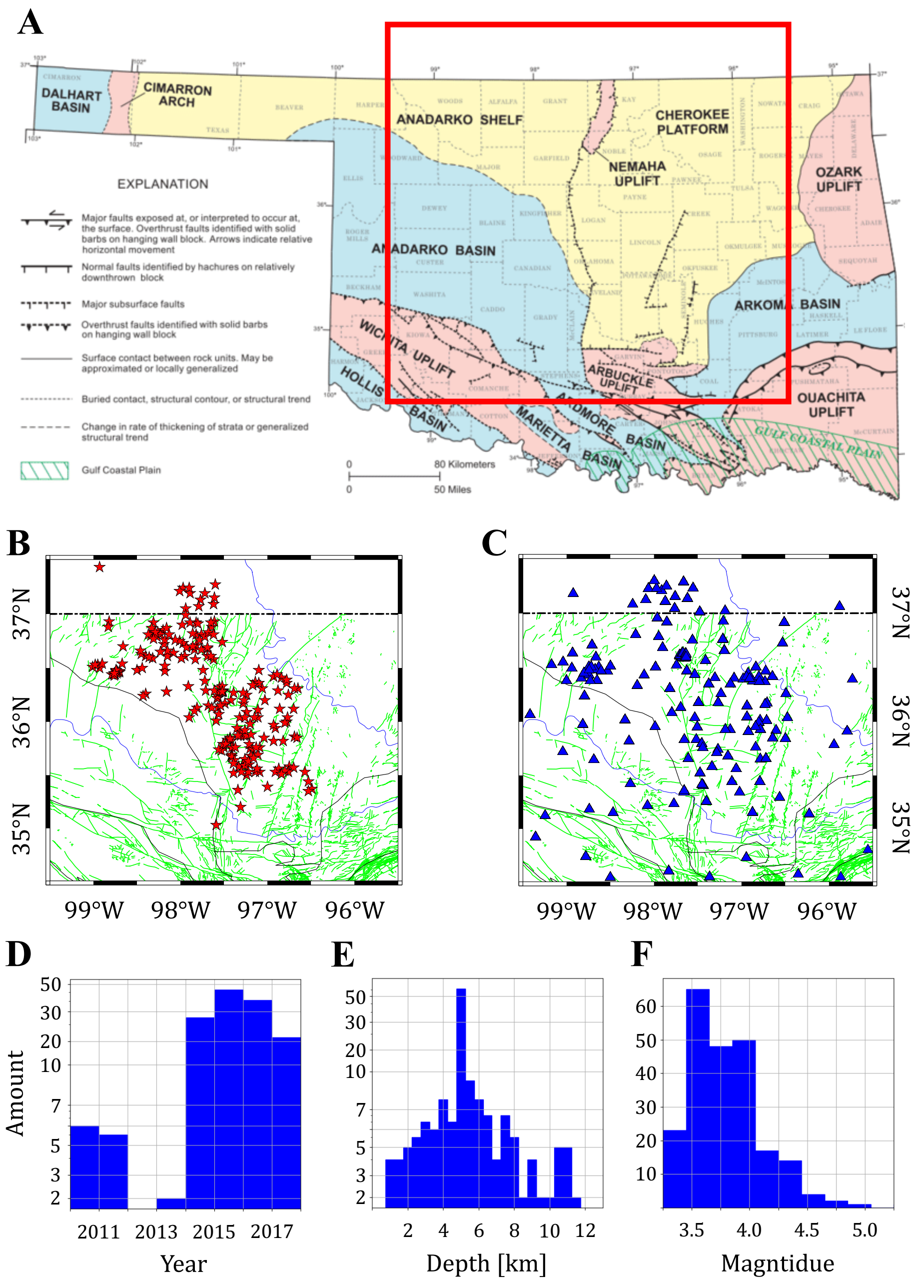

Figure 1. Tectonic map and distributions of earthquakes and stations used in this study. Panel A shows the simplified geological map modified from Northcutt and Campbell (1996). The red box represents the inversion region in this study. Panels B and C demonstrate the locations of 153 earthquakes (red stars) and 176 available stations (blue triangles). Green lines in panels B and C represent fault traces mapped at the Earth's surface (Marsh & Holland, 2016), while thin black lines delineate geological provinces shown in panel A. Panels D to F show the histograms of occurring times, depths and magnitudes of collected earthquakes from the SLU catalog.

Three-component waveform recordings for these events are downloaded from the Data Management Center of the Incorporated Research Institutions of Seismology (IRIS-DMC). The USArray Transportable Array (TA) covered the study region from 2010 to 2012, after which a number of temporary arrays have been deployed to monitor the increasing seismicity in Oklahoma. In total, 176 seismographic stations are used in this study (Figure 1C), allowing us to achieve a dense ray sampling for the state of Oklahoma.

3.2 The Initial Model and Spectral Element Mesh

We use a 3-D isotropic velocity model as the initial model, which was constructed by using adjoint tomography to fit vertical-vertical component ambient noise cross-correlation functions with a 5-40 s frequency band (Zhu, 2018). It gives us good fits for long-period surface waves with relatively low spatial resolutions, but does not include shallow sedimentary layers due to the limited frequency bands. Here, we incorporate a shallow layer (<1.5 km) from Shen and Ritzwoller (2016) into the starting model in order to represent sediments with slow seismic velocities in Oklahoma. The interface of these two models (at 1.5 km depth) is smoothed by a Gaussian filter with standard deviation $\sigma = 200\ m$, in order to avoid any artificial reflections. The simulation domain includes central and northern Oklahoma, as well as southern parts of Kansas, ranging from $34.5°\ N$ to $37.5°\ N$ in latitude and $99.5°\ W$ to $95.5°\ W$ in longitude. The Moho depths of the study region vary from 38 to 44 km (Keller, 2013), thus, our model is truncated at 50 km depth. The Earth's surface is comparatively flat in Oklahoma, ranging from 200 to 600 m (Amante & Eakins, 2009).

SPECFEM3D_Cartesian is used to calculate forward and adjoint wavefields with the spectral element method (Komatitsch & Tromp, 1999; Peter et al., 2011). Topography from ETOPO1 (Amante & Eakins, 2009) is incorporated into the discretized spectral-element mesh. The entire mesh includes 428,544 spectral elements and 28,340,784 Gauss-Lobatto-Legendre grid points. The minimum resolvable period is around 1.61 s and the minimum element size is approximately 1.25 km at the Earth's surface. With 128 cores on the Lonestar 6 cluster at the Texas Advanced Computing Center (TACC), it takes 48 minutes to perform one forward simulation and approximately 2 hours for calculating misfit gradients for each individual event.

4 Method

4.1 Choices of Misfit Functions

The specific misfit function in FWI determines the purposes and eventual performance of the inversion (Tromp et al., 2005). In the last decades, a variety of misfit functions have been designed based on travel-times differences (Luo & Schuster, 1991), surface wave dispersion curves (Beaty et al., 2002; Dal Moro et al., 2007), envelopes differences (Bozdağ et al., 2011; Wu et al., 2014), dynamic wrapping functions (Ma & Hale, 2013), adaptive matching filters (Warner & Guasch, 2016; Zhu & Fomel, 2016), cross-correlation functions (Y. Liu et al., 2017; Tao et al., 2017), Wasserstein distances (Métivier et al., 2016; Yang & Engquist, 2018), etc. Among them, the L2 norm of waveform differences is the classical misfit to constrain seismic velocity models. However, it suffers from nonlinearity and cycle-skipping problems (Virieux & Operto, 2009). In order to mitigate these difficulties, two misfit functions based on phase and waveform differences are used in this study. Here, FLEXWIN is applied to automatically select useful windows, which allows us to compare phase shifts, STA/LTA, as well as envelopes of observed and predicted waveforms (Maggi et al., 2009).

We first update the velocity models by reducing phase differences. Here, frequency-dependent phase differences are measured by using a multi-taper technique (Tape et al., 2010),

$$\chi_1 = \frac{1}{2} \sum_s \sum_r \sum_m N_m \int \left[\frac{\Delta\tau_m(\omega)}{\sigma_m(\omega)} \right]^2 \mathrm{d}\omega \quad , \tag{1}$$

where $\Delta\tau_m$ denotes the phase difference between observations and predictions for m component, and σ_m is the associated uncertainty of the phase measurement. ω is the angular frequency, N_m denotes the weighting factor to balance the contributions of different components. The total misfit (Equation 1) is the summation over all earthquakes s, stations r, and wave components m. To further mitigate the nonlinearity of FWI, a multi-scale strategy (Bunks et al., 1995) is applied via inverting the velocity model using three different frequency bands, 10-30 s, 5-30 s, and 2-30 s, sequentially.

Once the travel-time differences between observed and predicted waveforms are less than half period of the dominate frequency, we switch to the L2 waveform misfit as,

$$\chi_2 = \frac{1}{2}\int \left[\hat{d}(t) - \hat{s}(t)\right]^2 \mathrm{d}t \quad , \tag{2}$$

where $\hat{d}(t)$ and $\hat{s}(t)$ denote the normalized observations and predictions, in order to mitigate potential errors for moment magnitude from CMT solutions. This second waveform-based misfit enables us to further improve the spatial resolution of the inversion.

4.2 Model Parameterization

Radial anisotropy, with five indenpendent elastic constants (C_{11}, C_{13}, C_{33}, C_{44}, C_{66}), is introduced in the model update to solve the Rayleigh-Love discrepancy (Anderson, 1961; Harkrider, 1964; Debayle & Kennett, 2000). Since the phase measurements are more sensitive to wavespeeds, we use the following five model parameters,

$$\begin{aligned}
\alpha_{\mathrm{h}} &= \sqrt{\frac{C_{11}}{\rho}} \quad , \\
\alpha_{\mathrm{v}} &= \sqrt{\frac{C_{33}}{\rho}} \quad , \\
\beta_{\mathrm{h}} &= \sqrt{\frac{C_{66}}{\rho}} \quad , \\
\beta_{\mathrm{v}} &= \sqrt{\frac{C_{44}}{\rho}} \quad , \\
\eta &= \frac{C_{13}}{C_{11} - 2C_{44}} \quad .
\end{aligned} \tag{3}$$

where ρ stands for the density. α_{h} and α_{v} are the velocities of horizontally and vertically polarized P-wave. β_{h} and β_{v} are the velocities of horizontally and vertically polarized S-wave. η is the radial anisotropy parameter.

The mass density ρ is approximated by the following empirical relationship,

$$\delta \ln\rho = 0.33 \ln\beta \quad , \tag{4}$$

where the Voigt average of isotropic compressional- and shear-wave velocities, α and β, can be computed as

$$\alpha = \sqrt{\frac{2\alpha_{\mathrm{h}}^2 + \alpha_{\mathrm{v}}^2}{3}} \quad ,$$

$$\beta = \sqrt{\frac{2\beta_{\mathrm{h}}^2 + \beta_{\mathrm{v}}^2}{3}} \quad . \tag{5}$$

We define the radial anisotropy (RA) as,

$$RA = \frac{\beta_{\mathrm{h}} - \beta_{\mathrm{v}}}{\beta} \quad , \tag{6}$$

For each iteration, four model parameters, α_{h}, α_{v}, β_{h}, and β_{v}, are updated simultaneously. Thus, the misfit perturbation can be expressed as a volumetric integral over relative perturbations of these four model parameters as

$$\delta\chi = \int_V K_{\alpha_{\mathrm{h}}} \delta\ln\alpha_{\mathrm{h}} + K_{\alpha_{\mathrm{v}}} \delta\ln\alpha_{\mathrm{v}} + K_{\beta_{\mathrm{h}}} \delta\ln\beta_{\mathrm{h}} + K_{\beta_{\mathrm{v}}} \delta\ln\beta_{\mathrm{v}} \mathrm{d}V \quad , \tag{7}$$

where $K_{\alpha_{\mathrm{h}}}$, $K_{\alpha_{\mathrm{v}}}$, $K_{\beta_{\mathrm{h}}}$ and $K_{\beta_{\mathrm{v}}}$ are the misfit gradients with respect to four radially anisotropic elastic model parameters.

We use the approximated inverse of the diagonal Hessian as the pre-conditioner to balance amplitudes at shallow and deeper depths, and mitigate singular values at source and receiver locations (Luo, 2012; Luo et al., 2015),

$$P(\mathbf{x}) = \frac{1}{\int \partial^2 \mathbf{s}(\mathbf{x}, t) \cdot \partial^2 \mathbf{s}^{\dagger}(\mathbf{x}, T - t) \mathrm{d}t} \quad , \tag{8}$$

where $\mathbf{s}$ and $\mathbf{s}^{\dagger}$ denote the forward and adjoint displacement wavefields, respectively.

We also employ a 3-D Gaussian function to smooth the preconditioned kernels. Its standard deviation varies with the dominant wavelength of the inversion. A conjugate-gradient method is utilized to update the model parameters (Fletcher & Reeves, 1964; Matthies & Strang, 1979), with the step length determined by a quadratic interpolation (Tape et al., 2007).

5 Results

5.1 Waveform Fitting

Taking one earthquake occurred in November 8th 2015 as an example (Figure 2A), we compare observed and predicted seismograms to demonstrate the performance of the inversion. The locations and azimuthal distributions of recorded seismometers are shown in Figures 2A and C. Compared with results from the initial model (Figures 3A and S1 in Supporting Information), simulations from the new model fit observed waveforms much better. For instance, for short epicentral distances, predictions can perfectly match observations, while there are still some residuals for longer epicentral distances. Other than fundamental mode surface waves, the inverted model can also reproduce higher-mode oscillations, which can be clearly observed in 5-30 s and 2-30 s frequency bands (Figures 2B and S2 in Supporting Information). For further comparisons, we also simulate wave propagation with the same earthquake and corresponding stations by using a 1-D velocity profile (OGS-1D) provided by the Oklahoma Geological Survey (Darold et al., 2015). For short epicentral distances, the OGS-1D model provides comparably good fittings with observed data, however, it fails to fit observations with long epicentral distances (Figures 3C and S3 in Supporting Information). More details on waveform comparisons with different velocity models can be found in Section S1 of Supporting Information.

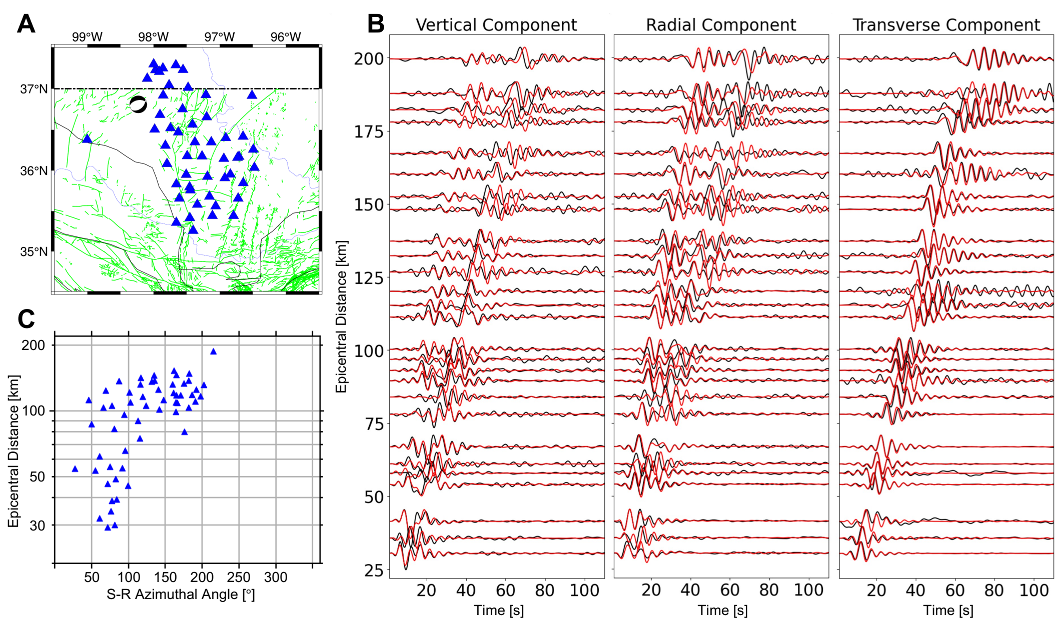

Figure 2. Comparison between observed (black) and predicted (red) waveforms based on the inverted model. The particular earthquake (beachball) and corresponding seismometers (triangle) are shown in panel A. Comparisons of vertical, radial, and transverse component seismograms (with 5-30 s passband) are shown from left to right in panel B. Panel C illustrates the distributions of azimuthal angles and epicentral distances for selected seismograms.

Beyond this particular event, we also present the evolution of data residuals in Figure 4A. In order to mitigate the cycling-skipping problem, three frequency bands, 10-30 s, 5-30 s, 2-30 s, are applied sequentially, with the same phase-based misfit (Equation 1). It is then followed by another five iterations with the L2 norm waveform-based misfit (Equation 2) in 5-30 s frequency band. Because of different frequency bands and misfits, these four stages are not directly comparable. Therefore, we normalize the data misfit within each individual stage for a better comparison. When using the phase-based misfit in 10-30 s (Figure 4A), the data misfit is reduced by about 30% for each individual component. While for higher frequency bands (5-30 s and 2-30 s), the phase difference of the transverse component decreases much faster than the other two components. The data misfit is reduced by around 25% after using the phase-based misfit. In contrast, after switching to the L2 norm waveform misfit in the last five iterations, we observe a larger misfit reduction for vertical and radial components (22%) than the transverse component (13%).

The robustness of the inversion in the data domain can be further illustrated by comparing the histograms of time shifts between the initial and inverted models (Figures 4B-D). The isotropic initial velocity model (Zhu, 2018) still produces 0.5-1.0 s mean travel time errors for three components in the frequency band of 2-30 s. The inverted model enables us to reduce the averaged travel-time error to less than 0.2 s. For instance, the mean traveltime error for the vertical component is reduced from 1.09 s to 0.19 s. In addition, FLEXWIN can detect more windows for the inverted model than the initial model, because of the improvement of overall waveform match. For instance, the total number of detected time windows for the radial component is increased from 1,140 to 2,099 after the inversion.

5.2 3-D Isotropic Shear Wave Velocity Model

We first compute the 1-D velocity profile (FWI-1D) by averaging lateral heterogeneities of the inverted 3-D model, and compare it with OGS-1D in Figure 5A. Starting from slow sedimentary layers with $V_p = 3.0\ km/s$ and $V_s = 1.7\ km/s$, both FWI-1D and OGS-1D consistently increase with depths. Large discrepancies exist between 2 to 7 km, with FWI-1D being slower than OGS-1D by about 9% in P-wave velocity and 3% in S-wave velocity. Considering better waveform comparisons as shown in Figures 3B and C, this comparatively slow velocity at depths of 4-7 km in FWI-1D (Figure 5A) is

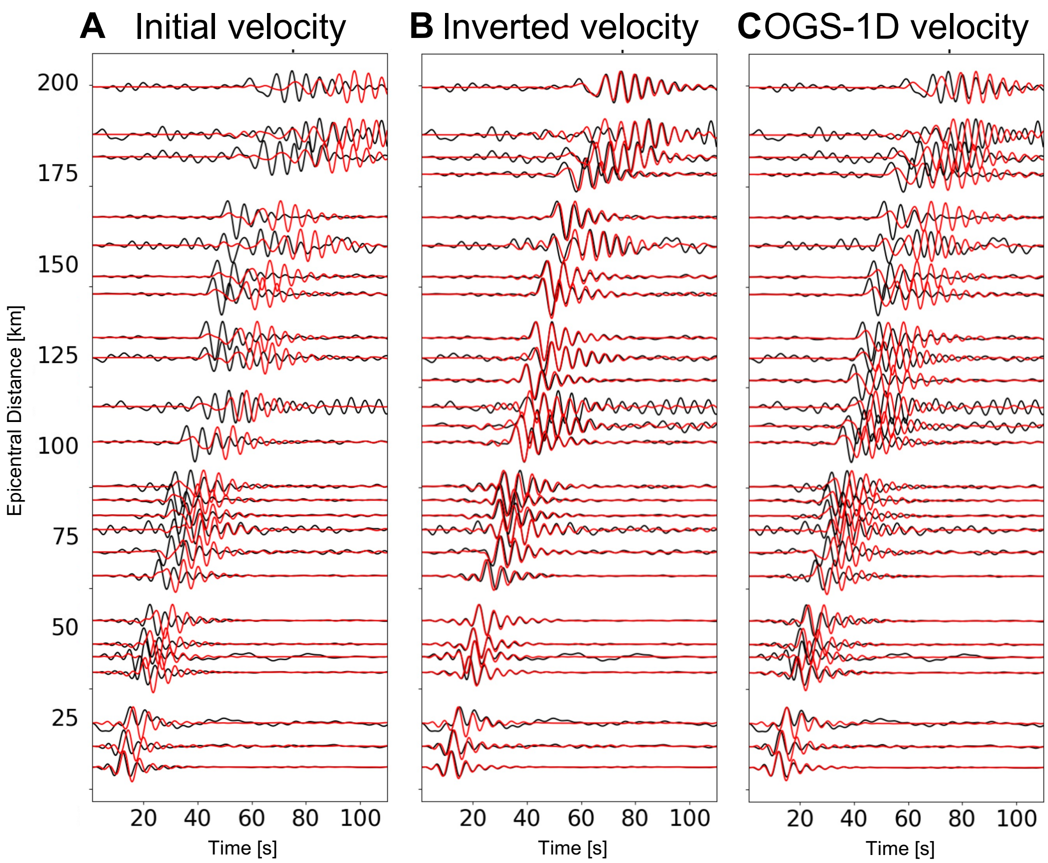

Figure 3. Comparison between transverse component observed (black) and predicted (red) seismograms from different velocity models. Locations of the earthquake and corresponding seismometers are shown in Figure 2A. Panels A to C are resulted from the initial model, inverted model, and OGS-1D profile (Darold et al., 2015), respectively. All seismograms are filtered with 5-30 s passband.

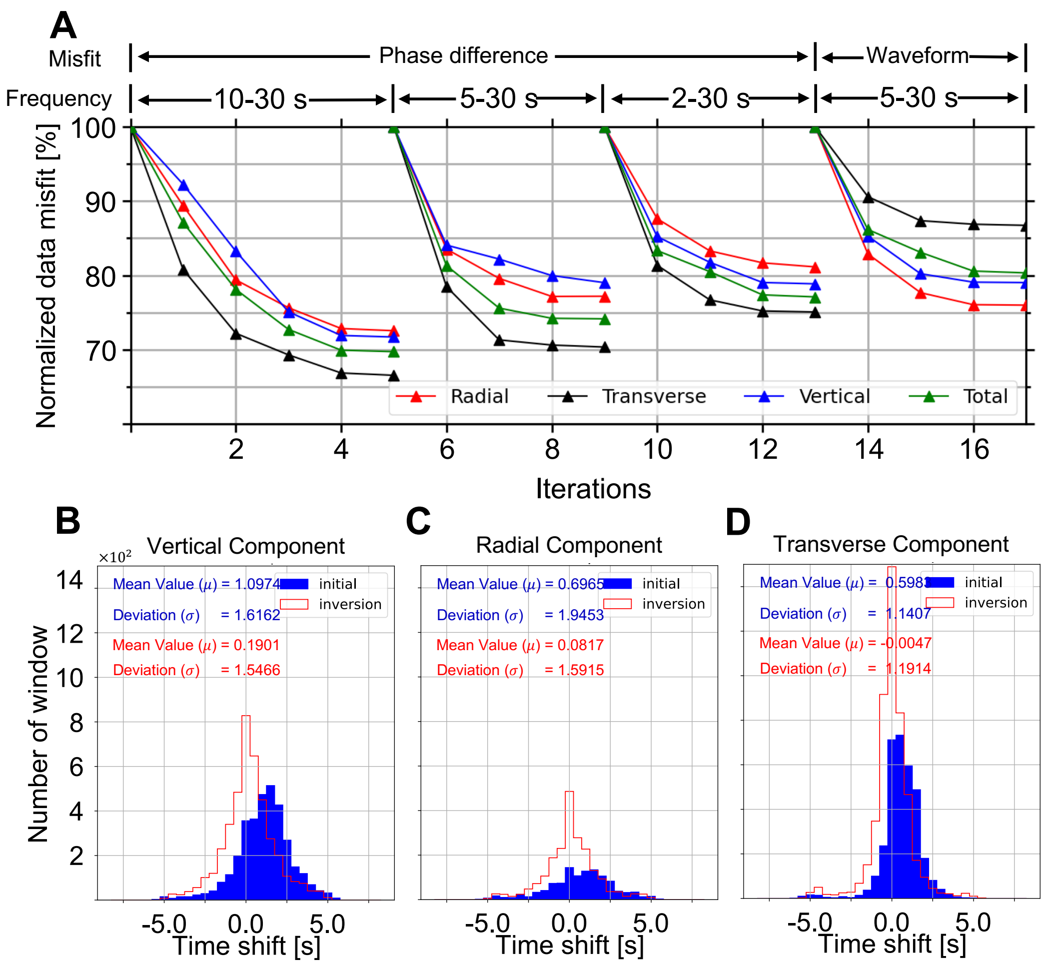

Figure 4. Comparisons of data residuals and travel time histograms. Panel A shows the evolution of data residuals with four stages of total 17 iterations, with different frequency bands and misfit functions. The data misfits are normalized within each individual stage for better comparison. Panels B-D compare the histograms of travel-time differences between three components, observed and predicted seismograms from the initial (blue) and inverted (red) velocity models.

required for waveform fitting. These two 1D velocity profiles are basically consistent with each other in the middle crust. Because of limited frequencies and ray-path coverage, our inversion is not sensitive to velocity perturbations at depths greater than 30 km.

We also compute relative velocity perturbations (Figures 5B-E), with respect to FWI-1D by using $V_{rel} = \ln \frac{V_{3D}}{V_{1D}}$. Two major features can be observed within the uppermost crust (Figure 5B), with slow anomalies for basin areas and fast anomalies for the Cherokee Shelf and Platform. In vertical profiles, the depths of the fast anomaly change from 10 km in the Cherokee Shelf (Figures 6G and I) to less than 5 km in the Cherokee Platform (Figure 6G), which basically agree with geological survey results (Northcutt & Campbell, 1996; Johnson & Luza, 2008; Xu et al., 2009).

In contrast to the fast Cherokee Shelf and Platform, the Anadarko and Arkoma Basins are fulfilled with sandstone and shale after frequent erosion and deposit (Johnson & Luza, 2008), where seismic velocity perturbations are imaged as slow as -10%. In addition, porous and layered structures in these sedimentary basins might further slow down the apparent velocity due to attenuation and scattering effects (Houtz & Ludwig, 1979; Sams et al., 1997; Yu et al., 2015). The NE-SW distribution of the slow velocity anomaly is consistent with the geological boundaries of the Anadarko Basin (Perry, 1989). Similar observations can also be obtained for the Arkoma Basin. The wedge shape of the slow velocity anomaly in the Anadarko Basin, with the lower bound at about 15 km (Figure 6H and I), is consistent with geological investigations (Perry, 1989; Ball et al., 1991; Northcutt & Campbell, 1996). Another fast velocity anomaly can be observed in the middle crust beneath slow basins in Figure 6H, which might be related to the Arbuckle Uplift (Johnson & Luza, 2008) in south Oklahoma.

5.3 Radial Anisotropy

The magnitude of RA, defined by Equation 6, ranges from -5% to +5% in our inverted model. Two large RA anomalies are imaged, a large negative anomaly within the middle crust is overlain by a positive anomaly in the uppermost crust (Figures 5J-L). The positive perturbation is located around the Nemaha-Wilzetta Fault System, which connects the Cherokee Shelf in the west and the Cherokee Platform in the east (Figure 5F). In spite of its large amplitude (+5%), this positive RA is comparatively thin. Underneath

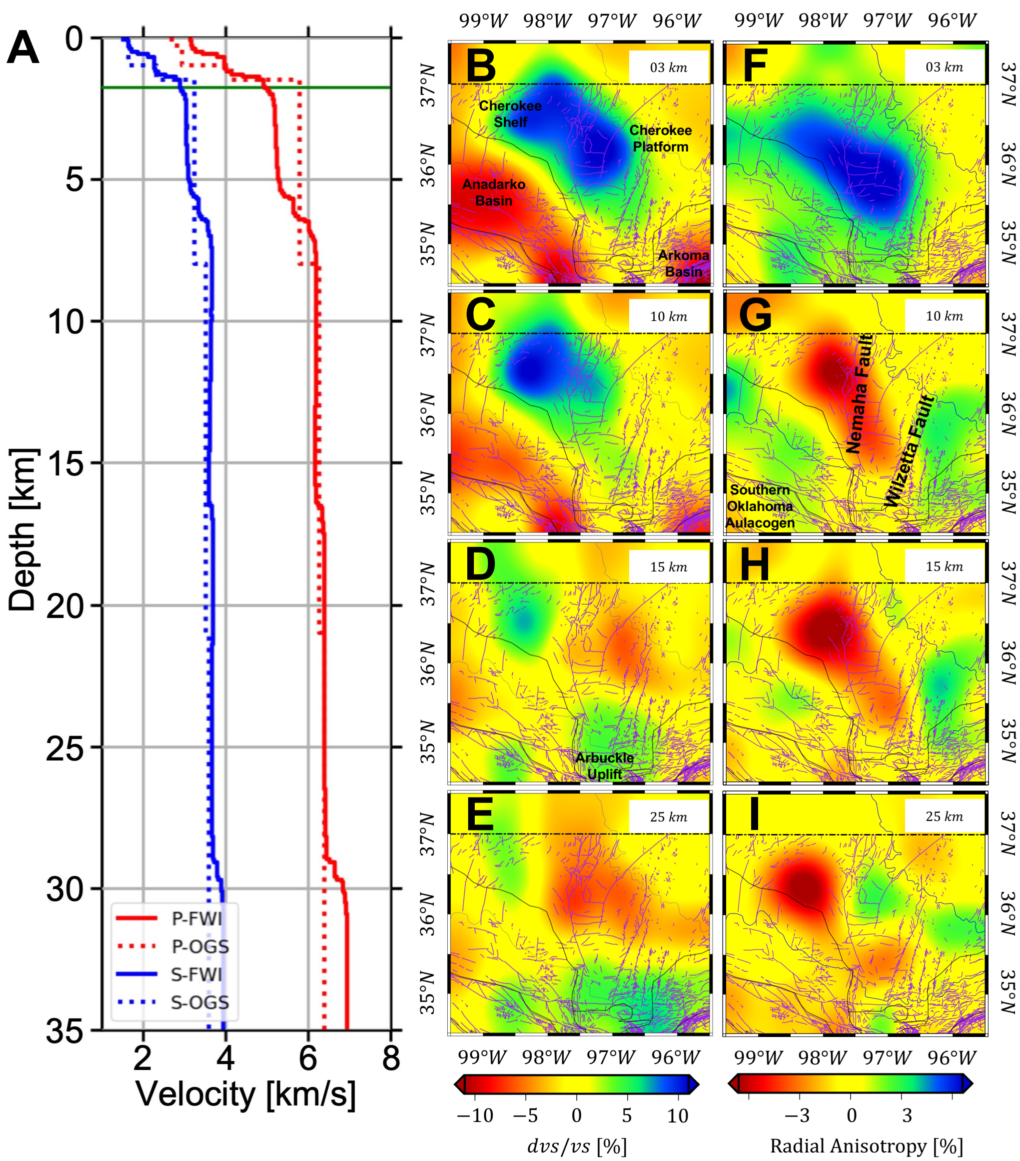

Figure 5. Vertical and horizontal variations of seismic velocities within the inverted model. Panel A compares absolute P (red) and S (blue) wave velocities from OGS-1D (dashed) and FWI-1D (solid) profiles. Panels B to E show relative S velocity variations at depths of 3, 10, 15 and 25 km. Corresponding radial anisotropy at these depths are shown in panels F to I.

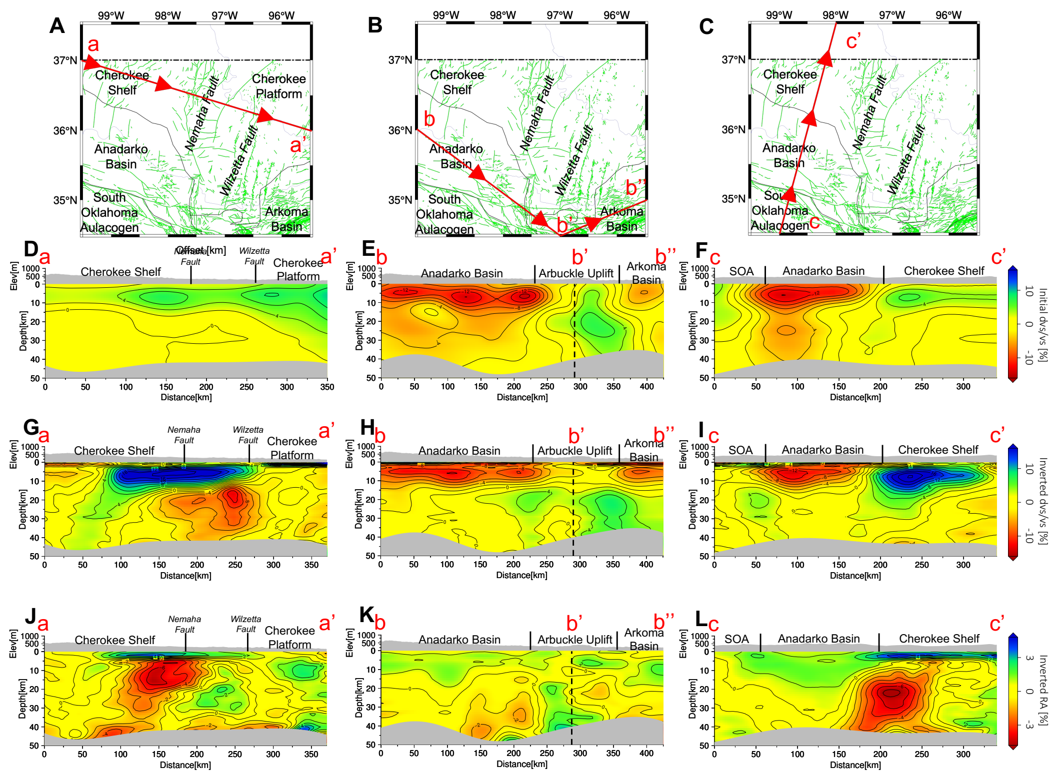

Figure 6. Vertical cross sections of the initial and inverted models and their radial anisotropy. Panels D, G and J are extracted from line a-a' in panel A. Panels E, H and K are extracted from line b-b'-b" in panel B, where the dashed lines indicate the turning point b'. Panels F, I and L are extracted from line c-c' in panel C. Panels D, E and F illustrate shear wave velocity perturbations from the initial velocity model. Panels G, H and I show relative shear wave velocity perturbations from the inverted velocity model. Panels J, K and L are radial anisotropy in the inverted model.

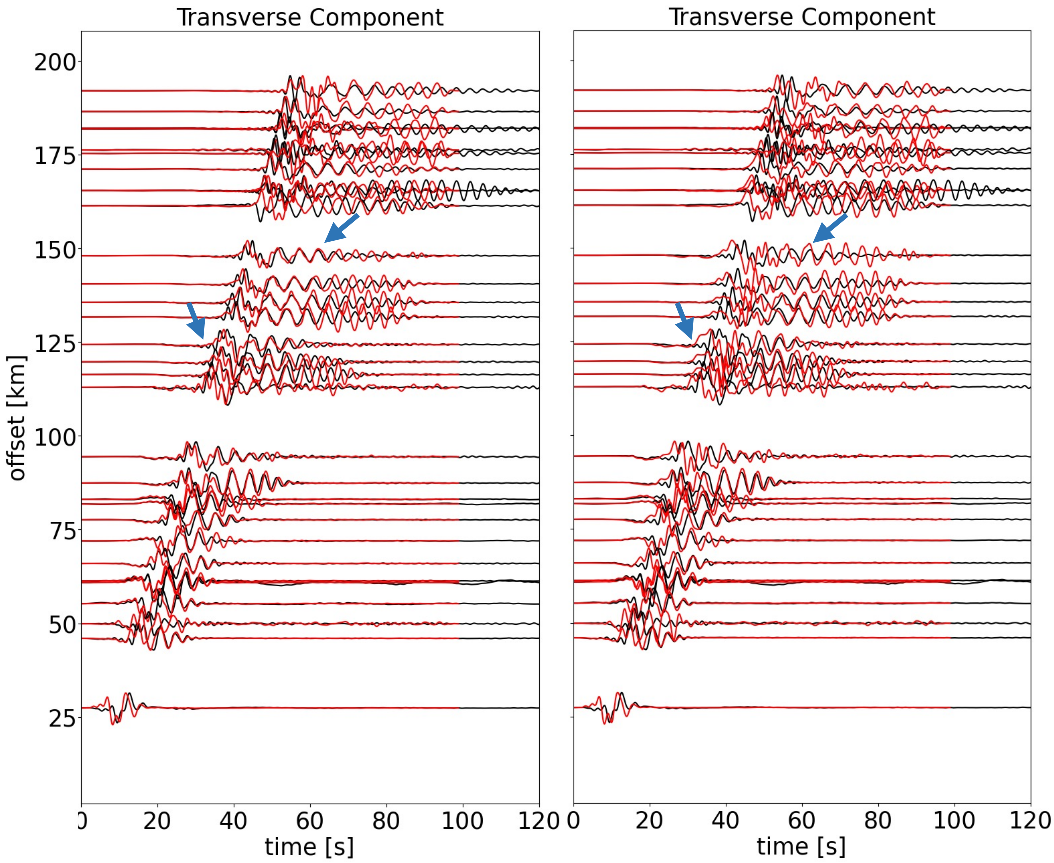

Figure 7. Necessity of incorporating radial anisotropy in the inverted model. Red traces are predicted seismograms based on the inverted model (left) and the modified velocity model after removing positive RA in the uppermost crust (right), while black traces are observations. Only transverse component seismograms are shown here. The locations of earthquake and corresponding stations are the same as Figure 2A. All seismograms are filtered with a 2-30 s passband.

the Anadarko Basin, the weak positive RA (less than +3%) goes down to depths around 20 km (Figures 6K and L).

In contrast to the uppermost crust, a negative RA perturbation (-5%) is imaged within the middle/lower crust beneath the Nemaha-Wilzetta Fault Zone, which is surrounded by relatively weak positive anomalies (+3%) beneath the Anadarko Basin and Cherokee Platform (Figures 5G and H). As the depth increases, the center of this negative anomaly moves northward to the Cherokee Shelf (Figure 5I). The origin of these RA anomalies will be discussed in section 6.2.

To further evaluate the necessity of including radial anisotropy in our inversion, we build another 3-D velocity model by removing the positive RA within the uppermost crust. A Gaussian filter with $\sigma = 0.2\ km$ is applied to remove artificial contrasts due to this modification. All waveforms are filtered with a 2-30 s passband. Compared with the original inverted model (Figure 7A), seismograms from the modified velocity model (Figure 7B) produce much larger mismatches in both travel-times and amplitudes. This comparison demonstrates the necessity of incorporating radial anisotropy in the inversion.

6 Discussion

6.1 Assessments of the Inverted Model

A checkerboard model with a standard deviation $\sigma_{\mathrm{h}} = 30\ km$ in the horizontal direction and $\sigma_{\mathrm{v}} = 10\ km$ in the vertical direction is used to analyze the resolution of our inversion. The amplitude of this checkerboard model is limited within $\pm 15\%$ with respect to the maximum of the inverted model. The action of the Hessian on each model parameter can be approximated by the subtraction of gradients based on perturbed and original 3-D velocity models. In order to evaluate cross-talks among four model parameters, we perturb one model parameter at each time and leave the other three model parameters unchanged.

For instance, Figure 8 illustrates the approximated Hessian action when perturbing β_{v} alone. Regardless of the imperfect shapes resulting from the uneven distribution of seismometers and earthquakes, we are able to successfully recover the positive and negative Gaussian anomalies in the checkerboard model (Figures 8E and e). In addition, the amplitude of the recovered perturbations in β_{v} is ten times larger than the other three model parameters. These results suggest that the inversion is less contaminated by the tradeoff among different model parameters. The other three experiments by perturbing α_{h}, α_{v}, and β_{h} are shown in Section S2 of Supporting Information, which basically give us similar conclusions.

6.2 Origin of Radial Anisotropy

Radial anisotropy can be used as an indicator for investigating tectonic deformation and dynamic processes of the crust (Fouch & Rondenay, 2006; J. Wang & Zhao, 2009; Long, 2013). Major origins of seismic anisotropy include lattice-preferred orientation (LPO)

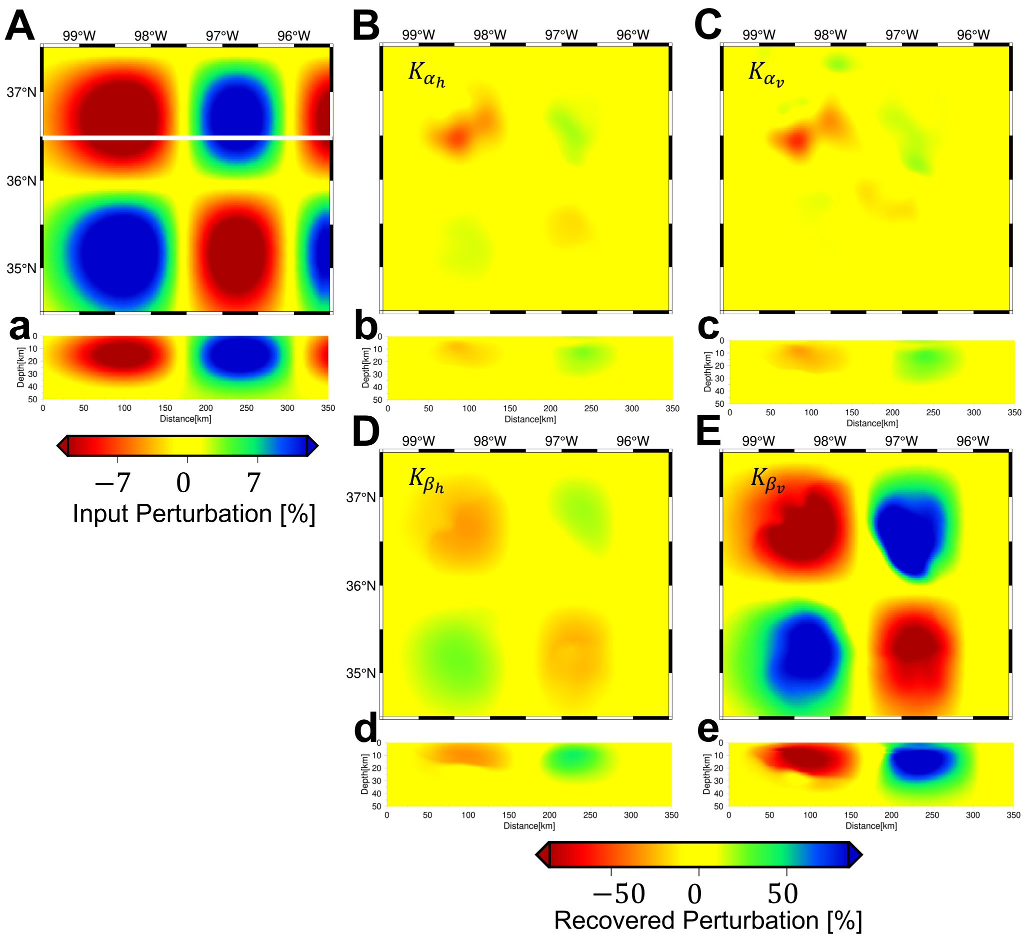

Figure 8. A checkerboard model and corresponding action of the Hessian on velocity perturbation. Panel A shows the distribution of Gaussian anomalies in the checkerboard model. Panels B, C, D and E are the action of the Hessian on 15% perturbations in α_h, α_v, β_h and β_v, respectively. Panels a, b, c, d and e are corresponding vertical sections of Panels A, B, C, D and E along latitude=36.5° N (white line in Panel A).

and shape-preferred orientation (SPO). When discussing the uppermost crust, the alignment of layered structures, pores and cracks could be alternative contributors of radial anisotropy (Babuska & Cara, 1991; Shapiro et al., 2004; Lin et al., 2011).

In our inverted model, we observe positive radial anisotropy near the Earth's surface (Figures 5, and 6), which means that horizontally polarized shear waves V_{sh} are faster than the vertically polarized components V_{sv} (Equation 3). The layered strata of sedimentary deposits might be the major cause of such positive radial anisotropy within the uppermost crust (Crampin, 1989; Johnston & Christensen, 1995; Jiang & Denolle, 2022). The comparatively deep positive anomalies around the Anadarko and Arkoma basins (Figure 6L) might correspond to their thick sedimentary strata, whereas the thin sedimentary deposit in the Cherokee Shelf and Platform can be used to explain their shallow positive anomalies (Figures 6J and L) . In addition, measured by laboratory experiments (Yan et al., 2016), porosity and saturation of sandstone and shale might result in contrastive radial anisotropy in basin and shelf areas as well.

In most cases, radial anisotropy within the middle crust is positive, due to the subhorizontal foliation plane of minerals in response to widespread horizontal-orientated tectonic stress (Shapiro et al., 2004; Guo et al., 2012). However, a large negative volume is observed in the middle crust of the inverted model (Figure 5 and 6). The negative radial anisotropy is often attributed to the injection of magma which forms vertical structures, like dikes (Mordret et al., 2015; Lynner et al., 2018). Nonetheless, few volcanic activities are recorded in the geological history of Oklahoma. In the last decade, negative radial anisotropy has also been reported in Tohoku and Kyushu (J. Wang & Zhao, 2013), the Tehran basin (Shirzad & Shomali, 2014), the eastern Tibet (Huang et al., 2010), and the Los Angeles basin (K. Wang et al., 2020), which potentially result from the preferred orientation of mineral within the middle crust. Therefore, we also interpret the negative volume in the inverted model as the response of anisotropic minerals. With respect to the hexagonal symmetry of mica (Rey, 1993; Shapiro et al., 2004; G. E. Lloyd et al., 2009), or orthorhombic symmetry of amphibole (Brownlee et al., 2017), negative radial anisotropy can be caused by the sub-vertical foliation plane in minerals, which may suggest a potentially vertical tectonic orientation at a local scale. Other than the fast axes in mica/amphibole that are parallel to the direction of deformation, another possible candidate is plagioclase (Christensen, 1996; Almqvist & Mainprice, 2017; Bernard & Behr, 2017), which, in laboratory measurements, exhibits strong anisotropy with fast axes aligning perpendicular to the orientation of shear stresses (Shaocheng & David, 1988; Ji & Salisbury, 1993; Satsukawa et al., 2013). Based on the tectonic history in Oklahoma, the preferred orientation of mica or plagioclase, representing different crystal structures, could be the origin of negative radial anisotropy in the middle crust, but more investigations are needed to distinguish detailed mechanisms.

6.3 Depths of the Crystalline Basement

Figure 9B shows the basement depth in Oklahoma obtained from borehole measurements in the OGS database (`https://www.ou.edu/ogs`). A linear interpolation is applied to smooth these point sampled results. The basement is shallow in the Cherokee Platform and the Southern Oklahoma Aulacogen (less than 0.5 km), and increases in basin areas, such as around 5.0 km in the Arkoma Basin. These borehole measurements are point samples and unevenly distributed, for instance, there are few measurements in the Anadarko and Arkoma Basins, leading to poor constraints on the basement depths in these areas.

Alternatively, we choose the V_s=3.0 km/s contour as a proxy to delineate the lateral variations of the crystalline basement in Oklahoma (Durrheim & Mooney, 1991; Porritt et al., 2020). The resulting map from our inverted 3-D velocity model has similar spatial distribution as well-log measurements, for instance, shallow basement in the Cherokee Platform, the Cherokee Shelf, and the Southern Oklahoma Aulacogen, reflecting thin unconsolidated sedimentary layers. Furthermore, in Figures 9C and D, we show crystalline basement maps extracted from other two 3-D velocity models: US2015 (Schmandt et al., 2015) and US2016 (Shen & Ritzwoller, 2016). Model US2015 is estimated based on multi-mode receiver functions and Rayleigh wave phase velocities (Schmandt et al., 2015), while model US2016 is constrained by the joint inversion of ambient noise Rayleigh wave dispersion curves and P-wave receiver functions (Shen & Ritzwoller, 2016). Their spatial resolution is relatively low when focusing on Oklahoma, since both of them are models for the entire United States. Similar to Figures 9A and B, we can find shallow basements in the Cherokee Platform and the Southern Oklahoma Aulacogen in Figures 9C and D. However, the Anadarko and the Arkoma Basins are not clear in Figures 9C and D, and their depths are overall underestimated, such as around 3 to 4 km in contrast to 12 km from geological surveys and our new model.

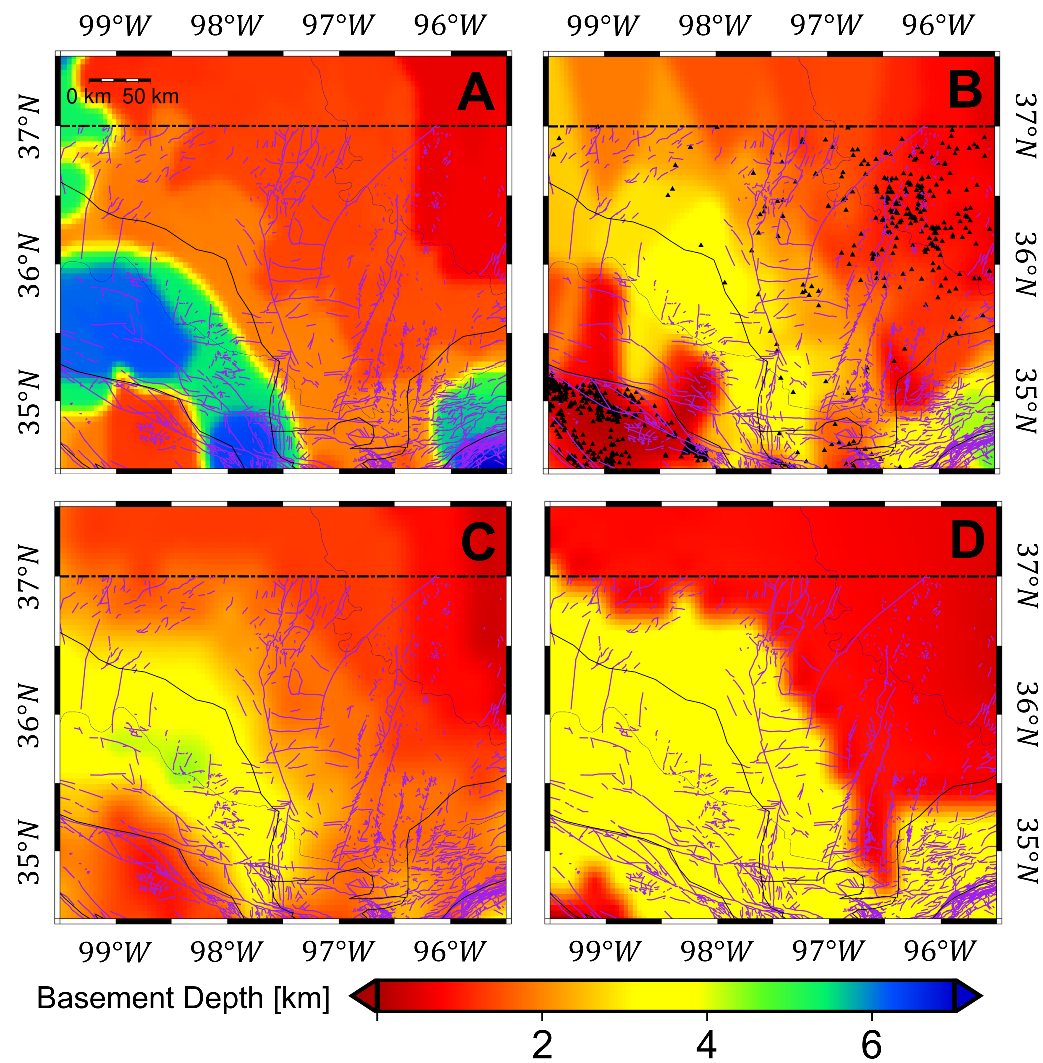

Figure 9. Comparison of crystalline basement depths extracted from our inverted 3D model (Panel A), well log measurements (Panel B), model US2016 from Shen and Ritzwoller (2016) (Panel C) and model US2015 from Schmandt et al. (2015) (Panel D). Black triangles in Panel B represent the locations of well logs (`https://www.ou.edu/ogs`).

6.4 Impact of 3-D velocity models on earthquake locations

To date, many studies have linked the increasing seismicity rate in Oklahoma to industry activities, such as saltwater injection (Keranen et al., 2013, 2014; Langenbruch & Zoback, 2016; X. Chen et al., 2018). Most existing earthquake catalogs are based on 1-D velocity profiles. They have played important roles to study the relation between industry activities and induced seismicity. Previous studies have demonstrated that lateral seismic velocity variations could bias the determination of centroid moment tensor solutions, as well as source locations (Q. Liu et al., 2004; X. Wang & Zhan, 2020). In this section, we illustrate the influence of lateral crustal velocity heterogeneities on earthquake locations in Oklahoma.

In Figure 10, 140 “synthetic earthquakes” are created and they are evenly distributed in the study region, with depths at 5, 10, 15 and 20 km. These “synthetic earthquakes” are relocated by using 58 stations in Oklahoma. Based on the inverted 3-D velocity model, the “observed travel-times” are calculated by using a fast marching method (Sethian, 1996; Sethian & Popovici, 1999), which are then inverted by using NonLinLoc (Lomax et al., 2000) to determine their locations. In the relocation, we use both inverted 3-D velocity model and the associated FWI-1D profile. As shown in Figures 10A and 11B, horizontal biases are overall negligible (less than 2 km) by taking lateral velocity variations or not. Whereas the depth errors are significant (Figures 10B, 10C and 11A). For instance, when using the 1-D velocity profile for earthquake relocation, the vertical errors can go as high as 10 km, which are reduced to around 2.5 km when we use the correct 3-D velocity model. Considering large uncertainties on the depths of relocated earthquakes, it is important to re-investigate the current catalogs by using the inverted 3-D velocity model, which allows us to better determine their depths and further investigate the triggering mechanisms of induced seismicity in Oklahoma.

7 Conclusion

With induced earthquakes and dense seismic stations deployed in Oklahoma, we construct a 3-D radially anisotropic crustal velocity model by using full waveform inversion. Our model can reduce the data misfit by around 40% for all three-component records. This 3-D model enables us to better delineate geological provinces in Oklahoma, such as the Anadarko Basin, the Cherokee Platform, and the Southern Oklahoma Aulacogen.

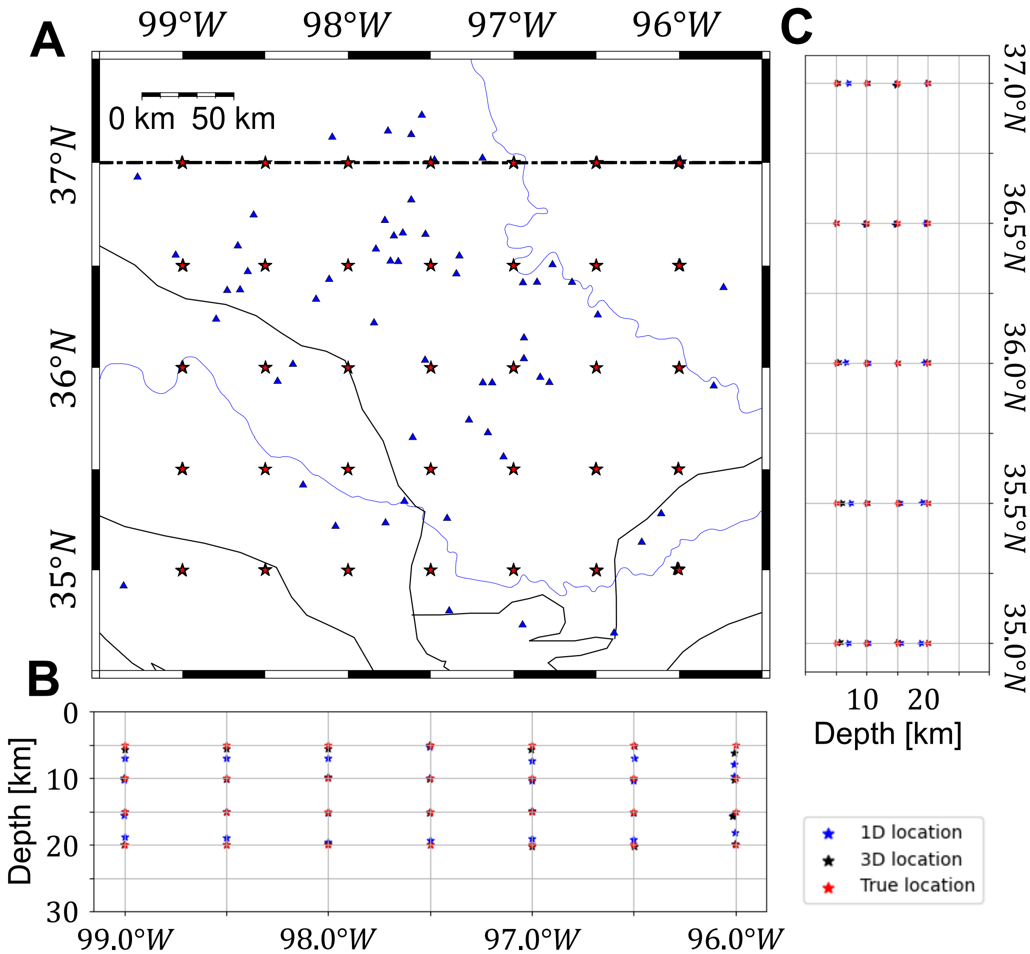

Figure 10. Comparison between earthquake locations based on 1-D (blue stars) and 3-D (black stars) velocity models by using synthetic earthquakes shown as red stars. Blue triangles in panel A denote 58 stations for the relocations. Panels B and C compare results along the vertical sections with latitude=$35.5^{\circ}N$ and longitude=$-98.5^{\circ}N$, respectively.

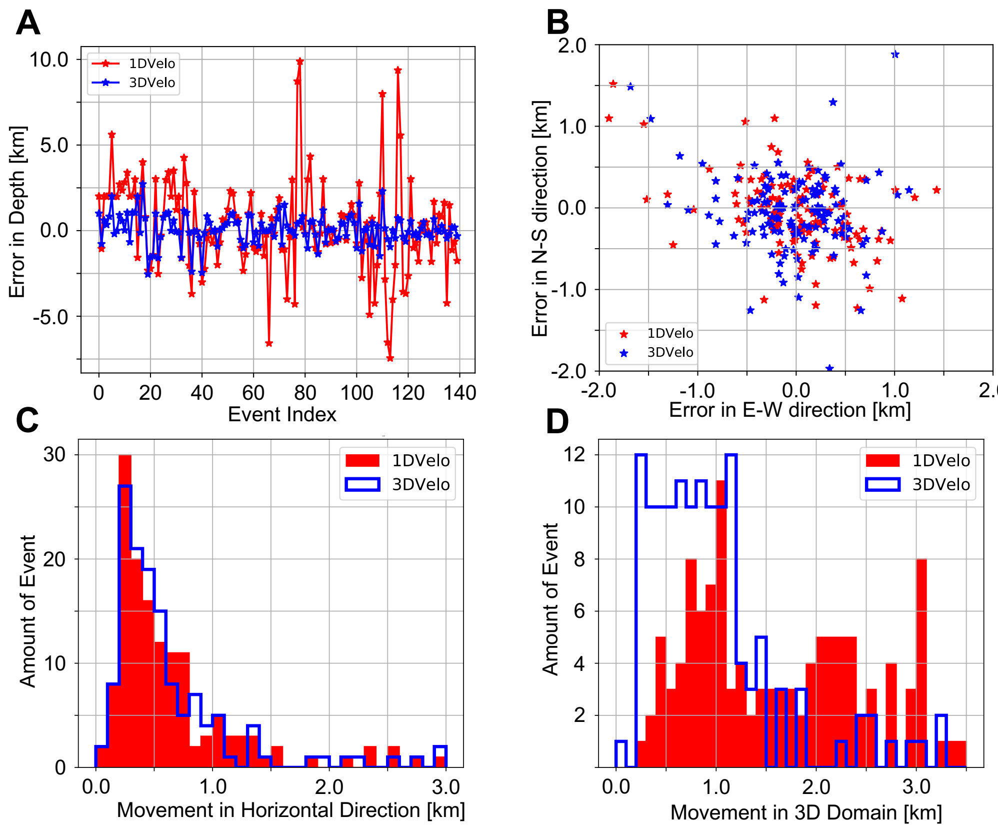

Figure 11. Impact of lateral seismic velocity variations on earthquake locations. Panels A and B illustrate vertical and horizontal errors from relocation based on 1-D (red) and 3-D (blue) velocity models. Panels C and D show the distribution of distances from the true location in the horizontal plane and 3-D volume.

Furthermore, we observe the upper crust is dominated by a thin layer with positive radial anisotropy (+6%), while the middle to lower crust is characterized as relatively large negative radial anisotropy (-6%). These features might be related to deformation from background tectonic stress and preferential alignment of anisotropic minerals. We also extract the depths of the crystalline basement based on the inverted 3-D velocity model, which is overall consistent with borehole measurements. We further demonstrate that the 3-D velocity model allows us to improve the accuracy of earthquake locations, especially for determining their depths. Therefore, the inverted 3-D velocity model provides us an opportunity to better investigate induced earthquakes in Oklahoma.

Acknowledgments

This study is supported by NSF Grant EAR-*** and 3D+4D seismic inversion consortium at the University of Texas at Dallas. We thank the Texas Advanced Computing Center for providing computational facilities for this study. Earthquake source parameters, including time, location, and CMT solutions, are collected from the Earthquake Center of St. Louis University (`https://www.eas.slu.edu/eqc/eqc.html`). Raw seismic waveform records are downloaded from the Data Management Center of Incorporated Research Institutions for Seismology (`https://ds.iris.edu/ds/nodes/dmc/`). Forward and adjoint wavefields are solved by using SPECFEM3D from Computational Infrastructure for Geodynamics (`https://github.com/SPECFEM/specfem3d`). Time window selection is performed by using FLEXWIN (`https://github.com/geodynamics/flexwin`). Well-log information are collected from the Open Data Oklahoma Corporation Commission (`https://www.ou.edu/ogs`). All figures are plotted by Generic Mapping Tools (`https://www.generic-mapping-tools.org/`) and Obspy (`https://docs.obspy.org/`). This is UTD Geoscience contribution number ***.

References

Almqvist, B. S., & Mainprice, D. (2017). Seismic properties and anisotropy of the continental crust: Predictions based on mineral texture and rock microstructure. *Reviews of Geophysics*, *55*(2), 367–433. doi: doi.org/10.1002/2016RG000552

Amante, C., & Eakins, B. W. (2009). *ETOPO1 arc-minute global relief model: procedures, data sources and analysis* (Tech. Rep.). NOAA National Geophysical Data Cente. Retrieved from `https://www.ngdc.noaa.gov/mgg/global/relief/ETOPO1/docs/ETOPO1.pdf`

Anderson, D. L. (1961). Elastic wave propagation in layered anisotropic media. *Journal of Geophysical Research*, *66*(9), 2953–2963. doi: doi.org/10.1029/JZ066i009p02953

Babuska, V., & Cara, M. (1991). *Seismic anisotropy in the Earth* (Vol. 10). Springer Science & Business Media.

Ball, M. M., Henry, M. E., & Frezon, S. E. (1991). *Petroleum geology of the Anadarko Basin region, province (115), Kansas, Oklahoma, and Texas* (Tech. Rep.). doi: doi.org/10.3133/ofr88450W

Barbour, A. J., Norbeck, J. H., & Rubinstein, J. L. (2017). The effects of varying injection rates in Osage County, Oklahoma, on the 2016 m w 5.8 Pawnee earthquake. *Seismological Research Letters*, *88*(4), 1040–1053. doi: doi.org/10.1785/0220170003

Beaty, K. S., Schmitt, D. R., & Sacchi, M. (2002). Simulated annealing inversion of multimode Rayleigh wave dispersion curves for geological structure. *Geophysical Journal International*, *151*(2), 622–631. doi: doi.org/10.1046/j.1365-246X.2002.01809.x

Bernard, R. E., & Behr, W. M. (2017). Fabric heterogeneity in the Mojave lower crust and lithospheric mantle in Southern California. *Journal of Geophysical Research: Solid Earth*, *122*(7), 5000–5025. doi: doi.org/10.1002/2017JB014280

Bozdağ, E., Trampert, J., & Tromp, J. (2011). Misfit functions for full waveform inversion based on instantaneous phase and envelope measurements. *Geophysical Journal International*, *185*(2), 845–870. doi: doi.org/10.1111/j.1365-246X.2011.04970.x

Brownlee, S. J., Schulte-Pelkum, V., Raju, A., Mahan, K., Condit, C., & Orlandini, O. F. (2017). Characteristics of deep crustal seismic anisotropy from a compilation of rock elasticity tensors and their expression in receiver functions. *Tectonics*, *36*(9), 1835–1857. doi: doi.org/10.1002/2017TC004625

Bunks, C., Saleck, F. M., Zaleski, S., & Chavent, G. (1995). Multiscale seismic waveform inversion. *Geophysics*, *60*(5), 1457–1473. doi: https://doi.org/10.1190/1.1443880

Chen, G., Chen, J., Tape, C., Wu, H., & Tong, P. (2023). Double-difference adjoint tomography of the crust and uppermost mantle beneath Alaska. *Journal of Geophysical Research: Solid Earth*, *128*, e2022JB025168. doi: doi.org/10.1029/2022JB025168

Chen, M., Niu, F., Tromp, J., Lenardic, A., Lee, C.-T. A., Cao, W., & Ribeiro, J. (2017). Lithospheric foundering and underthrusting imaged beneath Tibet. *Nature communications*, *8*(1), 1–10. doi: doi.org/10.1038/ncomms15659

Chen, X., Haffener, J., Goebel, T. H., Meng, X., Peng, Z., & Chang, J. C. (2018). Temporal correlation between seismic moment and injection volume for an induced earthquake sequence in central Oklahoma. *Journal of Geophysical Research: Solid Earth*, *123*(4), 3047–3064. doi: doi.org/10.1002/2017JB014694

Chenoweth, P. A. (1968). Early Paleozoic (Arbuckle) overlap, southern mid-continent, United States. *AAPG Bulletin*, *52*(9), 1670–1688. doi: https://doi.org/10.1306/5D25C4C7-16C1-11D7-8645000102C1865D

Chow, B., Kaneko, Y., Tape, C., Modrak, R., & Townend, J. (2020). An automated workflow for adjoint tomography—waveform misfits and synthetic inversions for the North Island, New Zealand. *Geophysical Journal International*, *223*(3), 1461–1480. doi: doi.org/10.1093/gji/ggaa381

Christensen, N. I. (1996). Poisson's ratio and crustal seismology. *Journal of Geophysical Research: Solid Earth*, *101*(B2), 3139–3156. doi: doi.org/10.1029/95JB03446

Cramer, C. H., Bauer, R. A., Chung, J.-w., Rogers, J. D., Pierce, L., Voigt, V., ... others (2017). St. louis area earthquake hazards mapping project: Seismic and liquefaction hazard maps. *Seismological Research Letters*, *88*(1), 206–223.

Crampin, S. (1989). Suggestions for a consistent terminology for seismic anisotropy 1. *Geophysical prospecting*, *37*(7), 753–770. doi: doi.org/10.1111/j.1365-2478.1989.tb02232.x

Dal Moro, G., Pipan, M., & Gabrielli, P. (2007). Rayleigh wave dispersion curve inversion via genetic algorithms and marginal posterior probability density estimation. *Journal of Applied Geophysics*, *61*(1), 39–55. doi: doi.org/10.1016/j.jappgeo.2006.04.002

Darold, A. P., Holland, A. A., Morris, J. K., & Gibson, A. R. (2015). *Oklahoma earthquake summary report 2014* (Tech. Rep.). Okla. Geol. Surv. Open-

File Rept. OF1-2015. Retrieved from `http://ogs.ou.edu/docs/openfile/OF1-2015.pdf`

Debayle, E., & Kennett, B. (2000). Anisotropy in the Australasian upper mantle from Love and Rayleigh waveform inversion. *Earth and Planetary Science Letters*, *184*(1), 339–351. doi: doi.org/10.1016/S0012-821X(00)00314-9

Durrheim, R. J., & Mooney, W. D. (1991). Archean and Proterozoic crustal evolution: Evidence from crustal seismology. *Geology*, *19*(6), 606–609. doi: doi.org/10.1130/0091-7613(1991)019⟨0606:AAPCEE⟩2.3.CO;2

Ellsworth, W. L. (2013). Injection-induced earthquakes. *Science*, *341*(6142). doi: doi.org/10.1126/science.1225942

Evans, J. L. (1979). Major structural and stratigraphic features of the Anadarko basin. , *61*, 2116. doi: doi.org/10.1306/2F9188A1-16CE-11D7-8645000102C1865D

Fichtner, A., Kennett, B. L., Igel, H., & Bunge, H.-P. (2009). Full seismic waveform tomography for upper-mantle structure in the Australasian region using adjoint methods. *Geophysical Journal International*, *179*(3), 1703–1725. doi: doi.org/10.1111/j.1365-246X.2009.04368.x

Fichtner, A., Trampert, J., Cupillard, P., Saygin, E., Taymaz, T., Capdeville, Y., & Villasenor, A. (2013). Multiscale full waveform inversion. *Geophysical Journal International*, *194*(1), 534–556. doi: doi.org/10.1093/gji/ggt118

Fletcher, R., & Reeves, C. M. (1964). Function minimization by conjugate gradients. *The computer journal*, *7*(2), 149–154. doi: doi.org/10.1093/comjnl/7.2.149

Font, Y., Segovia, M., Vaca, S., & Theunissen, T. (2013). Seismicity patterns along the Ecuadorian subduction zone: new constraints from earthquake location in a 3-D a priori velocity model. *Geophysical Journal International*, *193*(1), 263–286. doi: doi.org/10.1093/gji/ggs083

Fouch, M. J., & Rondenay, S. (2006). Seismic anisotropy beneath stable continental interiors. *Physics of the Earth and Planetary Interiors*, *158*(2-4), 292–320. doi: doi.org/10.1016/j.pepi.2006.03.024

French, S., & Romanowicz, B. A. (2014). Whole-mantle radially anisotropic shear velocity structure from spectral-element waveform tomography. *Geophysical Journal International*, *199*(3), 1303–1327. doi: doi.org/10.1093/gji/ggu334

Guo, Z., Gao, X., Wang, W., & Yao, Z. (2012). Upper-and mid-crustal radial anisotropy beneath the central Himalaya and southern Tibet from seismic ambient noise tomography. *Geophysical Journal International*, *189*(2), 1169–1182. doi: doi.org/10.1111/j.1365-246X.2012.05425.x

Hamilton, W. B. (1956). Precambrian rocks of Wichita and Arbuckle mountains, Oklahoma. *Geological Society of America Bulletin*, *67*(10), 1319–1330. doi: doi.org/10.1130/0016-7606(1956)67[1319:PROWAA]2.0.CO;2

Harkrider, D. G. (1964). Surface waves in multilayered elastic media i. Rayleigh and Love waves from buried sources in a multilayered elastic half-space. *Bulletin of the Seismological Society of America*, *54*(2), 627–679. doi: doi.org/10.1785/BSSA0540020627

Herrmann, R. B. (2013). Computer programs in seismology: An evolving tool for instruction and research. *Seismological Research Letters*, *84*(6), 1081–1088. doi: doi.org/10.1785/0220110096

Higley, D. K., Cook, T. A., & Pawlewicz, M. J. (2014). Petroleum systems and assessment of undiscovered oil and gas in the Anadarko Basin Province, Colorado, Kansas, Oklahoma, and Texas—Woodford Shale assessment units. , *58*. doi: doi.org/10.3133/ds69EE

Holland, A. A. (2013a). Earthquakes triggered by hydraulic fracturing in south-central Oklahoma. *Bulletin of the Seismological Society of America*, *103*(3), 1784–1792. doi: doi.org/10.1785/0120120109

Holland, A. A. (2013b). Optimal fault orientations within oklahoma. *Seismological Research Letters*, *84*(5), 876–890. doi: doi.org/10.1785/0220120153

Houtz, R. E., & Ludwig, W. J. (1979). Distribution of reverberant subbottom layers in the southwest Pacific basin. *Journal of Geophysical Research: Solid Earth*, *84*(B7), 3497–3504. doi: doi.org/10.1029/JB084iB07p03497

Huang, H., Yao, H., & van der Hilst, R. D. (2010). Radial anisotropy in the crust of SE Tibet and SW China from ambient noise interferometry. *Geophysical Research Letters*, *37*(21). doi: doi.org/10.1029/2010GL044981

Ji, S., & Salisbury, M. H. (1993). Shear-wave velocities, anisotropy and splitting in high-grade mylonites. *Tectonophysics*, *221*(3-4), 453–473. doi: doi.org/10.1016/0040-1951(93)90173-H

Jiang, C., & Denolle, M. A. (2022). Pronounced Seismic Anisotropy in Kanto Sedimentary Basin: A Case Study of Using Dense Arrays, Ambient Noise Seismology, and Multi-Modal Surface-Wave Imaging. *Journal of Geophysical Research: Solid Earth*, *127*(8), e2022JB024613. doi: doi.org/10.1029/2022JB024613

Johnson, K. S. (1996). *Geology of Oklahoma* (Tech. Rep.). Oklahoma Geological Survey. Retrieved from `http://ogs.ou.edu/docs/specialpublications/SP96-5.pdf`

Johnson, K. S., & Luza, K. V. (2008). *Earth sciences and mineral resources of Oklahoma* (Tech. Rep.). Oklahoma Geological Survey. Retrieved from `http://www.ogs.ou.edu/pubsscanned/EP9_All.pdf`

Johnston, J. E., & Christensen, N. I. (1995). Seismic anisotropy of shales. *Journal of Geophysical Research: Solid Earth*, *100*(B4), 5991–6003. doi: doi.org/10.1029/95JB00031

Keller, G. R. (2013). The Moho of North America: A brief review focused on recent studies. *Tectonophysics*, *609*, 45–55. doi: doi.org/10.1016/j.tecto.2013.07.031

Keranen, K. M., Savage, H. M., Abers, G. A., & Cochran, E. S. (2013). Potentially induced earthquakes in Oklahoma, USA: Links between wastewater injection and the 2011 Mw 5.7 earthquake sequence. *Geology*, *41*(6), 699–702. doi: doi.org/10.1130/G34045.1

Keranen, K. M., Weingarten, M., Abers, G. A., Bekins, B. A., & Ge, S. (2014). Sharp increase in central Oklahoma seismicity since 2008 induced by massive wastewater injection. *Science*, *345*(6195), 448–451. doi: doi.org/10.1126/science.1255802

Kolawole, F., Turko, M. S., & Carpenter, B. M. (2020). Basement-controlled deformation of sedimentary sequences, Anadarko Shelf, Oklahoma. *Basin Research*, *32*(6), 1365–1387. doi: https://doi.org/10.1111/bre.12433

Komatitsch, D., & Tromp, J. (1999). Introduction to the spectral element method for three-dimensional seismic wave propagation. *Geophysical journal international*, *139*(3), 806–822. doi: doi.org/10.1046/j.1365-246x.1999.00967.x

Lailly, P., & Bednar, J. (1983). The seismic inverse problem as a sequence of before stack migrations. In *Conference on inverse scattering: theory and application* (pp. 206–220).

Langenbruch, C., & Zoback, M. D. (2016). How will induced seismicity in Oklahoma respond to decreased saltwater injection rates? *Science advances*, *2*(11), e1601542. doi: https://doi.org/10.1126/sciadv.1601542

Lei, W., Ruan, Y., Bozdağ, E., Peter, D., Lefebvre, M., Komatitsch, D., ... Pugmire, D. (2020). Global adjoint tomography—model GLAD-M25. *Geophysical Journal International*, *223*(1), 1–21. doi: https://doi.org/10.1093/gji/ggaa253

Lin, F.-C., Ritzwoller, M. H., Yang, Y., Moschetti, M. P., & Fouch, M. J. (2011). Complex and variable crustal and uppermost mantle seismic anisotropy in the western United States. *Nature Geoscience*, *4*(1), 55–61. doi: https://doi.org/10.1038/ngeo1036

Liu, Q., Polet, J., Komatitsch, D., & Tromp, J. (2004). Spectral-element moment tensor inversions for earthquakes in southern California. *Bulletin of the Seismological Society of America*, *94*(5), 1748–1761. doi: https://doi.org/10.1785/012004038

Liu, Y., Teng, J., Xu, T., Wang, Y., Liu, Q., & Badal, J. (2017). Robust time-domain full waveform inversion with normalized zero-lag cross-correlation objective function. *Geophysical Journal International*, *209*(1), 106–122. doi: https://doi.org/10.1093/gji/ggw485

Lloyd, A., Wiens, D., Zhu, H., Tromp, J., Nyblade, A., Aster, R., ... others (2020). Seismic structure of the Antarctic upper mantle imaged with adjoint tomography. *Journal of Geophysical Research: Solid Earth*, *125*(3). doi: https://doi.org/10.1029/2019JB017823

Lloyd, G. E., Butler, R. W., Casey, M., & Mainprice, D. (2009). Mica, deformation fabrics and the seismic properties of the continental crust. *Earth and Planetary Science Letters*, *288*(1-2), 320–328. doi: https://doi.org/10.1016/j.epsl.2009.09.035

Lomax, A., Virieux, J., Volant, P., & Berge-Thierry, C. (2000). Probabilistic earthquake location in 3D and layered models. In *Advances in seismic event location* (pp. 101–134). Springer. doi: 10.1007/978-94-015-9536-0_5

Long, M. D. (2013). Constraints on subduction geodynamics from seismic anisotropy. *Reviews of Geophysics*, *51*(1), 76–112. doi: https://doi.org/10.1002/rog.20008

Lund Snee, J.-E., & Zoback, M. D. (2020). Multiscale variations of the crustal stress field throughout North America. *Nature Communications*, *11*(1), 1951. doi: https://doi.org/10.1038/s41467-020-15841-5

Luo, Y. (2012). *Seismic imaging and inversion based on spectral-element and adjoint methods* (Doctoral dissertation, Princeton University). Retrieved from https://dataspace.princeton.edu/handle/88435/dsp018623hx78j

Luo, Y., Modrak, R., & Tromp, J. (2015). Strategies in adjoint tomography. In *Handbook of Geomathematics: Second Edition* (pp. 1943–2001). Springer Berlin Heidelberg. doi: 10.1007/978-3-642-54551-1_96

Luo, Y., & Schuster, G. T. (1991). Wave-equation traveltime inversion. *Geophysics*, *56*(5), 645–653. doi: https://doi.org/10.1190/1.1443081

Lynner, C., Beck, S. L., Zandt, G., Porritt, R. W., Lin, F.-C., & Eilon, Z. C. (2018). Midcrustal deformation in the Central Andes constrained by radial anisotropy. *Journal of Geophysical Research: Solid Earth*, *123*(6), 4798–4813. doi: https://doi.org/10.1029/2017JB014936

Ma, Y., & Hale, D. (2013). Wave-equation reflection traveltime inversion with dynamic warping and full-waveform inversion. *Geophysics*, *78*(6), R223–R233. doi: https://doi.org/10.1190/geo2013-0004.1

Maggi, A., Tape, C., Chen, M., Chao, D., & Tromp, J. (2009). An automated time-window selection algorithm for seismic tomography. *Geophysical Journal International*, *178*(1), 257–281. doi: https://doi.org/10.1111/j.1365-246X.2009.04099.x

Marsh, S., & Holland, A. (2016). *Comprehensive fault database and interpretive fault map of Oklahoma* (Tech. Rep.). Oklahoma Geological Survey. Retrieved from http://ogs.ou.edu/docs/openfile/OF2-2016.pdf

Matthies, H., & Strang, G. (1979). The solution of nonlinear finite element equations. *International journal for numerical methods in engineering*, *14*(11), 1613–1626. doi: https://doi.org/10.1002/nme.1620141104

McNamara, D. E., Benz, H. M., Herrmann, R. B., Bergman, E. A., Earle, P., Holland, A., . . . Gassner, A. (2015). Earthquake hypocenters and focal mechanisms in central Oklahoma reveal a complex system of reactivated subsurface strike-slip faulting. *Geophysical Research Letters*, *42*(8), 2742–2749. doi: https://doi.org/10.1002/2014GL062730

Métivier, L., Brossier, R., Mérigot, Q., Oudet, E., & Virieux, J. (2016). Measuring the misfit between seismograms using an optimal transport distance: Application to full waveform inversion. *Geophysical Supplements to the*

Monthly Notices of the Royal Astronomical Society, *205*(1), 345–377. doi: doi.org/10.1093/gji/ggw014

Michelini, A., & Lomax, A. (2004). The effect of velocity structure errors on double-difference earthquake location. *Geophysical Research Letters*, *31*(9). doi: https://doi.org/10.1093/gji/ggw014

Mitchell, B., & Landisman, M. (1970). Interpretation of a crustal section across Oklahoma. *Geological Society of America Bulletin*, *81*(9), 2647–2656. doi: https://doi.org/10.1130/0016-7606(1970)81[2647:IOACSA]2.0.CO;2

Mordret, A., Rivet, D., Landès, M., & Shapiro, N. M. (2015). Three-dimensional shear velocity anisotropic model of Piton de la Fournaise Volcano (La Réunion Island) from ambient seismic noise. *Journal of Geophysical Research: Solid Earth*, *120*(1), 406–427. doi: https://doi.org/10.1002/2014JB011654

Mueller, C. S. (2019). Earthquake catalogs for the USGS national seismic hazard maps. *Seismological Research Letters*, *90*(1), 251–261. doi: https://doi.org/10.1785/0220170108

Northcutt, R. A., & Campbell, J. A. (1996). Geologic provinces of Oklahoma. *The Shale Shaker*, *46*(5), 99–103. doi: 10.1007/978-94-011-5098-9_2

Pennington, C., & Chen, X. (2017). Coulomb stress interactions during the M w 5.8 Pawnee sequence. *Seismological Research Letters*, *88*(4), 1024–1031. doi: https://doi.org/10.1785/0220170011

Perry, W. J. (1989). *Tectonic evolution of the Anadarko Basin region, Oklahoma* (No. 1866). Department of the Interior, US Geological Survey. doi: https://doi.org/10.3133/b1866A

Peter, D., Komatitsch, D., Luo, Y., Martin, R., Le Goff, N., Casarotti, E., . . . others (2011). Forward and adjoint simulations of seismic wave propagation on fully unstructured hexahedral meshes. *Geophysical Journal International*, *186*(2), 721–739. doi: doi.org/10.1111/j.1365-246X.2011.05044.x

Porritt, R., Savvaidis, A., Young, B., Shirley, M., & Li, P. (2020). Crustal Structure in Southeastern Texas From Joint Inversion of Ambient Seismic Noise and P to S Receiver Functions. *Geochemistry, Geophysics, Geosystems*, *21*(7), e2019GC008866. doi: https://doi.org/10.1029/2019GC008866

Rey, P. (1993). Seismic and tectono-metamorphic characters of the lower continental crust in Phanerozoic areas: A consequence of post-thickening extension. *Tec-*

tonics, *12*(2), 580–590. doi: https://doi.org/10.1029/92TC01568

Rickers, F., Fichtner, A., & Trampert, J. (2013). The Iceland–Jan Mayen plume system and its impact on mantle dynamics in the North Atlantic region: evidence from full-waveform inversion. *Earth and Planetary Science Letters*, *367*, 39–51. doi: https://doi.org/10.1016/j.epsl.2013.02.022

Rubinstein, J. L., & Mahani, A. B. (2015). Myths and facts on wastewater injection, hydraulic fracturing, enhanced oil recovery, and induced seismicity. *Seismological Research Letters*, *86*(4), 1060–1067. doi: https://doi.org/10.1785/0220150067

Sams, M., Neep, J., Worthington, M., & King, M. (1997). The measurement of velocity dispersion and frequency-dependent intrinsic attenuation in sedimentary rocks. *Geophysics*, *62*(5), 1456–1464. doi: https://doi.org/10.1190/1.1444249

Satsukawa, T., Ildefonse, B., Mainprice, D., Morales, L., Michibayashi, K., & Barou, F. (2013). A database of plagioclase crystal preferred orientations (CPO) and microstructures–implications for CPO origin, strength, symmetry and seismic anisotropy in gabbroic rocks. *Solid Earth*, *4*(2), 511–542. doi: https://doi.org/10.5194/se-4-511-2013

Schmandt, B., Lin, F.-C., & Karlstrom, K. E. (2015). Distinct crustal isostasy trends east and west of the Rocky Mountain Front. *Geophysical Research Letters*, *42*(23), 10–290. doi: https://doi.org/10.1002/2015GL066593

Schoenball, M., & Ellsworth, W. L. (2017). Waveform-relocated earthquake catalog for Oklahoma and southern Kansas illuminates the regional fault network. *Seismological Research Letters*, *88*(5), 1252–1258. doi: https://doi.org/10.1785/0220170083

Sethian, J. A. (1996). A fast marching level set method for monotonically advancing fronts. *Proceedings of the National Academy of Sciences*, *93*(4), 1591–1595. doi: https://doi.org/10.1073/pnas.93.4.1591

Sethian, J. A., & Popovici, A. M. (1999). 3-D traveltime computation using the fast marching method. *Geophysics*, *64*(2), 516–523. doi: https://doi.org/10.1190/1.1444558

Shaocheng, J., & David, M. (1988). Natural deformation fabrics of plagioclase: implications for slip systems and seismic anisotropy. *Tectonophysics*, *147*(1-2), 145–163. doi: https://doi.org/10.1016/0040-1951(88)90153-9

Shapiro, N. M., Ritzwoller, M. H., Molnar, P., & Levin, V. (2004). Thinning and flow of Tibetan crust constrained by seismic anisotropy. *Science*, *305*(5681), 233–236. doi: https://doi.org/10.1126/science.1098276

Shen, W., & Ritzwoller, M. H. (2016). Crustal and uppermost mantle structure beneath the United States. *Journal of Geophysical Research: Solid Earth*, *121*(6), 4306–4342. doi: https://doi.org/10.1002/2016JB012887

Shirzad, T., & Shomali, Z. H. (2014). Shallow crustal radial anisotropy beneath the Tehran basin of Iran from seismic ambient noise tomography. *Physics of the Earth and Planetary Interiors*, *231*, 16–29. doi: https://doi.org/10.1016/j.pepi.2014.04.001

Skoumal, R. J., Ries, R., Brudzinski, M. R., Barbour, A. J., & Currie, B. S. (2018). Earthquakes induced by hydraulic fracturing are pervasive in Oklahoma. *Journal of Geophysical Research: Solid Earth*, *123*(12), 10–918. doi: doi.org/10.1029/2018JB016790

Sloss, L. L. (1988). *Sedimentary Cover—North American Craton: US.* Geological Society of America.

Sumy, D. F., Cochran, E. S., Keranen, K. M., Wei, M., & Abers, G. A. (2014). Observations of static Coulomb stress triggering of the November 2011 M5. 7 Oklahoma earthquake sequence. *Journal of Geophysical Research: Solid Earth*, *119*(3), 1904–1923. doi: https://doi.org/10.1002/2013JB010612

Takemura, S., Yoshimoto, K., & Shiomi, K. (2021). Long-period ground motion simulation using centroid moment tensor inversion solutions based on the regional three-dimensional model in the Kanto region, Japan. *Earth, Planets and Space*, *73*(1), 1–18. doi: https://doi.org/10.1186/s40623-020-01348-2

Tan, J., Langston, C. A., & Ni, S. (2021). Shallow shear-wave velocity structure in Oklahoma based on the joint inversion of ambient noise dispersion and teleseismic P-wave receiver functions. *Bulletin of the Seismological Society of America*, *111*(2), 654–670. doi: https://doi.org/10.1785/0120200246

Tao, K., Grand, S. P., & Niu, F. (2017). Full-waveform inversion of triplicated data using a normalized-correlation-coefficient-based misfit function. *Geophysical Journal International*, *210*(3), 1517–1524. doi: https://doi.org/10.1093/gji/ggx249

Tao, K., Grand, S. P., & Niu, F. (2018). Seismic structure of the upper mantle beneath eastern Asia from full waveform seismic tomography. *Geochemistry, Geophysics, Geosystems*, *19*(8), 2732–2763. doi: https://doi.org/10.1029/2018GC007460

Tape, C., Liu, Q., Maggi, A., & Tromp, J. (2010). Seismic tomography of the southern California crust based on spectral-element and adjoint methods. *Geophysical Journal International*, *180*(1), 433–462. doi: https://doi.org/10.1111/j.1365-246X.2009.04429.x

Tape, C., Liu, Q., & Tromp, J. (2007). Finite-frequency tomography using adjoint methods—Methodology and examples using membrane surface waves. *Geophysical Journal International*, *168*(3), 1105–1129. doi: https://doi.org/10.1111/j.1365-246X.2006.03191.x

Tarantola, A. (1984). Inversion of seismic reflection data in the acoustic approximation. *Geophysics*, *49*(8), 1259–1266. doi: https://doi.org/10.1190/1.1441754

Thurber, C. H. (1983). Earthquake locations and three-dimensional crustal structure in the Coyote Lake area, central California. *Journal of Geophysical Research: Solid Earth*, *88*(B10), 8226–8236. doi: https://doi.org/10.1029/JB088iB10p08226

Tromp, J., Tape, C., & Liu, Q. (2005). Seismic tomography, adjoint methods, time reversal and banana-doughnut kernels. *Geophysical Journal International*, *160*(1), 195–216. doi: https://doi.org/10.1111/j.1365-246X.2004.02453.x

Virieux, J., & Operto, S. (2009). An overview of full-waveform inversion in exploration geophysics. *Geophysics*, *74*(6), WCC1–WCC26. doi: https://doi.org/10.1190/1.3238367

Walsh, F. R., & Zoback, M. D. (2015). Oklahoma's recent earthquakes and saltwater disposal. *Science advances*, *1*(5), e1500195. doi: https://doi.org/10.1126/sciadv.1500195

Walter, J. I., Ogwari, P., Thiel, A., Ferrer, F., Woelfel, I., Chang, J. C., … Holland, A. A. (2020). The Oklahoma Geological Survey Statewide Seismic Network. *Seismological Research Letters*, *91*(2A), 611–621. doi: https://doi.org/10.1785/0220190211

Wang, J., & Zhao, D. (2009). P-wave anisotropic tomography of the crust and upper mantle under Hokkaido, Japan. *Tectonophysics*, *469*(1-4), 137–149. doi: https://doi.org/10.1016/j.tecto.2009.02.005

Wang, J., & Zhao, D. (2013). P-wave tomography for 3-D radial and azimuthal anisotropy of Tohoku and Kyushu subduction zones. *Geophysical Journal International*, *193*(3), 1166–1181. doi: https://doi.org/10.1093/gji/ggt086

Wang, K., Jiang, C., Yang, Y., Schulte-Pelkum, V., & Liu, Q. (2020). Crustal deformation in Southern California constrained by radial anisotropy from ambient noise adjoint tomography. *Geophysical Research Letters*, *47*(12), e2020GL088580. doi: https://doi.org/10.1029/2020GL088580

Wang, X., & Zhan, Z. (2020). Moving from 1-D to 3-D velocity model: automated waveform-based earthquake moment tensor inversion in the Los Angeles region. *Geophysical Journal International*, *220*(1), 218–234. doi: https://doi.org/10.1093/gji/ggz435

Warner, M., & Guasch, L. (2016). Adaptive waveform inversion: Theory. *Geophysics*, *81*(6), R429–R445. doi: https://doi.org/10.1190/geo2015-0387.1

Whitaker, A. E., & Engelder, T. (2006). Plate-scale stress fields driving the tectonic evolution of the central Ouachita salient, Oklahoma and Arkansas. *Geological Society of America Bulletin*, *118*(5-6), 710–723. doi: https://doi.org/10.1130/B25780.1

Wu, R.-S., Luo, J., & Wu, B. (2014). Seismic envelope inversion and modulation signal model. *Geophysics*, *79*(3), WA13–WA24. doi: https://doi.org/10.1190/geo2013-0294.1

Xu, C., Cronin, T. P., McGinness, T. E., & Steer, B. (2009). Middle Atokan sediment gravity flows in the Red Oak field, Arkoma Basin, Oklahoma: A sedimentary analysis using electrical borehole images and wireline logs. *AAPG bulletin*, *93*(1), 1–29. doi: https://doi.org/10.1306/09030808054

Yan, F., Han, D.-H., Sil, S., & Chen, X.-L. (2016). Analysis of seismic anisotropy parameters for sedimentary strata. *Geophysics*, *81*(5), D495–D502. doi: https://doi.org/10.1190/geo2016-0062.1

Yang, Y., & Engquist, B. (2018). Analysis of optimal transport and related misfit functions in full-waveform inversion. *Geophysics*, *83*(1), A7–A12. doi: https://doi.org/10.1190/geo2017-0264.1

Yu, Y., Song, J., Liu, K. H., & Gao, S. S. (2015). Determining crustal structure beneath seismic stations overlying a low-velocity sedimentary layer using receiver functions. *Journal of Geophysical Research: Solid Earth*, *120*(5), 3208–3218.

doi: https://doi.org/10.1002/2014JB011610

Zhang, C., Yao, H., Liu, Q., Zhang, P., Yuan, Y. O., Feng, J., & Fang, L. (2018). Linear array ambient noise adjoint tomography reveals intense crust-mantle interactions in North China Craton. *Journal of Geophysical Research: Solid Earth*, *123*(1), 368–383. doi: https://doi.org/10.1002/2017JB015019

Zhu, H. (2018). Crustal wave speed structure of North Texas and Oklahoma based on ambient noise cross-correlation functions and adjoint tomography. *Geophysical Journal International*, *214*(1), 716–730. doi: https://doi.org/10.1093/gji/ggy169

Zhu, H., Bozdağ, E., & Tromp, J. (2015). Seismic structure of the European upper mantle based on adjoint tomography. *Geophysical Journal International*, *201*(1), 18–52. doi: https://doi.org/10.1093/gji/ggu492

Zhu, H., & Fomel, S. (2016). Building good starting models for full-waveform inversion using adaptive matching filtering misfit. *Geophysics*, *81*(5), U61–U72. doi: https://doi.org/10.1190/geo2015-0596.1

Zhu, H., Komatitsch, D., & Tromp, J. (2017). Radial anisotropy of the North American upper mantle based on adjoint tomography with USArray. *Geophysical Journal International*, *211*(1), 349–377. doi: https://doi.org/10.1093/gji/ggx305

Supporting Information for "Constructing a 3-D radially anisotropic crustal velocity model for Oklahoma using full waveform inversion"

Shuo Zhang[1] and Hejun Zhu[1,2]

[1]Department of Geosciences, the University of Texas at Dallas

[2]Department of Physics, the University of Texas at Dallas

Contents of this file

Introduction

In this supporting document, we provide additional details on data processing and analysis to support discussions in the main text. Section S1 provides waveform comparisons based on different velocity models. Section S2 provides checkerboard test results with respect to α_h, α_v, and β_h.

Text S1. Comparison between observed and predicted seismic recordings based on different velocity models

We show predicted seismograms based on the initial model to illustrate the improvement of data fitting by the inversion (Figure S1). Using the same earthquake and seismic arrays as shown in Figure 2 of the main text, we observe the reduction of time shifts between observed and predicted recordings.

As a comparison, we also simulate seismic recordings based on the 1-D OGS velocity profile (Figure S2), with the same earthquake and station arrays in Figure S1. Compared with Figrue 2 in the main text, larger mismatches in waveform fitting in Figure S2, especially for large epicentral distances, indicate the performance of the inverted 3-D velocity model.

Text S2. Checkerboard tests

A checkerboard model is designed with positive and negative Gaussian-shape anomalies (Figure S3), with the standard deviation $\sigma_{\mathrm{h}} = 30km$ and $\sigma_{\mathrm{v}} = 10km$. The magnitude of the checkerboard model is set to be 14% of the maximal value of the corresponding model parameters. Considering the interreaction among different model parameters, four individual tests are performed for α_{h}, α_{v}, β_{h} and β_{v}, respectively. To recover the checkerboard pattern, two synthetic seismograms are generated by the original and perturbed models, which are then used to compute misfit gradients. The subtraction of these two gradients is used to approximate the pattern of the Hessian on specific model parameters. Other than Figure 8 with respect to β_{v} in the main text, Figures S4, S5 and S6 show the recovered checkerboard patterns for α_{h}, α_{v}, and β_{h}. Similar to Figure 8 in the main text, the recovered perturbations involve the positive/negative anomalies in the horizontal direction, with imperfect Gaussian shapes which are determined by the ray sampling. Vertically, the current acquisition system can detect velocity anomalies at depths shallower than 40 km. Except for the resolution assessment, the checkerboard test can also be used to evaluate trade-offs among different model parameters. In these four experiments, the contamination among model parameters is limited, although we can still observe leakages among model parameters. The magnitude of the perturbation in unperturbed model parameters is ten times smaller than that in the perturbed parameter. These checkerboard tests validate model parameterization and model resolution in this study.

References

Johnson, K. S. (1973). Oklahoma geological survey. *Annual Review, Indiana," in Mining*.

Marsh, S., & Holland, A. (2016). Comprehensive fault database and interpretive fault map of oklahoma. *Oklahoma Geol. Surv. Open-File Rep. OF2-2016, Oklahoma Geological Survey, Norman, OK*.

Zhu, H. (2018). Crustal wave speed structure of north texas and oklahoma based on ambient noise cross-correlation functions and adjoint tomography. *Geophysical Journal International*, *214* (1), 716–730.

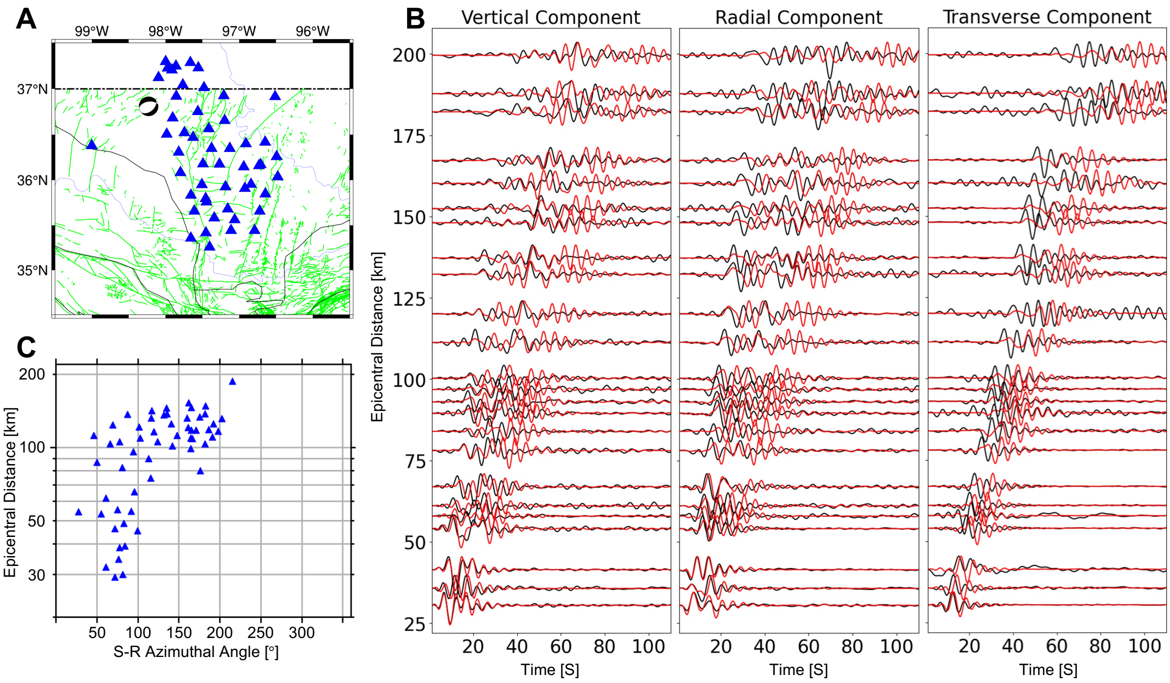

Figure S1. Performance of the initial velocity model in data domain. The locations of the particular earthquake and corresponding stations are shown in panel A, with the distribution of azimuthal and epicentral distance shown in panel C. Panel B shows the comparison between observed (black) and predicted (red) seismograms based on the initial velocity model (Zhu, 2018) within a 5-30 s passband. Green lines in panel A are fault traces measured at the Earth's surface (Marsh & Holland, 2016), and the thin black lines denote the boundaries of geological provinces in Oklahoma (Johnson, 1973)

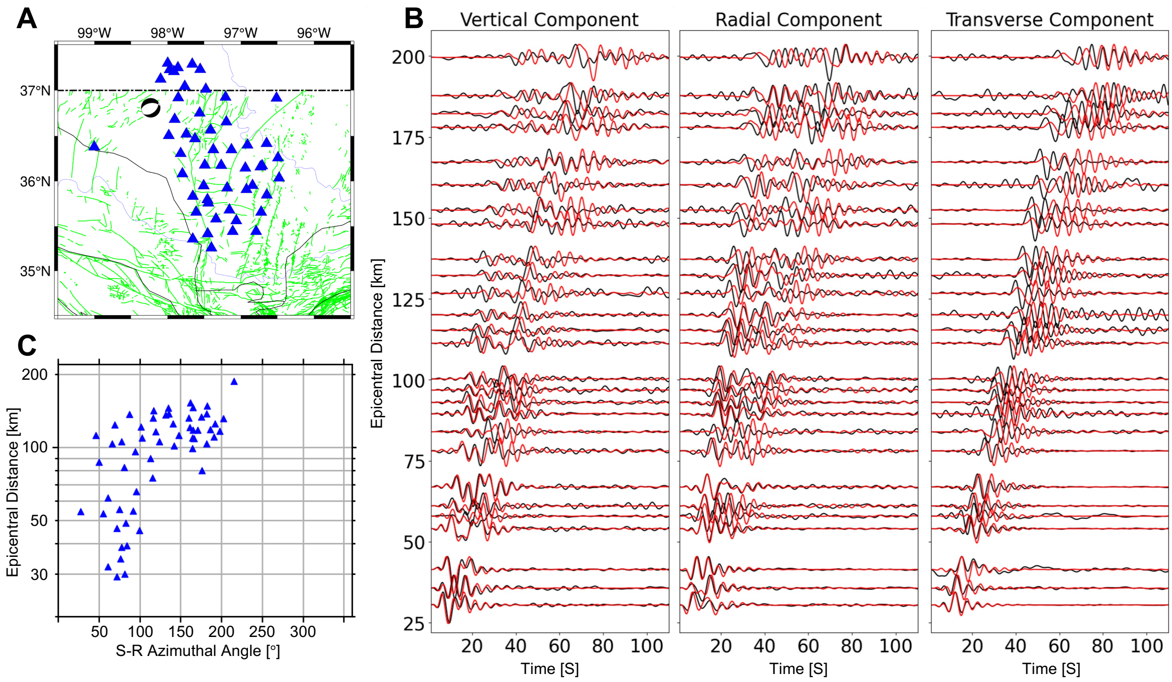

Figure S2. The same settings as Figure S1 but from simulations based on OGS-1D velocity profile.

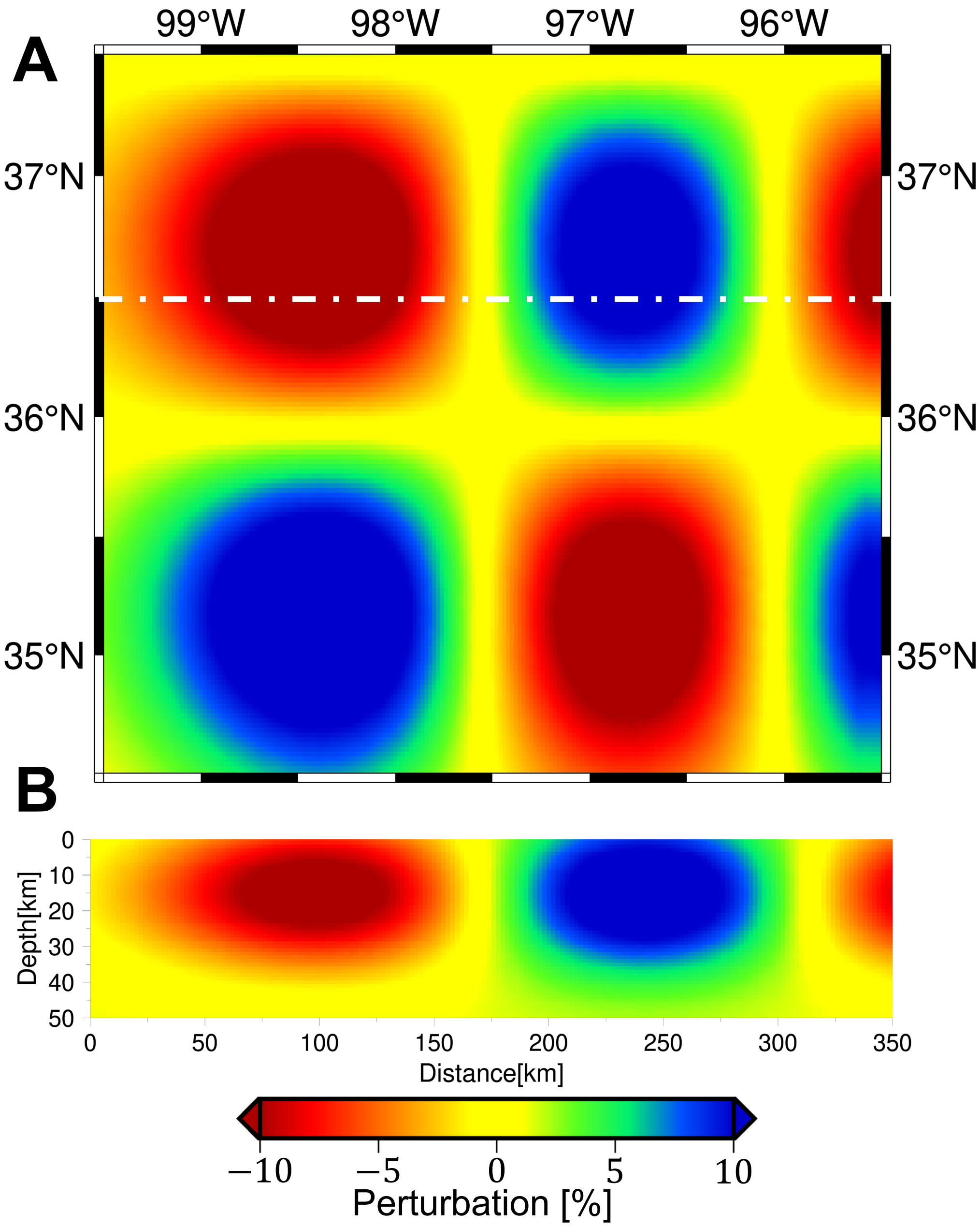

Figure S3. A designed Checkerboard model. Several positive and negative Gaussian-shape anomalies are distributed laterally in Panel A. A vertical section is cut along the white dashed line in panel A and shown in Panel B. The standard deviations of these Gaussian anomalies are $\sigma_{\mathrm{h}} = 30km$ in the horizontal direction, and $\sigma_{\mathrm{v}} = 10km$ in the vertical direction.

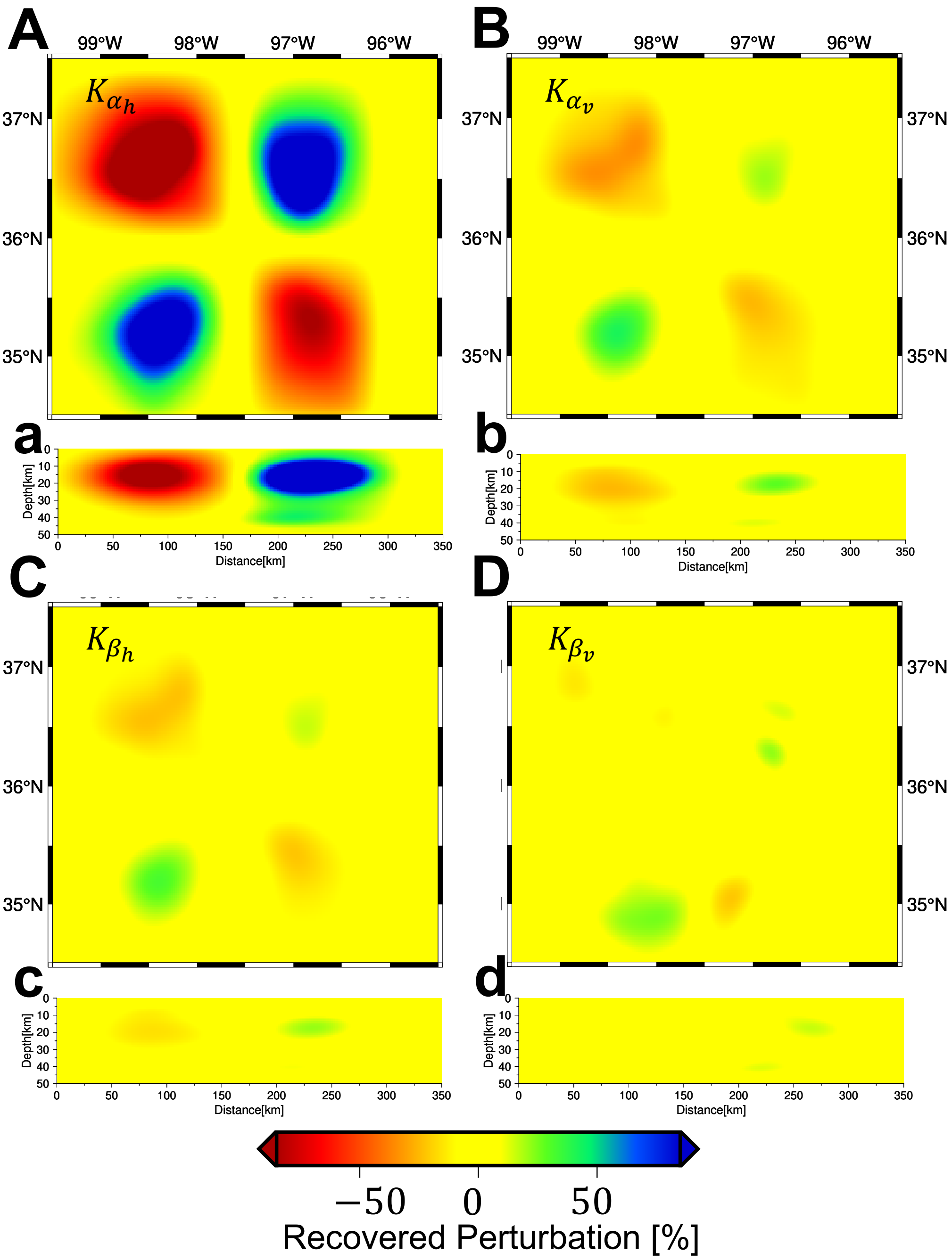

Figure S4. Recovered model gradients with respect to the model perturbation on α_h. Panel A, B, C and D are the horizontal cross section of K_{α_h}, K_{α_v}, K_{β_h} and K_{β_v}, respectively. Panel a, b, c, and d are the vertical sections of panels A, B, C and D. To make it comparable, K_{α_h}, K_{α_v}, K_{β_h}, and K_{β_v} are normalized by the maximum magnitude of K_{α_h}

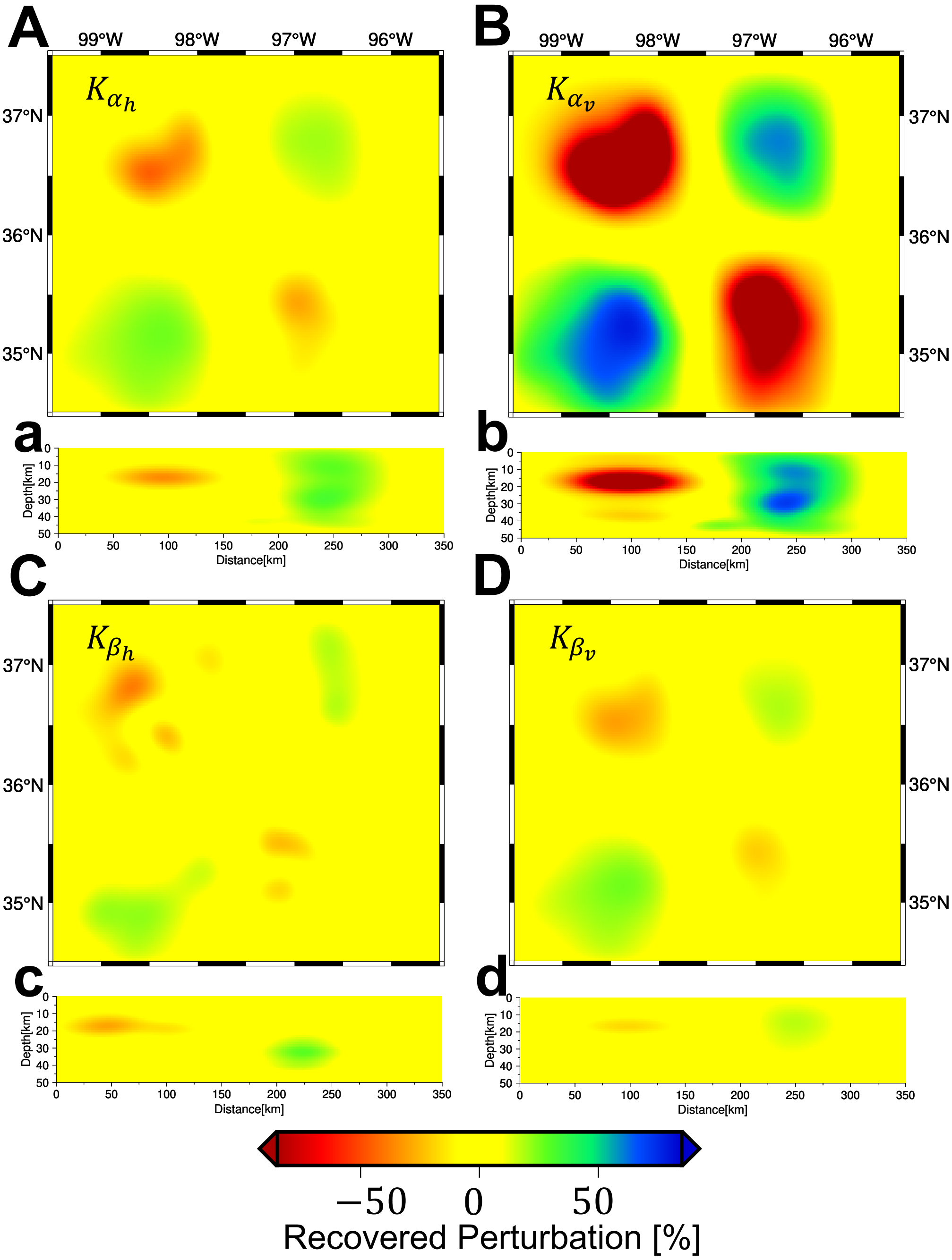

Figure S5. The same settings as Figure S4 but for K_{α_v}

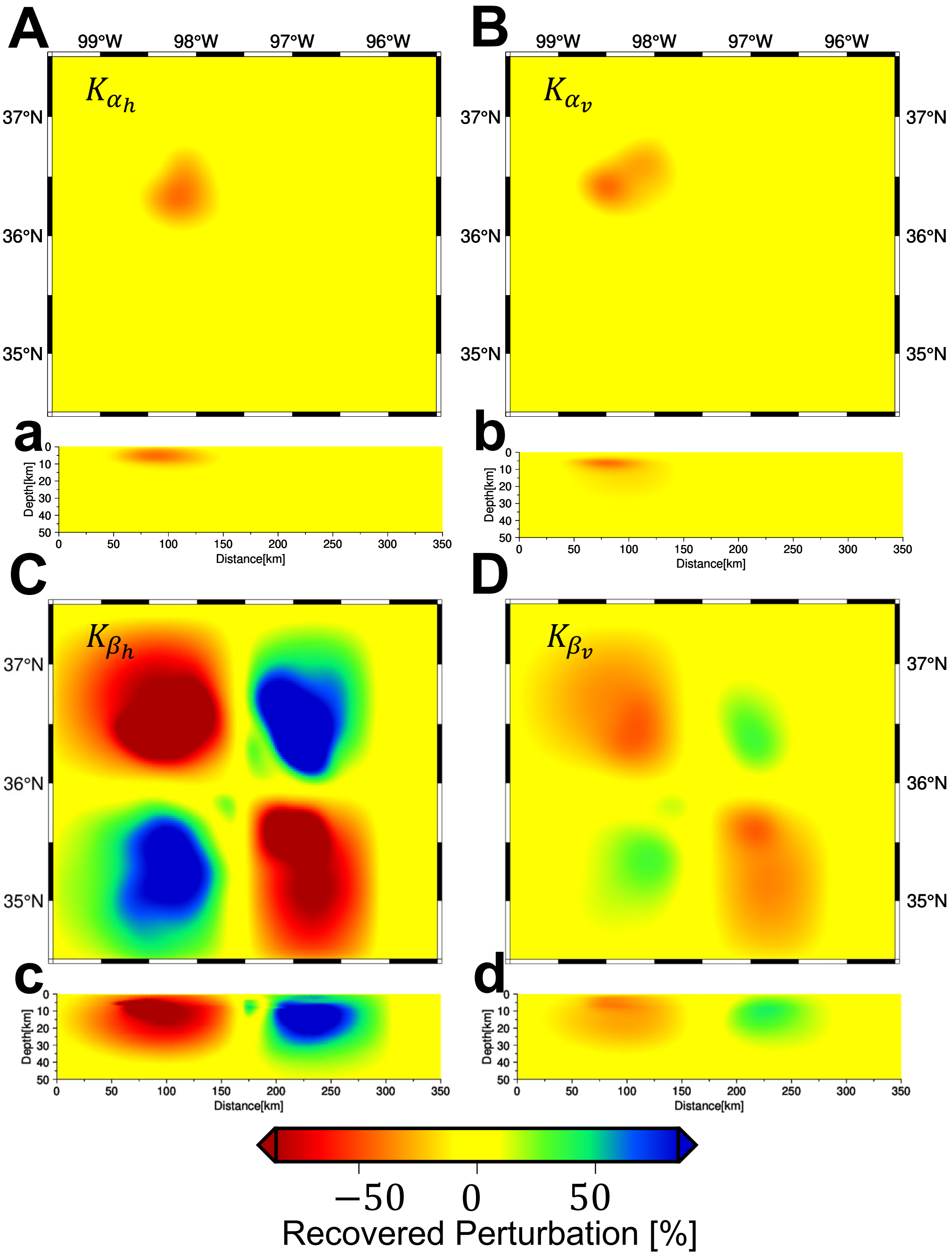

Figure S6. The same settings as Figure S4 but for K_{β_h}